UNIVERSIDADE ESTADUAL DE CAMPINAS

Instituto de Física Gleb Wataghin

GUILLERMO GERARDO RIVERA GAMBINI

Um candidato à matéria escura no contexto da física além do modelo padrão

A dark matter candidate in the context of physics beyond the standard model

CAMPINAS

2022

GUILLERMO GERARDO RIVERA GAMBINI

Um candidato à matéria escura no contexto da física além do modelo padrão

A dark matter candidate in the context of physics beyond the standard model

Tese apresentada ao Instituto de Física Gleb Wataghin da Univerisdade Estadual de Campinas como parte dos requisitos exigidos para a obtenção do título de Doutor em Ciências, na área de Física no âmbito de Acordo de Cotutela firmado entre a Unicamp e a McGill University.

Thesis presented to the Gleb Wataghin Institute of Physics of the University of Campinas in partial fulfillment of the requirements for the degree of Doctor of Sciences, in the area of Physics under the Cotutelle/Joint Ph.D Agreement signed between Unicamp and McGill University.

Supervisor/Orientador: Pedro Cunha de Holanda

ESTE TRABALHO CORRESPONDE À VERSÃO FINAL DA TESE DEFENDIDA PELO ALUNO GUILLERMO GERARDO RIVERA GAMBINI, E ORIENTADA PELO PROF. DR. PEDRO CUNHA DE HOLANDA.

CAMPINAS

2022

Ficha catalográfica
Universidade Estadual de Campinas
Biblioteca do Instituto de Física Gleb Wataghin
Lucimeire de Oliveira Silva da Rocha - CRB 8/9174

R524d

Rivera Gambini, Guillermo Gerardo, 1984-
A dark matter candidate in the context of physics beyond the standard model / Guillermo Gerardo Rivera Gambini. – Campinas, SP : [s.n.], 2022.

Orientadores: Pedro Cunha de Holanda e James Michael Cline.
Tese (doutorado) – Universidade Estadual de Campinas, Instituto de Física Gleb Wataghin.
Em cotutela com: McGill University.

1. Matéria escura (Astronomia). 2. Lépton neutro pesado. I. Holanda, Pedro Cunha de, 1973-. II. Cline, James Michael. III. Universidade Estadual de Campinas. Instituto de Física Gleb Wataghin. V. Título.

Informações Complementares

Título em outro idioma: Um candidato à matéria escura no contexto da física além do modelo padrão
Palavras-chave em inglês:
Dark matter (Astronomy)
Heavy neutral lepton
Área de concentração: Física
Titulação: Doutor em Ciências
Banca examinadora:
Pedro Cunha de Holanda [Orientador]
Flávia Sobreira
Ernesto Kemp
Cássio Bruno Magalhães Pigozzo
Gustado do Amaral Valdiviesso
James Michael Cline
Data de defesa: 07-11-2022
Programa de Pós-Graduação: Física

Identificação e informações acadêmicas do(a) aluno(a)
- ORCID do autor: https://orcid.org/0000-0002-9381-7049
- Currículo Lattes do autor: http://lattes.cnpq.br/9082825225407765

MEMBROS DA COMISSÃO EXAMINADORA DA TESE DE DOUTORADO DO ALUNO GUILLERMO GERARDO RIVERA GAMBINI - RA 153914 APRESENTADA E APROVADA AO INSTITUTO DE FÍSICA “GLEB WATAGHIN”, DA UNIVERSIDADE ESTADUAL DE CAMPINAS, EM 07/11/2022.

COMISSÃO JULGADORA:

- Prof. Dr. Pedro Cunha de Holanda – Presidente e orientadora (IFGW/UNICAMP)

- Profa. Dra. Flávia Sobreira (IFGW/UNICAMP)

- Prof. Dr. Ernesto Kemp (IFGW/UNICAMP)

- Dr. Cássio Bruno Magalhães Pigozzo (Universidade Federal da Bahia)

- Dr. Gustavo do Amaral Valdiviesso (Universidade Federal de Alfenas)

- Dr. James Michael Cline (McGill University)

OBS.: Ata da defesa com as respectivas assinaturas dos membros encontra-se no SIGA/Sistema de Fluxo de Dissertação/Tese e na Secretaria do Programa da Unidade.

CAMPINAS

2022

para mi familia por creer en mí

Acknowledgements

First of all, I would like to thank my family for their endless patience and support.

I am deeply grateful to both of my supervisors: Prof. Pedro C. de Holanda at Universidade Estadual de Campinas and Prof. James M. Cline at McGill University. Thank you for your trust in me, for your guiding of my research, and for sharing good times in non-academic activities like marches for science, recitals, having lunch, etc.

I want to thank Profs. Giorgio Torrieri, Saulo Carneiro, Bruce Sánchez-Vega, Flávia Sobreira, Orlando Peres, Ernesto Kemp, Orlado Pereyra Ravinez, and Rosendo Ochoa for their continuous academic support and friendship.

(Old) friends and colleagues who had direct impact in my life during the Ph.D.: Dennis Zavaleta, Armando Pezo, Paulo H. de Moura, Fernanda F. Rodrigues, Kayman J. Gonçalves, Andres Navarro, Garv Chauhan, Carlos Alvarez Salazar, Ana Romero Castellanos, Bárbara Peluzo, Mariano Chaves, Yago P. Porto-Silva, Gabriela Vitti Stenico, Pedro Pasquini, Jean-Samuel Roux, Benoit Laurent, Matteo Puel, Gonzalo Alonso-Álvarez, Karishma Moorthy, Qiu Shi Wang, Katarina Bleau, Cedrick Perron, Oscar Chacaltana, Frank Coronado, Ingrid Ribeiro, Leonardo Leite, Erick Lamilla, Marvyn Inga, Fiorella Aquino, Caroline Mouls, Lisbeth Corbacho, Jamille Feitosa, Luis Alejo, Jullyane G. de Jesus, and Hernan Chalco, thank you for the good things I have learned from you.

This study was financed in part by the Coordenação de Aperfeiçoamento de Pessoal de Nível Superior - Brasil (CAPES) - Finance Code 001 - 1583268, Ministry of Science, Technology and Innovation" and the "National Council for Scientific and Technological Development – CNPq 141699/2016-7, Fundo de Apoio ao Ensino, à Pesquisa e à Extensão (FAEPEX) 2039/20, the Canadian government: Emerging Leaders in the Americas Program (ELAP) scholarship, McGill Space Institute (MSI): Trottier MSI Grad Awards 2020 and 2021, McGill Graduate and Postdoctoral Studies (MGAPS): travel awards 2021 and 2022, and Canada's Natural Sciences and Engineering Research Council (NSERC).

I would like to thank Profs. Gustavo Valdiviesso, Cássio Pigozzo, Ernesto Kemp, and Flávia Sobreira for their comments and questions which helped me improve this thesis.

Special thanks to the CPG team at IFGW, you guys do a great job.

"The effort to understand the universe is one of the very few things which lifts human life a little above the level of farce and gives it some of the grace of tragedy."

Steven Weinberg

The first three minutes (1976)

Resumo

A motivação para estender o modelo padrão da física de partículas vem de muitas fontes. As massas de neutrinos e a natureza da matéria escura estão entre essas fontes e são discutivelmente os ingredientes desconhecidos mais importantes do universo que exigem explicação. Neste trabalho, estudamos como os limites publicados sobre o ângulo de mistura entre léptons neutros pesados e neutrinos ativos podem mudar quando o primeiro acopla a um singleto escalar leve. O método apresentado aqui pode ser usado para reformular restrições de outros experimentos (antigos) sem recorrer a simulações de Monte Carlo computacionalmente caras. Também propusemos um novo mecanismo para resolver o problema da cúspide central através da reativação tardia das aniquilações da matéria escura. Isso foi feito no contexto da matéria escura assimétrica. Finalmente, estudamos matéria escura multicomponente em um modelo onde $B - L$ é uma simetria gauge. Mostramos que mesmo que a densidade relativa atual do componente instável seja desprezível, o efeito da radiação escura produzida por seus decaimentos pode restringir severamente o espaço de parâmetros dos VEVs do modelo, o que está em conflito com os benchmarks anteriores na literatura.

Abstract

Motivation for extending the standard model of particle physics comes from many sources. Neutrino masses and the nature of the dark matter are among these sources and they are arguably the most important unknown ingredients of the universe which call for explanation. In this work, we have studied how the published limits on the mixing angle between heavy neutral leptons and active neutrinos can change when the former couples to a light scalar singlet. The method presented here could be used to recast constraints from other (older) experiments without resorting to computationally expensive Monte Carlo simulations. We have also proposed a new mechanism to solve the core-cusp problem through the late-time reactivation of dark matter annihilations. This has been done in the context of asymmetric dark matter. Finally, we study multi-component DM in a gauged $B - L$ model. We show that even if the present-day relative density of the unstable component is negligible, the effect of the dark radiation produced by its decays can severely constrain the parameter space of the VEVs of the model, which is in conflict with previous benchmarks in the literature.

Résumé

La motivation pour étendre le modèle standard de la physique des particules provient de nombreuses sources. Les masses de neutrinos et la nature de la matière noire font partie de ces sources et sont sans doute les ingrédients inconnus les plus importants de l'univers qui appellent une explication. Dans ce travail, nous avons étudié comment les limites publiées sur l'angle de mélange entre les leptons neutres lourds et les neutrinos actifs peuvent changer lorsque les premiers se couplent à un singulet scalaire léger. La méthode présentée ici pourrait être utilisée pour refondre les contraintes d'autres expériences (plus anciennes) sans recourir à des simulations de Monte Carlo coûteuses en calcul. Nous avons également proposé un nouveau mécanisme pour résoudre le problème noyau-pointe par la réactivation tardive des annihilations de matière noire. Cela a été fait dans le contexte de la matière noire asymétrique. Enfin, nous étudions le DM multi-composants dans un modèle $B - L$ calibré. Nous montrons que même si la densité relative actuelle de la composante instable est négligeable, l'effet du rayonnement d'obscurité produit par ses désintégrations peut contraindre sévèrement l'espace des paramètres des VEV du modèle, ce qui est en conflit avec les repères précédents dans le Littérature.

Contents

1 Introduction

The history of the dark matter (DM) research program began in 1933 when Fritz Zwicky showed there was *missing* matter in the Coma cluster of galaxies [1]. This undetected matter is used to explain cosmological observations like flat rotation curves in spiral galaxies [2], gravitational lensing from clusters of galaxies, and the bullet cluster [3], among others[1]. Let us briefly see how cold dark matter appears in different cosmological scenarios and why it is thought to be of non-baryonic origin.

1 **Galaxy halos**: The shape of the Universe has always been of great interest for humankind. It is possible to know if it is open, close, or flat by determining the ratio of its mass density ρ to the critical density $\Omega = \rho/\rho_c$. As finding ρ is a very difficult task, a first approach would be to determine the average mass density $\langle\rho\rangle$ by multiplying the number density of galaxies $n_{\rm GAL}$ times the average mass per galaxy $\langle M_{\rm GAL}\rangle$. Invoking Kepler's 3rd law,

$$GM(r) = v^2 r, \tag{1.1}$$

where $M(r)$ is the mass interior to r, $v(r)$ is the orbital velocity at distance r from the center of the galaxy, and G is Newton's constant. Assuming all luminous matter is concentrated in a region of radius $r_{\rm GAL}$, the mass of this matter $M_{\rm LUM} = v^2(r_{\rm GAL})r_{\rm GAL}/G$ gives $\Omega_{\rm LUM} \approx 0.01$ [8]. This means that this kind of matter only accounts for about 1% of the mass in the Universe. Where is the rest? Maybe there is something there that our detectors are not 'seeing'. When $r > r_{\rm GAL}$, Eq.(1.1) gives $GM_{\rm GAL} = v^2 r$, so we have

$$v \propto r^{-1/2}. \tag{1.2}$$

Observations of spiral galaxy NGC 3198 give a flat rotation curve, *i.e.* the circular velocity is approximately constant for $r > r_{\rm GAL}$, which obviously disagrees with Eq.(1.2) (see Fig.1a). Models that try to solve this discrepancy usually take into consideration two distinct distributions of matter: an exponential disk of luminous

[1] Modified gravity theories are alternatives to the dark matter hypothesis, but they will not be discussed in this work.

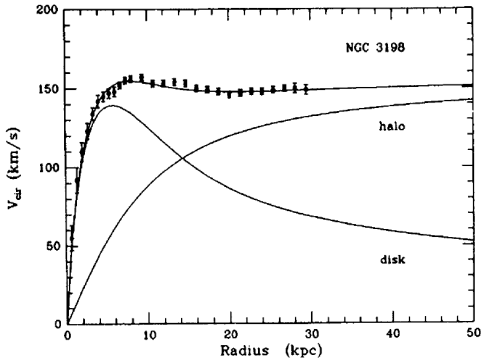

(a) Rotation curve of spiral galaxy NGC 3198 [4].

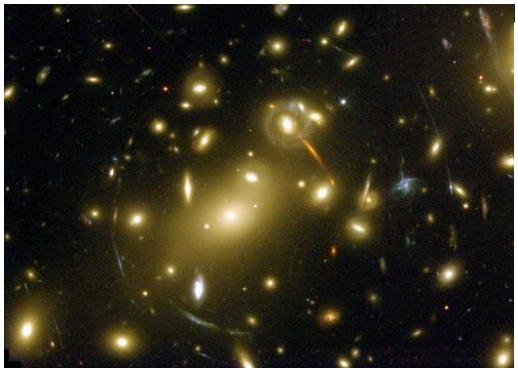

(b) Galaxy cluster Abell 2218 [5].

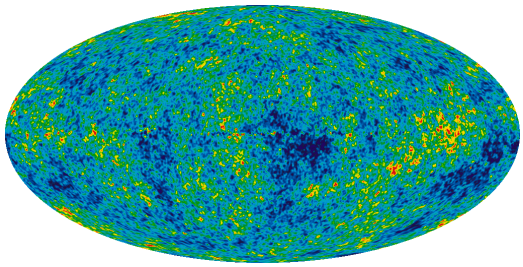

(c) The cosmic microwave background [6].

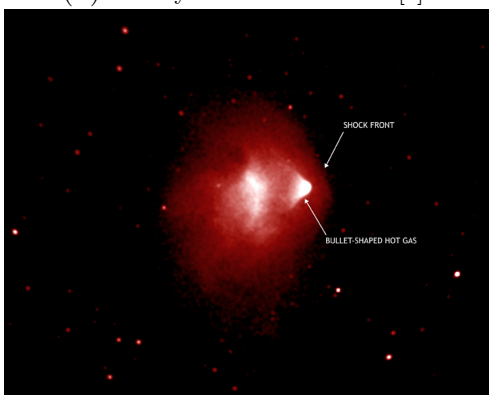

(d) Galaxy cluster 1E 0657-56 (*a.k.a.* the bullet cluster) [3].

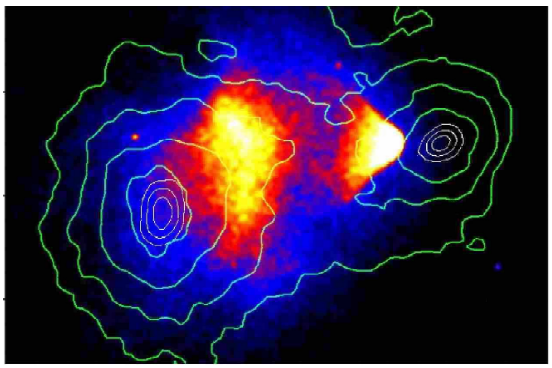

(e) Map of the gravitational potential in a collision of two clusters of galaxies [3].

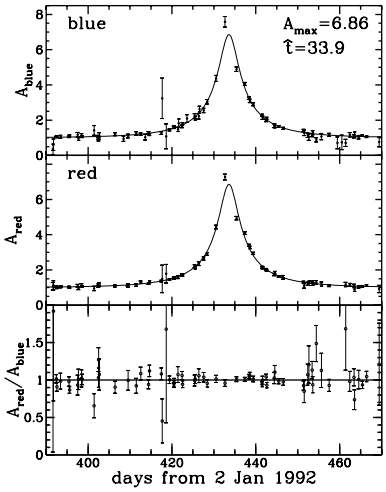

(f) Color light curve for a star in the Magellanic cloud [7].

Figure 1 – **Evidence of dark matter in our universe**. (a) Spiral galaxy NGC 3198 can not be successfully modeled by a disk of baryonic matter only. A halo of some unseen matter must be added to match the rotation curve. (b) Light coming from luminous objects that are positioned behind galaxy cluster Abell 2218 gets deflected by it, creating faint arcs. (c) The detailed picture of the early universe reveals 13.77 billion year old temperature fluctuations, which were the seeds that created the galaxies. (d) In the collision of two clusters of galaxies, the hot ionized gas of the smallest one gets shaped like a bullet, hence producing a bow-shaped shock front. (e) The collision of two large clusters could not exhibit this form of the gravitational potential, if it wasn't for dark matter. (f) Flux divided by median observed flux, microlensing model fitting in both blue and red passbands. The brightness of the star presents a *temporary* (33.9 days) increase around $t = 433.55 \pm 0.04$ days after january 2nd 1992.

matter and a halo of dark matter [4]. As a result, two-component models usually get good fits (see Fig.1a).

2 **Clusters of galaxies**: In his 1933 paper 'The redshift of extragalactic nebulae', Fritz Zwicky studied the Coma cluster of galaxies and showed, by means of the virial theorem, that the density of the dark matter is much greater than that of the luminous matter. Assuming the Coma cluster to be a mechanically stationary system, the virial theorem tells us that the mean kinetic $\langle \mathcal{E}_k \rangle$ and potential $\langle \mathcal{E}_p \rangle$ energies are related by

$$\langle \mathcal{E}_k \rangle = -\frac{1}{2} \langle \mathcal{E}_p \rangle . \tag{1.3}$$

For purposes of estimation, let us assume a uniform distribution of mass (ρ= constant) in the cluster. In this way, if M and R for stand for its mass and radius, respectively, then its gravitational energy U is

$$U = -\int_0^M \frac{GM(r)}{r} dm = -\frac{3}{5}\frac{GM^2}{R}. \tag{1.4}$$

From this result and Eq.(1.3), we get

$$\frac{1}{2}\left\langle v^2 \right\rangle = \langle \mathcal{E}_k \rangle = -\frac{1}{2} \langle \mathcal{E}_p \rangle = -\frac{1}{2}\left(\frac{U}{M}\right) = \frac{3}{10}\frac{GM}{R}, \tag{1.5}$$

$$\left\langle v^2 \right\rangle^{1/2} \approx 80 km/s. \tag{1.6}$$

Unfortunately, the velocity dispersion in the Coma cluster goes from 1500 to 2000 km/s. This problem made Zwicky think that, as $\langle v^2 \rangle^{1/2} \propto \sqrt{M}$ from Eq.(1.5), the cluster needed its mass to be at least *400 times greater* than the mass of its luminous matter[2].

3 **Gravitational lensing**: Clusters of galaxies can be used as telescopes because gravity can 'bend' light. They will deflect light coming from, say, a single galaxy or a group of them (see Fig.1b), and the measurement of the deflection will give us the mass of the cluster. Lensing results seem to match the mass-to-light ratio $M/L \simeq 300h$ obtained from the study of the Coma cluster, therefore reinforcing the statement of missing mass in this group of galaxies.

[2] Zwicky's estimate of $M_{\rm GAL}$ was significantly smaller than its current value, but he noted a troubling discrepancy in the mass-to-light ratio of the Coma cluster, i.e. $M/L \simeq 300h$ (see item 4).

4 **Mass-to-light ratios**: If we consider the mass of the universe to be mainly the addition of the masses of its visible parts, *i.e.* the galaxies, then finding the mass-to-light ratio of a single galaxy and, assuming this is the same for the whole universe, multiplying it by the luminosity of the universe should give us its mass and, consequently, Ω.

The luminosity of astronomical objects in the Universe reveal a total luminosity density of $\rho_L = 2 \pm 0.7 \times 10^8 h L_\odot Mpc^{-3}$ [9]. As the critical density is given by $\rho_c = 3H_0^2/8\pi G = 2.77537(13) \times 10^{11} \Omega h^2 M_\odot Mpc^{-3}$ [10], the critical mass-to-light ratio reads [11]

$$\left(\frac{M}{L}\right)_c = 1390h \pm 35\%. \tag{1.7}$$

As we have seen before, $M/L \simeq 300h$. Since this value is far from the result obtained in Eq.(1.7), more low luminosity massive objects are needed in order to get our observed flat universe, *i.e.* $\Omega = 1$.

5 **The cosmic microwave background (CMB)**: Planck[3] measurements of the CMB temperature and lensing-potential power spectra at high multipoles were used to find the physical densities of baryons ($\Omega_b h^2 = 0.02205 \pm 0.00028$) and cold dark matter ($\Omega_{DM} h^2 = 0.1199 \pm 0.0027$) in the ΛCDM cosmology [12] . From this results, it can be seen that not only matter is not the most dominant contributor to the energy density of the universe, but also most of it is of unknown composition.

6 **The large-scale structure of the Universe**: As the baryonic density parameter Ω_b is very small compared to the other 'ingredients' of the Universe, it would have required large fluctuations in the primordial baryon density in order to form the observed number of galaxies in our universe. These large fluctuations would also mean large anisotropies in the cosmic microwave background today. Consequently, galaxy formation in a purely baryonic medium is totally ruled-out by the observation of small anisotropies in the CMB (Fig.1c).

7 **The bullet cluster**: The most recent works on observational cosmology highlight the presence of DM in collisions of galaxy clusters. In Fig.1d we see the collision of two galaxies merging into a double cluster (galaxy cluster 1E 0657-56), which is

[3] *Planck* is the European Space Agency's mission to map the sky measuring temperature and polarization anisotropies of the cosmic microwave radiation.

known as the *bullet cluster* after the bullet-shaped hot gas resembling a supersonic bullet producing shock waves. The main ingredients in these collisions are galaxies, clouds of hot gas, and dark matter. As galaxies are very distant from each other, they don't participate much in the collisions. However, hot gases do collide, producing a shock front (Fig.1d) and, most importantly, separating themselves from the DM. How can we know this? As can be seen in Fig.1e, the map of the gravitational potential clearly indicates the presence of two *unseen* massive objects that dominate in terms of the mass in this system.

"*Most of what we have learned (about dark matter) since 1986 is what the dark matter is not; discovering what the dark matter really is remains an exciting challenge*"

John N. Bahcall[4]

Microlensing: This astronomical phenomenon is based on the gravitational lens effect and uses the relative motion between the source and the lens to temporary *brighten* the combined signal. This means it is possible to find objects that emit little or no light by monitoring the light curves coming from the source, which are being deflected and distorted by such objects. After monitoring tens of millions of stars, which increase their brightness by means of this phenomenon, it is believed that most of the unseen matter is *not* of baryonic origin. As a result, MACHOs[5] in the mass range $10^{-7} < M/M_{\odot} < 15$ cannot account for the galactic dark matter [14]. For this reason, it is necessary to go beyond of the standard model of particle physics where dark matter can be studied as, for example, a WIMP [15].

[4] In 1986, John Bahcall and Steven Weinberg organized the 4^{th} Jerusalem Winter School. The articles that grew up out of those lectures were published here [13].

[5] Massive compact halo objects.

2 Recasting constraints for heavy neutral leptons

Right-handed neutrinos N with masses in the range $0.1 - 1000\,\text{GeV}$ are commonly known as heavy neutral leptons (HNLs). Since they are SM-gauge-singlet fermions and interact with the SM only through mixing with active neutrinos, they naturally belong to the dark sector. These mixings $|U| \sim \sqrt{m_\nu/m_N}$ have been constrained by beam-dump and other experiments. In this chapter, we show these limits cannot be directly applied to HNLs that couple to a light singlet scalar that mixes with the Higgs boson.

The content of this chapter is heavily based on Ref. [16], where our main results are published. These have been presented at the XXX International Conference on Neutrino Physics and Astrophysics (Neutrino 2022) in Seoul, Korea and The Eleventh Workshop of the LLP (Long-lived particles) Community at CERN (by invitation).

2.1 Motivation

2.1.1 (Partially) asymmetric dark matter

The dark matter puzzle, the mystery of small neutrino masses, the matter-antimatter asymmetry, and inflation call for physics beyond the standard model (BSM). A common denominator in BSM models which can address several of these missing pieces in the SM, *e.g.* νMSM [17, 18], SMASH [19], and scotogenic [20, 21], is the presence of right-handed neutrinos in their matter content.

Along these lines, a new model [22] has come up recently where the (partially)[1] asymmetric dark matter candidate is a quasi-Dirac heavy neutral lepton, its stability is related to the mass of the lightest neutrino, and its relic abundance can be explained if there's also a new SM-singlet scalar that couples to this DM particle and mixes with the Higgs boson. In this scenario, when the singlet scalar can be produced in DM decays, experimental limits that don't consider this decay channel must be reanalyzed.

[1] If asymmetric DM annihilations are not strong enough, its symmetric component may not be totally depleted, hence after freezeout the total DM would still have both symmetric and asymmetric components. In the next chapter, we delve deeper into asymmetric DM models.

2.1.2 Heavy neutral leptons (HNL)

Neutrinos are massive. However, there is not a consensus on the mechanism responsible for the generation of these masses. One of the most popular proposals for generating these masses is the seesaw mechanism. In its simplest form, new SM singlet fermions N mix with the active neutrinos ν_α ($\alpha = e, \mu, \tau$)

$$-\mathcal{L}_\nu^{\text{mass}} = \mu \bar{N} \nu + \frac{M}{2} \bar{N}^c N + \text{H.c.}, \tag{2.1}$$

producing light ν_i and heavy neutral fermions N'_j, where μ and M are the Dirac and Majorana masses, respectively. For instance, for one SM singlet fermion N that mixes exclusively with electron neutrinos ν_e,

$$\nu_1 \simeq \nu_e - \left(\frac{\mu}{M}\right) N \quad \text{and} \quad N' \simeq N + \left(\frac{\mu}{M}\right) \nu_e, \tag{2.2}$$

with masses

$$m_1 \simeq \frac{\mu^2}{M} \quad \text{and} \quad M_{N'} \simeq M, \tag{2.3}$$

in the limit where $\mu \ll M$.

As we can see from Eq.(2.2), the new physics appears in the ratio of the Dirac to the Majorana masses, so it is convenient to define

$$|U_e| \equiv \mu / M, \tag{2.4}$$

as this quantity will appear in the production and decay of the HNLs, which can be produced in neutrino experiments. For this reason, many experiments looking for these HNLs have put bounds on this mixing parameter in the case of 'pure mixing', *i.e* when there is only one HNL and it mixes with one active neutrino only. We will discuss three of these experiments in the next section.

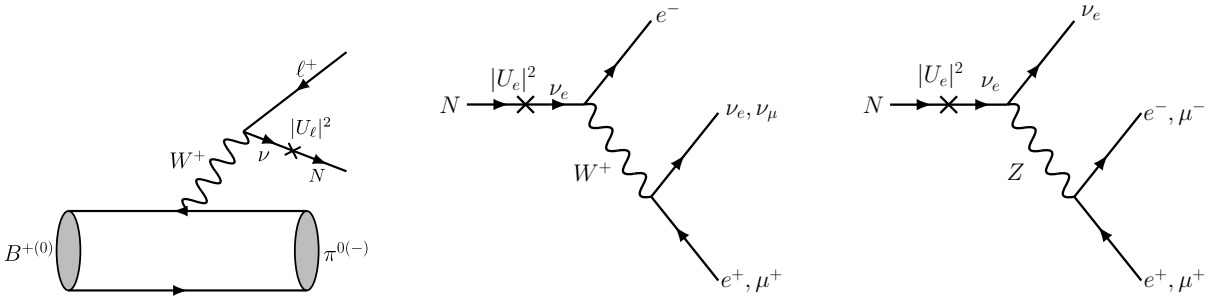

Figure 2 – Left: HNL production from B meson decays. Center: HNL charged decays. Right: HNL neutral decays.

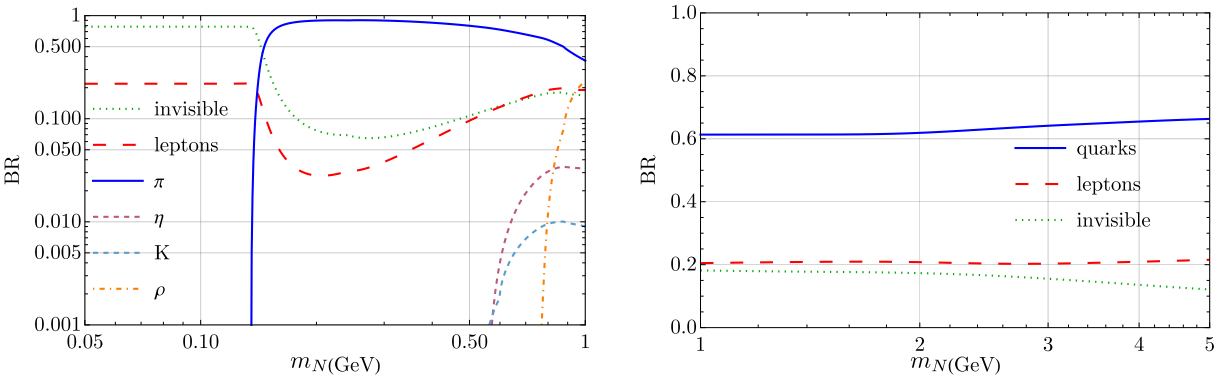

Figure 3 – HNL weak decays. Image reproduced from [23].

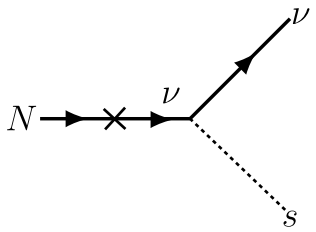

Figure 4 – HNL two-body decay $N \to \nu\, s$.

2.1.3 SM gauge singlet scalar: a new decay channel for HNLs

A singlet scalar s that interacts with heavy neutral leptons N through

$$g_s\, s\bar{N}N \;\in\; -\mathcal{L}, \tag{2.5}$$

can induce two-body decays (as shown in Fig.4) with decay rate

$$\Gamma(N \to s\nu_\alpha) = \frac{g_s}{32\pi} m_N \left(1 - \frac{m_s^2}{m_N^2}\right)^2 |U_\alpha|^2. \tag{2.6}$$

These new decays will compete with the usual weak decays. As an example, in Fig.5 we show the production and decay of HNLs from electron-positron collisions. The new decay channel $N \to \nu\, s$ is shown at the bottom.

2.2 Experiments

2.2.1 DELPHI

The DELPHI detector at the Large Electron-Positron (LEP) collider collected 3.3×10^6 hadronic Z decays from 1991 to 1994 [24]. In these decays, HNLs could be produced in Z boson decays: $Z \to N\bar{\nu}$, $Z \to \bar{N}\nu$, and $Z \to \bar{N}N$[2], through the mixing with light

[2] $Z \to \bar{N}N$ is suppressed by $|U|^4$.

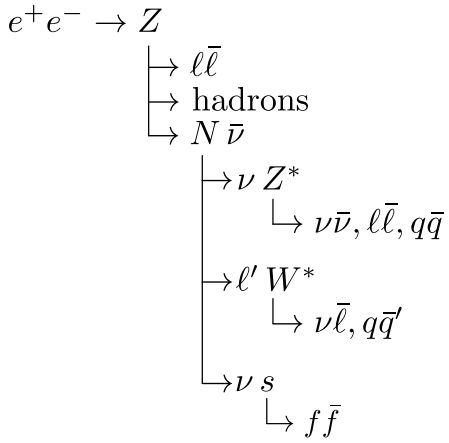

Figure 5 – Z boson decays including the new $N \to \nu\, s$ channel.

neutrinos. The branching ratio for these decays is given by

$$\mathrm{BR}(Z \to N\bar{\nu}_\alpha) = \mathrm{BR}(Z \to \nu_\alpha\bar{\nu}_\alpha)|U_\alpha|^2 \left(1 - \frac{m_N^2}{M_Z^2}\right)^2 \left(1 + \frac{1}{2}\frac{m_N^2}{M_Z^2}\right), \tag{2.7}$$

where $\mathrm{BR}(Z \to \nu_\alpha\bar{\nu}_\alpha) \approx 0.063$ for $\alpha = e, \mu, \tau$[3](no summation over repeated indices). The mean decay length of the HNLs is approximately

$$L \cong \frac{3}{|U_\alpha|^2} \left(\frac{\mathrm{GeV}}{m_N}\right)^6 \text{ cm}. \tag{2.8}$$

In their study, the DELPHI Collaboration analyzed three different decay topologies: $\nu\ell\bar{\ell}$, $\nu q\bar{q}$, and $\ell q\bar{q}'$ where $\ell = e, \mu, \tau$, $q = u, d, s, c, b$, and $q\bar{q}' = u\bar{d}, c\bar{s}$ plus charge conjugate states, which we illustrate in Fig. 5.

The fraction of Z bosons leading to observed HNLs decaying inside the detector via weak interactions is

$$f_w = 2 \times \mathrm{BR}(Z \to N\bar{\nu}_\alpha)\left(1 - e^{-D_L/L}\right)\varepsilon(m_N). \tag{2.9}$$

The factor of 2 accounts for the charge conjugate decay channel $Z \to \bar{N}\nu_\alpha$ and the reconstruction efficiency ε is a function on the mass of the HNL m_N that we take from Fig. 4 of Ref. [24]. D_L is the length of the region where decays are observed. As described below, we infer this parameter (obtaining $D_L = 200\,\mathrm{cm}$) when we reproduce the published limits for weak HNL decays.

2.2.2 Belle

The Belle experiment (1999-2010) searched for direct HNL decays ($N \to \ell^\pm\pi^\mp$, $\ell = e, \mu$) at the KEKB e^+e^- collider, where $B\bar{B}$ pairs were created at the $\Upsilon(4S)$ resonance

[3] LEP limits apply equally to all flavors of HNLs [25].

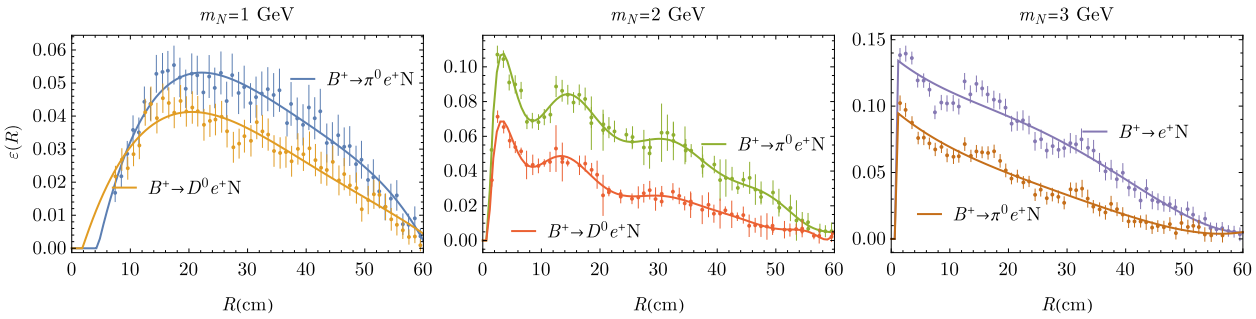

Figure 6 – Belle efficiencies $\varepsilon(R)$ for different HNL production modes. Solid curves: our fits for these efficiencies. In order to interpolate between different values of masses, we use the mass-dependent efficiency curves shown in Fig. 2 of Ref. [26].

in these collisions. The usual formula to calculate the number of detected heavy neutral leptons (N_N) is [26]

$$N_N = 2N_{B\bar{B}}\,\mathrm{BR}(B\to N)\,\mathrm{BR}(N\to\ell\pi)\int \frac{m_N\Gamma_N}{p_N}\exp\left(-\frac{m_N\Gamma_N}{p_N}\,R\right)\varepsilon(R)\,dR, \quad (2.10)$$

where $p_N = |\vec{p}_N|$ is the momentum of the HNL, Γ_N is its total decay width, and $\varepsilon(R)$ is its reconstruction efficiency, which depends on the distance R from the interaction point, the mass of the HNL, and its production mode. In Fig. 6, $\varepsilon(R)$ is shown for three values of m_N and the most relevant decay channels of the B^+ meson[4].

At Belle, the most favorable mass range in which to look for HNLs is $M_K < m_N < M_B$. For this reason, the total branching ratio for HNL production includes $X = \pi, \eta, \rho, \omega, \eta', \phi, D, D^*$ for semileptonic decays

$$\mathrm{BR}(B\to N) = \sum_X \mathrm{BR}(B\to X\ell_1 N), \quad (2.11)$$

and

$$\mathrm{BR}(B\to N) = \mathrm{BR}(B\to \ell_1 N), \quad (2.12)$$

for purely leptonic decays [26]. For Majorana HNLs,

$$\mathrm{BR}(N\to\ell_2\pi) = \mathrm{BR}(N\to\ell_2^-\pi^+) + \mathrm{BR}(N\to\ell_2^+\pi^-), \quad (2.13)$$

where $\mathrm{BR}(N\to\ell_2^+\pi^-) = \mathrm{BR}(N\to\ell_2^-\pi^+)$. Therefore the signal events of the form $\ell_1\ell_2\pi$ are $e^+e^+\pi^-$, $e^+e^-\pi^+$, $e^-e^+\pi^-$, and $e^-e^-\pi^+$. In case of Dirac HNLs, we should only consider processes where the signal fermion ℓ_2, which is produced by the HNL, has the opposite electric charge with respect to the production fermion ℓ_1 that is coming from the

[4] We thank Dmitri Liventsev for providing these data.

decay of the B meson. For the calculations of the HNL production and decay products we followed Ref. [23][5], which is updated relative to the values used in the Belle analysis and leads to some small differences in our determination of the standard limits for $|U|^2$ compared to the published version.

2.2.3 CHARM

The CHARM Collaboration searched for HNLs in the mass range $0.5 - 1.8$ GeV produced in the decays of $D^{\pm}$ and D^0 [29]. In subsequent analyses [30, 31], this range was expanded up to ∼2 GeV by considering also the production of D_s, which we emulate in this work.

In the CHARM search, 400 GeV protons were stopped by a copper beam dump, producing D mesons. These could decay into HNLs via mixing, subsequently decaying and producing one or two separate electromagnetic showers ($N \to e^+e^-\nu_e$), two tracks ($N \to \mu^+\mu^-\nu_\mu$), or one track and one electromagnetic shower ($N \to e^+\mu^-\nu_e$ or $N \to \mu^+e^-\nu_\mu$). The decay region was 35 m long and it had a 3×3 m^2 cross-sectional area.

The expected number of events is given by

$$N = N_D \,\mathrm{BR}(D \to N)\,\mathrm{BR}(N \to \ell'\ell\nu_\ell)\,\mathcal{A}\,e^{-d/L_N}\left(1 - e^{-D_L/L_N}\right)\varepsilon, \tag{2.14}$$

where N_D is the number of D mesons produced by protons in the dump, $\mathcal{A}$ is the acceptance factor (the fraction of HNLs that enter the decay region), $d = 480$ m is the distance from the interaction point (IP) to the beginning of the decay region, D_L =35 m is the length of the decay region, L_N is the mean decay length of the HNLs, and $\ell, \ell' = e, \mu$. This formula is similar to Eq.(2.10) in the case where the reconstruction efficiency ε is constant and the integration limits correspond to the boundaries of the detection region.[6] A typical value for the efficiency is $\varepsilon \sim 0.6$ for HNLs of mass $m_N \sim 1$ GeV [29].

[5] We used $M_{\mathrm{pole}} = \infty$ [27, 28] instead of 5.65 GeV [23] for $f_0^{B\to\pi}$ in the calculations of the B meson form factors.

[6] In the original analysis made by the CHARM collaboration [29], the distance from the interaction point to the beginning of the detector was ignored, thus taking $d = 0$ and incorrectly leading to exclusion of arbitrarily large mixings $|U|^2$.

2.3 Methodology

2.3.1 An algorithm to reproduce existing limits on $|U|^2$

The first step we take to reproduce the observed limits of a given experiment is to compute the fractional number f of signal events, relative to decaying parent particles, on a grid in the $\log_{10}|U|^2 - \log_{10}(m_N/\text{GeV})$ plane. Next, we plot contours of f, and choose the curve that best reproduces the published limit. This fraction is generally determined by the product of three probabilities,

$$f = \frac{N_E}{N_P} = \sum_{P,X,Y} \mathcal{P}_1(P,X)\,\mathcal{P}_2(Y)\,\mathcal{P}_3(P,X)\,, \tag{2.15}$$

where N_E is the number of observed events and N_P is the number of parent particles P the decays of which could produce HNLs. N_P might be given by a collaboration or it might be computable from, for example, the number of protons on target (POT) and the production fractions [32, 33]. The three probability factors are specified as follows.

$\mathcal{P}_1 = \text{BR}(P \to NX)$ is the probability of HNL production for a given decay mode of P. The HNL is accompanied by particles X. For instance, for CHARM in the case of pure mixings with electron neutrinos, $X = e^+$, e^+K^0, e^+K^{*0}, and $e^+\pi^0$, with $P = D^+$. X could be used to trigger for event candidates (Belle) or not (DELPHI, CHARM).

$\mathcal{P}_2 = \text{BR}(N \to Y)$ is the probability for the HNL to decay into the particles that produce the signal being searched for. For DELPHI, $\mathcal{P}_2 = 1$ since all HNL decays compete with the Z bosons'. In the case of Belle, $\mathcal{P}_2 = \text{BR}(N \to e\pi)$ for HNLs that mix exclusively with ν_e (recall signal events are $ee\pi$ where the second lepton and the pion have opposite electric charge.) In contrast with DELPHI and Belle, the CHARM detector is far from the interaction point, so one must account for the fact that not all decay products of the HNLs travel towards the detector. The acceptance factor $\mathcal{A}$, which generally depends on the mass of the HNL and the geometry of the experiment, quantifies this effect [29]. In our analysis, it is taken as a free parameter to be fit by reproducing the sensitivity of the experiment.

$\mathcal{P}_3$ is the probability of reconstructing the HNL from its decays. Its general form is

$$\mathcal{P}_3 = \int_d^{d+D_L} \frac{e^{-R/L_N}}{L_N}\,\varepsilon(R,P,X)\,dR, \tag{2.16}$$

where $\varepsilon(R, P, X)$ is the reconstruction efficiency. ε depends on the mass of the HNL m_N, its production mode (P, X), and the distance R from the interaction point to where it decays. The decay length L_N of the HNL depends on its momentum and the production modes, but it is more sensitive to the type of decay, *i.e.* two-body or three-body.

In Eq. (2.16), the distance from the interaction point to the beginning of the decay region inside the detector is called d. For DELPHI where HNLs are created from the decays of Z bosons at rest, $d = 0$. For Belle, the background is higher near the interaction point, so the experiment is insensitive to small-R events. Therefore, these are rejected by selection criteria such that $\varepsilon \to 0$ at $R = 0$. As the exact behavior of ε is uncertain near $R = 0$, we take d to be an undetermined small cutoff to be fit by matching Belle constraints. For CHARM the value $d = 480\,\text{m}$ is specified in their article [29].

To calculate the mean decay length of the HNLs, $L_N = p_N/(m_N\Gamma_N)$, we calculated the momenta in the rest frame of the parent particles and boosted them to the laboratory frame. We neglected departures from the axis of the parent mesons. For three-body decays $P \to N\ell x$ the maximum value of the momentum of the HNL is

$$|\vec{p}_N^{\,(\max)}| = \frac{1}{2m_P}\left[\left(m_P^2 - (m_\ell + m_x + m_N)^2\right)\left(m_P^2 - (m_\ell + m_x - m_N)^2\right)\right]^{1/2}. \quad (2.17)$$

We used $|\vec{p}_N| = |\vec{p}_N^{\,(\max)}|/2$ before applying Lorentz transformations to the laboratory reference frame and assumed $|\vec{p}_P| \approx 67$ GeV, for $P = B^\pm, D^\pm, D^0$, and D_s as in [30].

Fig. 7 shows contours of the fraction f of signal events for DELPHI. The best-fit value is $\log_{10} f = -6.05$. This value indicates that the experiment was sensitive to one part in $\sim 10^6$ Z bosons decaying into HNLs. This is the correct order of magnitude because DELPHI produced $\sim 10^6$ Z bosons and observed one event. The expected background of events is 0.8. The shape of the exclusion curve can be further tuned by varying the length of the decay region D_L. We took $D_L = 200$ cm as it provides the optimal fit in comparison with the red curves in Fig. 7.

For Belle, one must consider the dependence on the reconstruction efficiencies $\varepsilon(R)$ (see figure 6). In this case, we have considered the integration limits to go from $d = 1.75\,\text{cm}$ to $d + D_L = 60\,\text{cm}$. The curve that best reproduces the original constraint on $|U|^2$ vs. m_N is obtained with $\log_{10} f = -10.1$, regardless of the HNL flavor. With this choice, the total number of events is $N_E = 2\,N_{BB} \times 10^{-10.1} = 0.12$, where $N_{BB} = 772 \times 10^6$ is the number of $B\bar{B}$ pairs produced at Belle, indicating the limits in Fig. 8 (center) are in

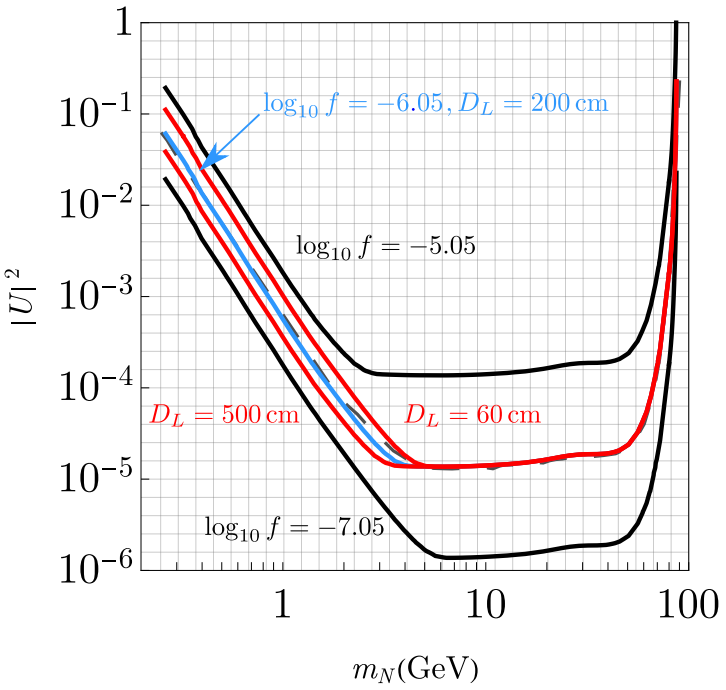

Figure 7 – Contours of detectable fraction f of Z bosons decaying into HNLs at DELPHI. Black curves illustrate the dependence on f, while red curves show the dependence on D_L, the assumed size of the decay detection length, Eq. (2.9). Blue curve is the best fit to the published limit (dashed curve).

accordance with the null results in this search for HNLs. For these calculations we used updated formulas for B meson branching ratios and HNL decay widths from Ref. [23]. We also reproduced Belle's original limits based on superseded branching ratios [34]. The main difference between the updated and original constraints is seen in the region near $m_N \gtrsim 2\,\text{GeV}$ because of revisions in the branching ratios for $B \to \rho N\ell$ and $B \to \pi N\ell$ production modes.

For CHARM, we integrate from $d = 480\,\text{m}$ to $d+D_L = 515\,\text{m}$ [30]. The excluded region in the $|U|^2 - m_N$ plane is located to the left of the blue curve in Fig. 8 (Right). In order to interpret f as the fraction of events for a null search for HNLs in the CHARM experiment, we consider the efficiencies to be 60% as reported by the CHARM collaboration for m_N =1 GeV [29], and the acceptance factor to be $\mathcal{A} \cong 10^{-3}$ (see Fig. 7 of Ref. [31]). Next, we fix $\log_{10} f = -15.6$ to match the original limit, giving the number of events $N_E = N_D \times f = 2.24 < 2.3$ at 90% C.L.. The number of $D's$ was determined using $N_{D_i} = N_{POT} \times \chi_{c\bar{c}} \times f_{c\to D_i}$, $N_{POT} = 2.4 \times 10^{18}$, $\chi_{c\bar{c}} \approx 4 \times 10^{-3}$ for a 400 GeV proton beam [35], $f_{c\to D^+} = 0.207$, $f_{c\to D^0} = 0.632$, and $f_{c\to D_s} = 0.088$. The values of the production fractions are taken from [32, 33].

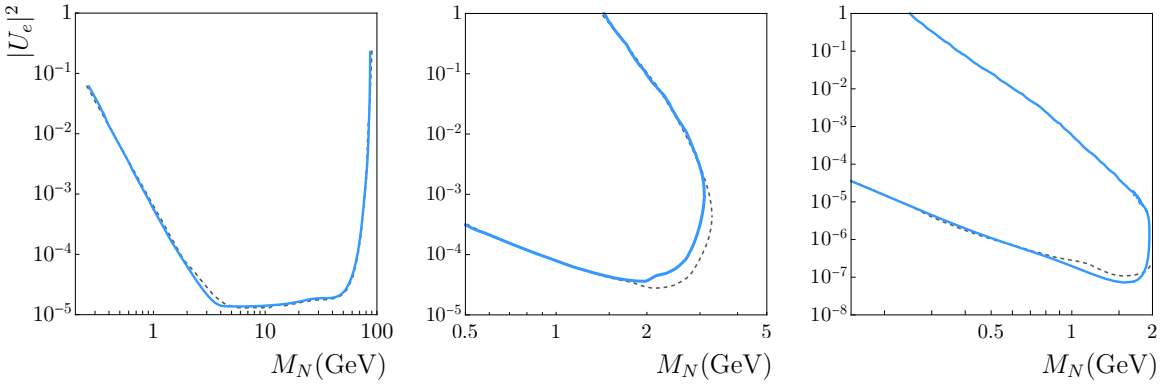

Figure 8 – **(Left)** Dashed curve: DELPHI limits at the 95% confidence level on $|U|^2$ as a function of the HNL mass [24]. These limits apply equally to all neutrino flavors. Blue curve: our result using equation 2.9. **(Center)** Dashed curve: Belle limits at 90% C.L. on $|U_e|^2$ [26]. Blue curve: our result using the procedure described above. The difference in the region $\gtrsim 2$ GeV is due to the use of updated formulas for HNL production and decay [23], and the treatment of HNL momenta (see appendix). **(Right)** Dashed curve: CHARM limits at 90% C.L. on $|U_e|^2$ [29]. Blue curve: our result for these limits. A similar result is obtained in [31].

2.3.2 Adding a SM gauge singlet scalar

Now we add a SM gauge singlet scalar s that couples to HNLs with strength g_s and also mixes with the Higgs boson through a small angle θ,

$$g_s s\bar{N}N + \frac{s_\theta\, m_f}{v} s\bar{f}f \;\in\; -\mathcal{L}, \tag{2.18}$$

where $s_\theta \equiv \sin\theta$, $v = 174\,\text{GeV}$ is the complex Higgs vacuum expectation value (VEV), and f represents SM fermions with mass m_f. As a consequence, for DELPHI (see Fig. 5), the decays of the singlet scalar into fermions ($s \to f\bar{f}$) will only affect the signals for the first two event candidates, *i.e.*, $\nu\ell\bar{\ell}$ and $\nu q\bar{q}$. However, the total decay width of the HNL Γ_N will increase and so will the probability for the HNL to decay inside the detector. Consequently, we replace Eq. (2.9) with the fraction that includes the additional events from the decays of s,

$$f_{w+s} = 2 \times \text{BR}(Z \to N\bar{\nu})\Big[\text{BR}_w \times (1 - e^{-D_L/L_N}) + \text{BR}_s \times (1 - e^{-D_L/(L_N+L_s)})\Big]\,, \tag{2.19}$$

where

$$\begin{aligned} \text{BR}_w &= \frac{\Gamma_N(\text{weak decays})}{\Gamma_N(\text{weak decays}) + \Gamma(N \to s\nu)}\,, \\ \text{BR}_s &= 1 - \text{BR}_w\,, \end{aligned} \tag{2.20}$$

and L_s, the mean decay length of the SM gauge singlet scalar s, is calculated following Refs. [36, 37].

At Belle, like for the DELPHI search, the N-s interaction introduces competition between 3-body weak decays and 2-body scalar decays of the HNL. But in contrast to DELPHI, now the $N \to s\nu$ decays cannot contribute to signal events, which are pions and charged leptons in the final state. Although s could decay to $\ell^+\ell^-$ or $\pi\pi$, it can never produce the combination $\pi\ell$ which is required by this search. Therefore, $N \to s\nu$ are invisible decays in the Belle analysis and these decays can only weaken the limit on $|U|^2$, independently of the size of the singlet-Higgs mixing angle θ.

At CHARM, in order to account for the singlet scalar decay channel, we modify Eq. (2.14) similarly to the recasting of DELPHI, making the replacement

$$\begin{aligned} e^{-d/L_N}\left(1-e^{-D_L/L_N}\right) \quad &\to \quad \mathrm{BR}_w\, e^{-d/L_N}\left(1-e^{-D_L/L_N}\right) \\ &+ \quad \mathrm{BR}'_s\, e^{-d/(L_N+L_s)}\left(1-e^{-D_L/(L_N+L_s)}\right), \end{aligned} \tag{2.21}$$

where we define

$$\mathrm{BR}'_s \equiv \mathrm{BR}_s \times \frac{\mathrm{BR}(s \to \ell\bar{\ell})}{\mathrm{BR}(N \to \ell'\ell\nu)}, \tag{2.22}$$

as the singlet s not always decays into light lepton pairs. This is similar to the case of Belle, where $\mathrm{BR}'_s = 0$, because the singlet scalar s cannot decay into $\pi\ell$.

2.4 Results

2.4.1 DELPHI

With the modifications to f previously mentioned, we obtain the upper bounds for $N-\nu$ mixing. For DELPHI, the new limits are shown in Fig. 9. The modified limits on $|U|^2$ can be understood as the result of the competition between HNL weak (three-body) and scalar (two-body) decays, through the factors BR_w and BR_s defined above, and the interplay between the altered decay length of the HNL $L_N(\mathrm{weak}+s)$ and that of s. For instance, the bottom right plot of Fig. 9 shows the weakened limits starting at the kinematic threshold $m_N > m_s = 8\,\mathrm{GeV}$. As the coupling g_s between the HNL and the singlet increases, $N \to s\nu$ decays become more prevalent. These are invisible decays at small mixing angle $\theta = 10^{-7}$, decreasing the number of signal events and weakening the limit on $|U|^2$. On the other hand, at larger singlet scalar-Higgs mixing $\theta \geq 5\times10^{-5}$, the scalar decays to $f\bar{f}$ with a short enough decay length for the final state particles to be observed as though they were coming from weak decays. We assume experimental

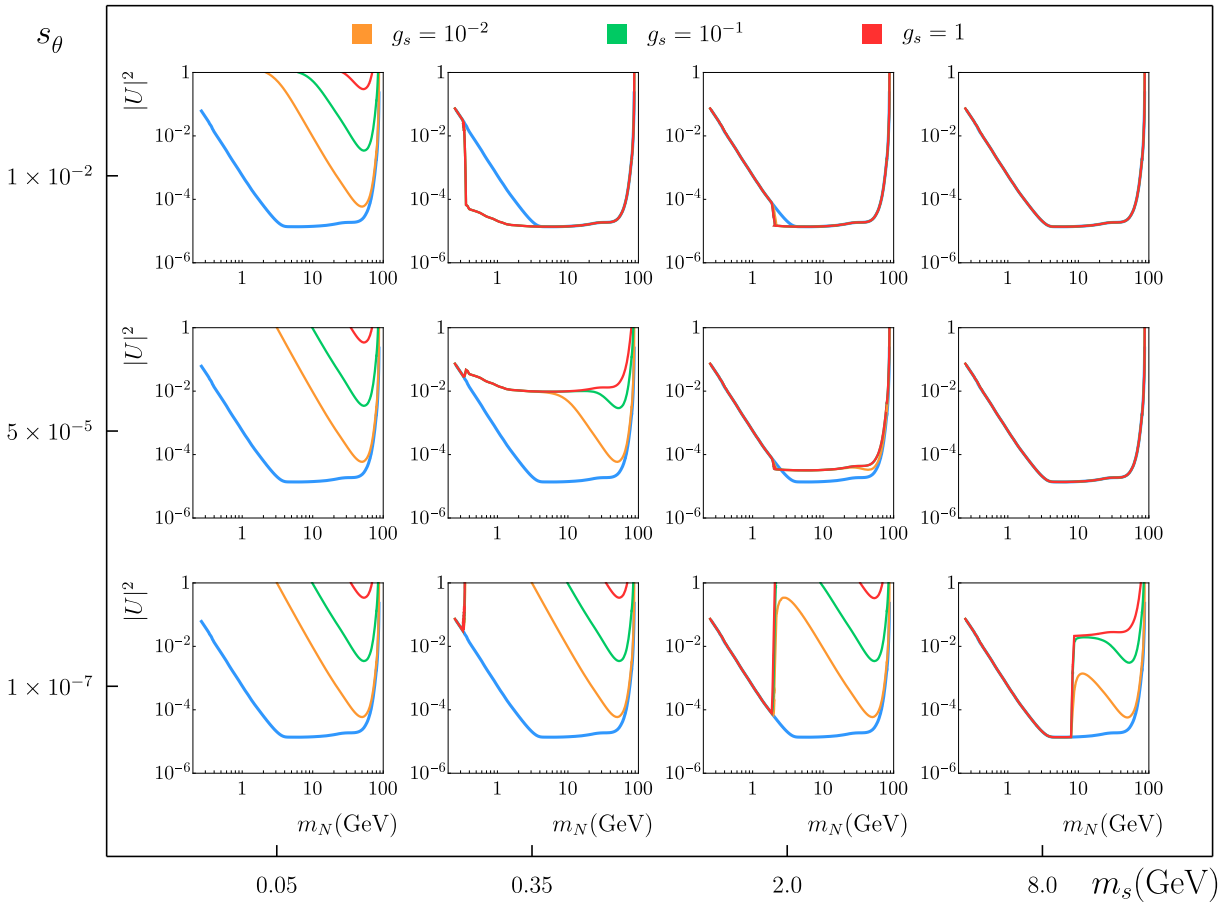

Figure 9 – **DELPHI:** Upper limits on $|U|^2$ for HNLs that couple to a light singlet scalar s, which mixes with the Higgs boson, in the HNL mass range from $2\,m_\mu$ up to m_Z at LEP. The blue contour is DELPHI's limit on $|U|^2$ at the 95% C.L. in the case of no singlet, which is independent on the HNL flavor (see figure 8).

sensitivity to these events to be similar to that for weak decays, resulting in an unmodified limit relative to the published result.

As we move to the left in Fig.9, for smaller values of m_s, the kinematic threshold discontinuity for $N \to s\nu$ also moves to the left, until the first column where it is no longer visible since $m_s < m_N$ for the range of m_N considered. The pattern described for the right-most column is similar, except that the decay length L_s is additionally increased by the small m_s, which suppresses $s \to f\bar{f}$ decays, leading to more invisible decays and generally weaker limits.

Exceptionally, there are several regions where the constraint on $|U|^2$ is strengthened. Most notably, this can be seen in the panel where $m_s = 350\,\text{MeV}$, $\theta = 10^{-2}$, $m_s < m_N \lesssim 4\,\text{GeV}$. It can be understood through the increased signal from $N \to s\nu$ followed by $s \to f\bar{f}$ in comparison to weak decays. This new excluded region eventually merges

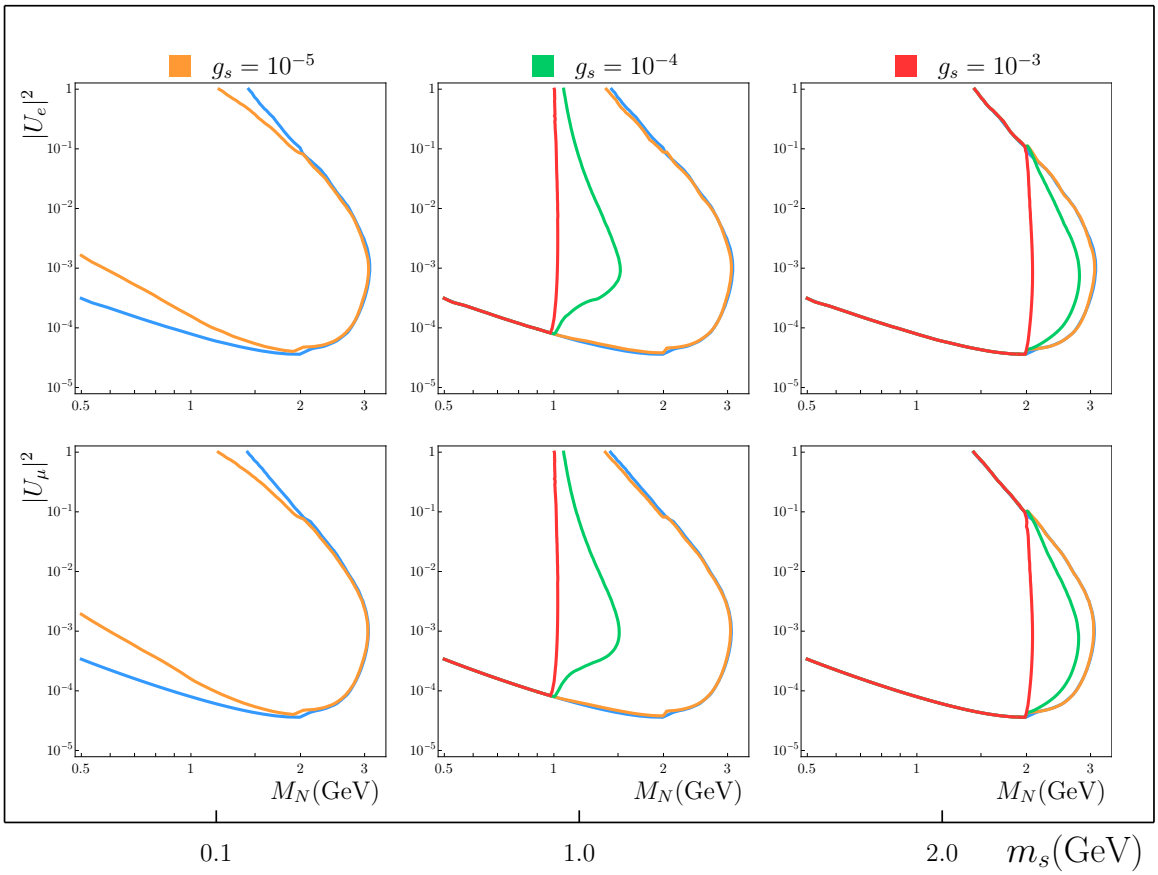

Figure 10 – **Belle:** Light blue curves show our reconstruction of the Belle limits on weak decays of heavy neutral leptons. Other colors show the relaxed constraints for different values of the coupling constant g_s due to $N \to s\nu$ decays.

back to the pure weak decay limit as m_N increases because the weak decay rate scales as m_N^5, while the two-body rate scales as m_N^3.

2.4.2 Belle

Fig. 10 shows our results for three choices of m_s and a range of values for g_s. As stated, the effect of the invisible decays is only to weaken the bounds. A borderline case appears when the coupling $g_s = 10^{-5}$ (green lines). We can see that at high HNL masses there is no change relative to the purely weak decay bounds. This is because the weak decays dominate in the region of large m_N as a consequence of their decay rate scaling as m_N^5 while the rate for $N \to s\nu$ goes as m_N^3. At lower m_N, provided that $m_s < m_N$ (left column), one can observe a weakening of the limits. On the other hand, for large enough g_s, the limits can disappear entirely when $m_s < m_N$.

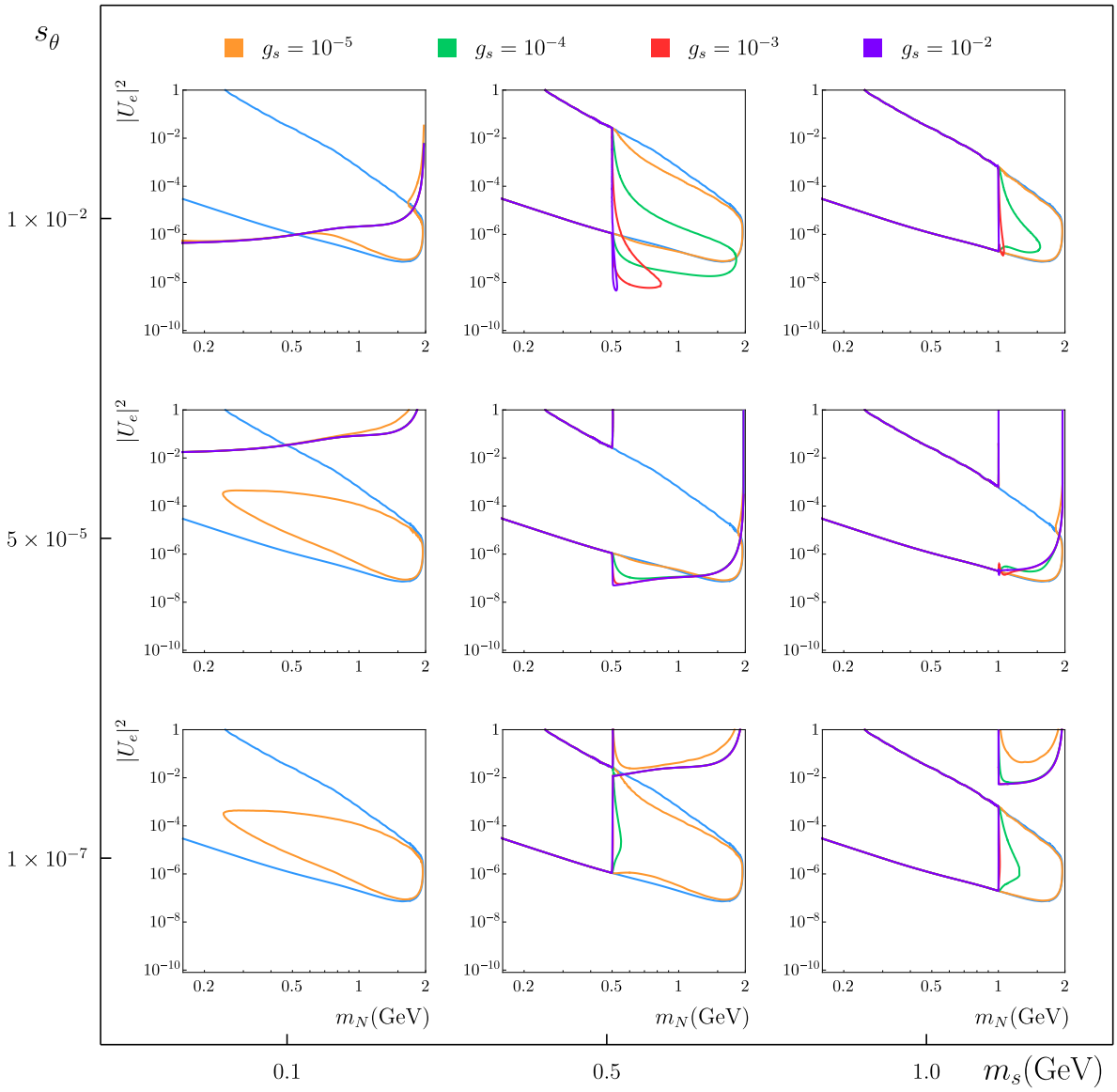

Figure 11 – **CHARM:** Recasted limits on $|U_e|^2$ versus HNL mass m_N on a grid of scalar mixing versus mass.

2.4.3 CHARM

The CHARM limits are sensitive to lepton flavor. Although the original CHARM analysis did not include U_τ constraints, Ref. [31] extended the published results to do so by including neutral current contributions to the decays of the HNL, and we have done likewise.

Similarly to the case of DELPHI, not only can constraints be weakened by the singlet decay channel, but also in some regions of parameter space the signal can be enhanced by singlet decays into $f\bar{f}$, which leads to new excluded regions when $\theta \times g_s$ is large enough. For example, in the upper left plot of Fig. 11, the singlet decays within the detector for

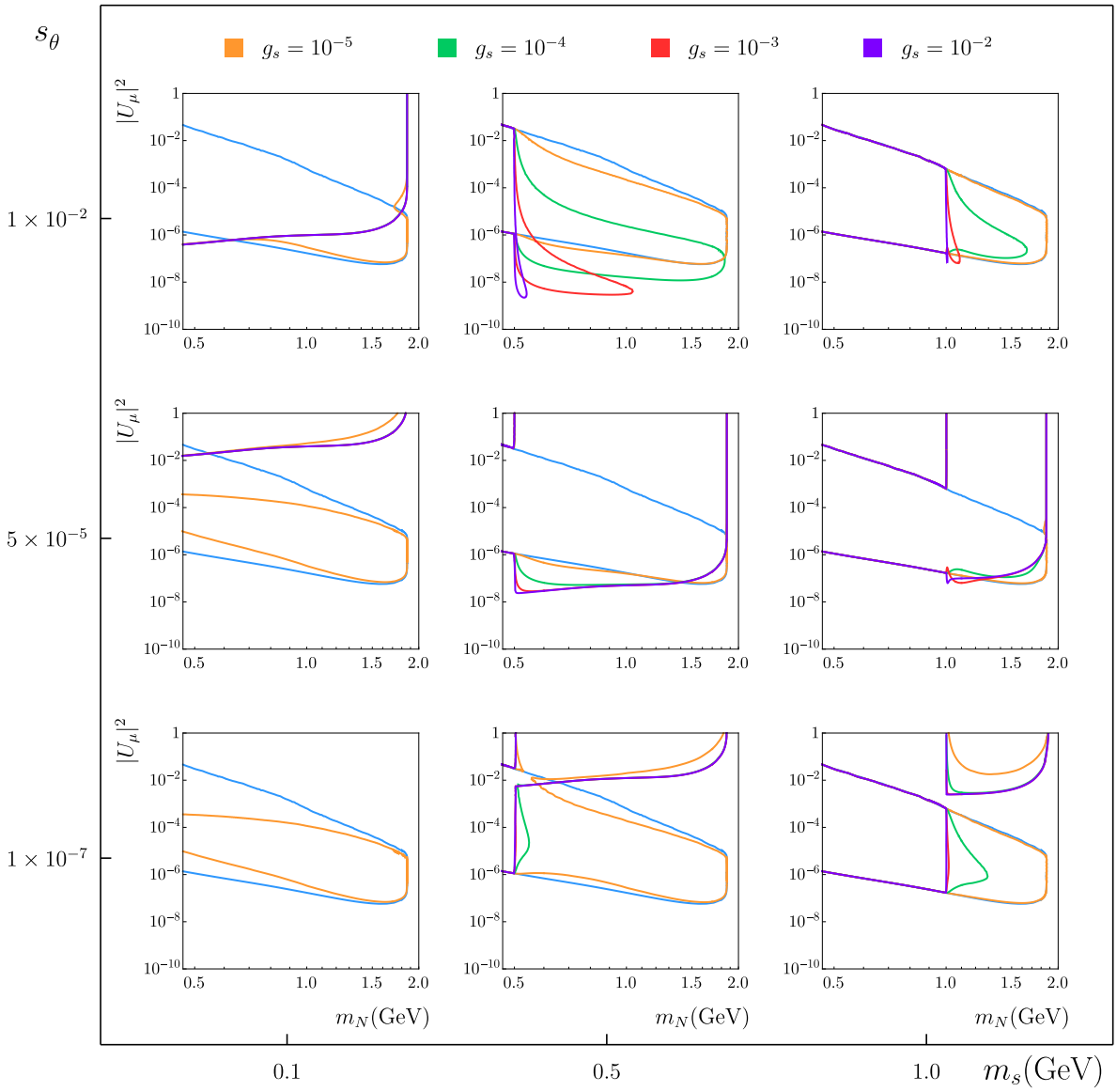

Figure 12 – **CHARM:** Like Fig. 12 but constraining $|U_\mu|^2$ from the CHARM experiment.

most values of g_s (even when $|U_e|^2 = 1$) allowing exclusion of large mixing angles. At larger m_s, the singlet starts to decay before reaching the experimental decay region and the upper boundaries on the excluded regions reappear. The bottom right graph has a disconnected excluded region at large $|U_e|^2$ because the singlet decay length starts to fall within the detection region. The constraints on $|U_\mu|^2$ shown in Fig. 12 are quite similar. The ones on $|U_\tau|^2$ in Fig. 13 are qualitatively distinct, but display similar general features. We used the results of Ref. [31] to calibrate the sensitivity curves at low values of $|U_\tau|$.

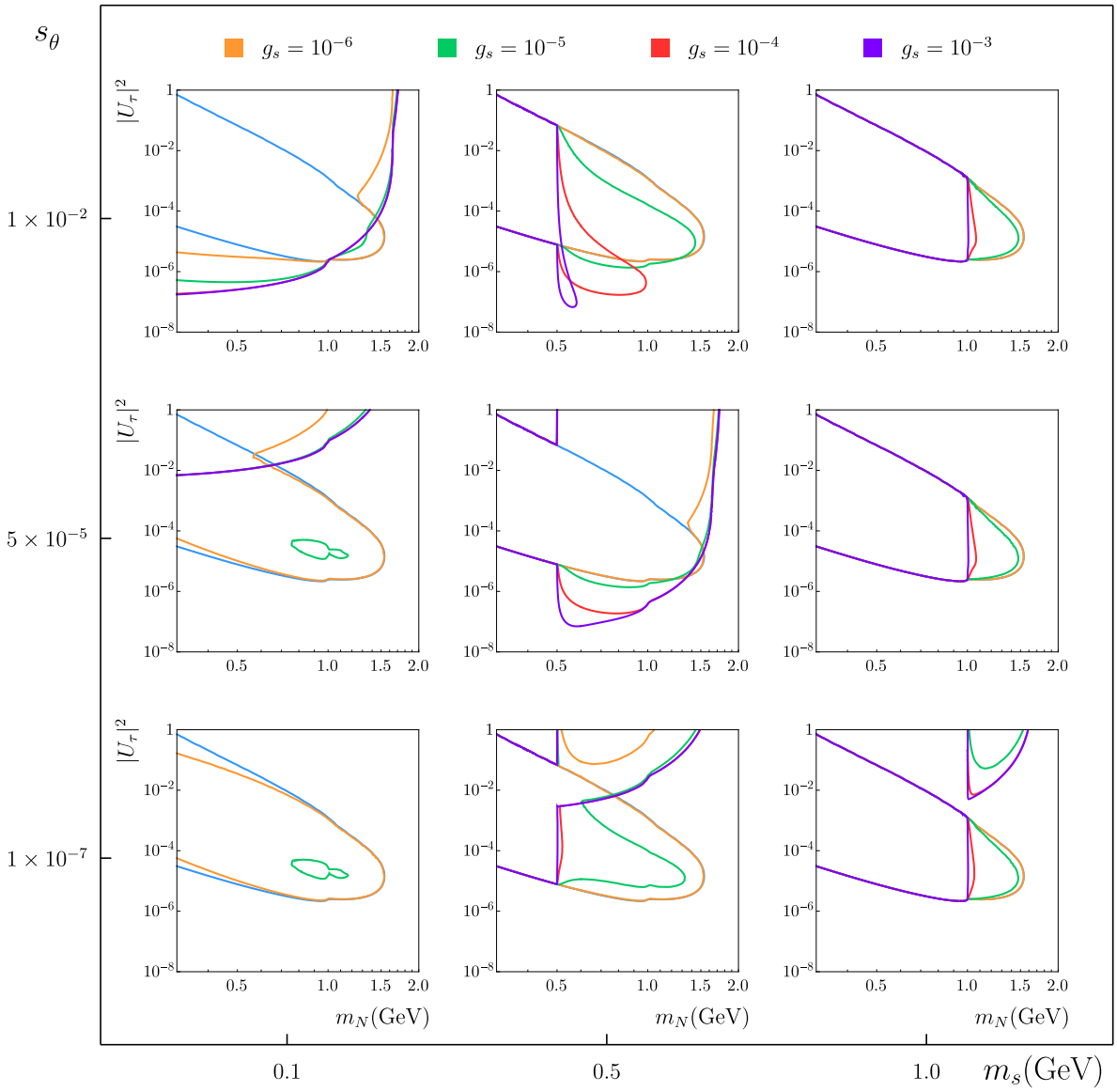

Figure 13 – **CHARM:** Recasted limits on $|U_\tau|^2$.

2.4.4 Relation to singlet scalar bounds

The Higgs mixing versus mass parameter space of the singlet $U - m_N$, in which we have displayed our recasted results for DELPHI and CHARM, is independently constrained by a variety of experiments or astrophysical considerations. In Fig. 14 we show how the regions considered in our previous results compare with the previously constrained parameter space [37]. There it can be seen that the largest mixing angle $s_\theta = 0.01$ we considered is ruled out by beam dump experiments or LHCb, except in the case of heavy singlets, $m_s \gtrsim 4\,\text{GeV}$. Moreover, for lighter singlets $m_s \lesssim 250\,\text{MeV}$, the region of small mixing angles $s_\theta \sim 10^{-7}$ that we have considered is excluded by the effects of singlet decays on supernova 1987A or by BBN. We have, nevertheless, included these regions in

our analysis to give a complete picture of the qualitative trends. It can be seen that our results overlap with a significant region of singlet parameters that is currently still open.

Just as the interactions of the singlet scalar with HNLs can alter the constraints on the HNL-active neutrino mixing angle, even if the singlet does not decay into the signal that a given experiment (*e.g.,* Belle) is looking for, they can also affect the constraints on the singlet scalar-Higgs boson mixing θ. These changes in the limits come from modifications of the production and decays of the heavy neutral lepton and the singlet scalar.

The HNL width can be increased by the new decay channel $N \to s\nu$ or by $N \to f\bar{f}\nu$ mediated by virtual s exchange, which compete with the weak HNL three-body decays. The singlet scalar width can be increased by $s \to N\bar{\nu}$ or the analogous process with off-shell N, which decays weakly. The on-shell decays $N \to s\nu$ and $s \to N\bar{\nu}$ open when $m_N > m_s$ and $m_s > m_N$, respectively. As these two regions of the full parameter space are mutually exclusive, our previous analysis is not affected by the new decay channels of the singlet. Off-shell contributions would not modify our results since these mediate processes like $s \to \bar{\nu}N^* \to \bar{\nu}\ell W$ which is kinematically forbidden for the light scalars studied in this work.

Regarding HNL production, one would expect it to be affected by the presence of the scalar singlet, since it inherits the couplings of the Higgs boson suppressed by the mixing angle theta. For Belle and CHARM, this is not the case because the probability of producing an HNL from a meson parent particle P is

$$\mathrm{BR}(P \to N) = \Gamma(P \to N) \times \tau_P, \tag{2.23}$$

where τ_P is an experimental value and the singlet does not affect $\Gamma(P \to N)$.

For DELPHI, HNLs can be produced in Z boson three-body decays $e^+e^- \to Z \to sZ^* \to sN\bar{\nu}$ [38], which are suppressed by s_θ^2 and kinematical factors in comparison with $Z \to N\bar{\nu}$ and $Z \to N\nu$. As a result,

$$\begin{aligned} \mathrm{BR}(Z \to N) &= \mathrm{BR}(Z \to N\bar{\nu}) + \mathrm{BR}(Z \to N\nu) \\ &+ \mathrm{BR}(Z \to sN\bar{\nu}) \\ &\approx \mathrm{BR}(Z \to N\bar{\nu}) + \mathrm{BR}(Z \to N\nu). \end{aligned} \tag{2.24}$$

For this reason, we expect small variations in HNL production.

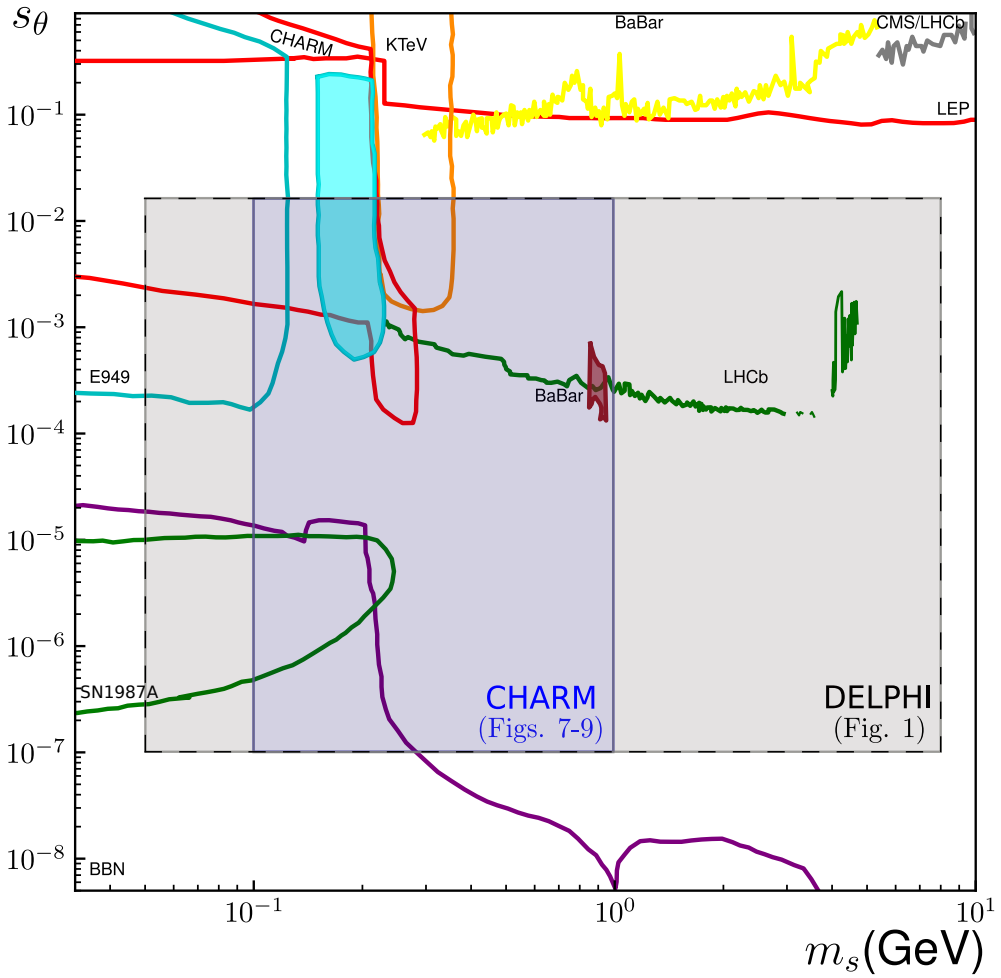

Figure 14 – Current bounds on singlet scalar-Higgs boson mixing from LEP [38], CMS [39], LHCb [40], CHARM [29], E949 [41], BaBar [42–44], KTeV [45], BBN [36], and SN1987a [37]. Black and blue boxes show the $s_\theta - m_s$ parameter space used to get the results presented in Fig. 9 and Figs. 11-13, respectively. The results for Belle (see Fig. 10) are independent from the singlet scalar-Higgs boson mixing θ. Limits adopted from [37].

2.5 Conclusions

In this chapter we have estimated the changes to HNL-active neutrino mixing bounds due to the new decay channel $N \to s\,\nu$, for HNL masses between 0.5 and $\sim 5\,\text{GeV}$. One motivation for focusing on this mass range is the possibility that one generation of such HNLs could be the DM of the Universe if the mixing is small enough [22], while the other generations would be subject to the constraints investigated here.

It is possible that the constraints derived here could be adapted to other qualitatively similar models. For instance, if HNLs couple to a light vector, Z', which kinetically mixes with the standard model hypercharge, it would give rise to effects that are similar to the ones studied here. In this case, g_s represents the new gauge coupling and θy_f maps onto

ϵe. Also, y_f is the fermion Yukawa coupling and ϵ is the kinetic mixing parameter.

Beyond the specific limits presented in this work, it may be that the general method described could be useful to recast other experimental constraints, especially in the case of older experiments, where access to their original data is not available or Monte Carlo simulations would be difficult to carry out.

3 Late-time dark matter oscillations

In this chapter we present a novel scenario for addressing the core-cusp problem – a long-standing small-scale discrepancy between ΛCDM predictions and observations of dark matter profiles in galaxies.

The content of this chapter is heavily based on Ref. [46], where our main results are published. These have been presented at the 3rd South American Dark Matter Workshop, ICTP-SAIFR, São Paulo, Brasil.

3.1 Motivation

3.1.1 The core-cusp problem

There is no doubt ΛCDM is a very successful model for the large scale structure of the universe. However, discrepancies with observations arise at small scales because structure formation is highly nonlinear. ΛCDM simulations show that the inner regions of cold dark matter halos present central cusps [47], in contrast with what is deduced from observations of rotation curves [48] which indicate constant 'cored' density profiles. This is the core-cusp problem and it represents a small-scale challenge for theoretical cosmology. See [49] for a review.

3.1.2 Oscillating asymmetric dark matter

The similarity in orders of magnitude of the dark matter (DM) and baryon densities, *i.e.* $\rho_{\rm DM}/\rho_{\rm B} \approx 5$, and the difference in mechanisms for producing these values, *e.g.* freeze-out for WIMPs and baryogenesis, call for an explanation. An initial asymmetry for the DM, similar to the baryon asymmetry, could link these densities to each other, thus providing a natural explanation for this ratio. See Ref. [50] for a review on theories of asymmetric dark matter.

In this scenario, where the DM density is set by its chemical potential, the symmetric DM component is depleted efficiently through annihilation and the relic DM abundance is fixed by the initial asymmetric component (asymmetric freeze-out), associated with

a conserved $U(1)_X$ symmetry. In the presence of tiny $U(1)_X$-violating mass terms, DM particle-antiparticle oscillations take place [51–55]. If oscillations turn on after freeze-out, the symmetric component, which did not survive the annihilations, is repopulated by these oscillations, and annihilations are reactivated. These residual annihilations can modify the DM relic density substantially [56] and they were thought to be avoided at late times [57].

The study of oscillating asymmetric dark matter (OADM) requires solving the generalized Boltzmann equations taking into account quantum coherence between particle and antiparticle [56, 58]. Here, the density matrix structure of the collision term depends strongly on the interaction governing the DM annihilation. Defining 'flavor' as the property of being a particle or antiparticle, the DM interaction is 'flavor-blind' or 'flavor-sensitive'. This difference will be reflected in the scattering term which does or does not lead to decoherence by measuring the flavor of the coherent state.

3.2 Boltzmann equations for OADM

Having discussed the motivation for oscillating asymmetric dark matter, let us focus on understanding the basics of the oscillation formalism required for phenomenological purposes. This subsection is based on Ref. [58] where the Boltzmann equations for OADM were derived from first principles.

First, let us consider a Dirac fermion χ as our dark matter candidate, which enters the theory through

$$\mathcal{L}_\chi = \bar{\chi}(i\partial\!\!\!/ - m_\chi)\chi. \tag{3.1}$$

Here χ is a mass eigenstate of the free Hamiltonian with eigenvalue m_χ in its rest frame. So, adding $U(1)_\chi$-invariant interactions to account for $\chi\bar{\chi}$ annihilations

$$\mathcal{L}_\chi = \bar{\chi}(i\partial\!\!\!/ - m_X)\chi + \mathcal{L}_{\rm int}, \tag{3.2}$$

does not alter this statement. The addition of a tiny Majorana-type mass term

$$\mathcal{L}_\chi = \bar{\chi}(i\partial\!\!\!/ - m_X)\chi - \frac{\delta m}{2}\left(\bar{\chi}^c\chi + \bar{\chi}\chi^c\right) + \mathcal{L}_{\rm int}, \tag{3.3}$$

where charge conjugation is defined by $\chi^c = -i\gamma^2\chi^*$ breaks this symmetry, causing the mass matrix M in the $\{\chi, \chi^c\}$ basis to have eigenvalues $m_\chi \pm \delta m$. Therefore, χ and χ^c

are no longer mass eigenstates and oscillations occur between them. For this reason, it is useful to define a flavor-like doublet $\Psi = (\chi, \chi^c)$ which allows us to write Eq.(3.3) in compact form

$$\mathcal{L} = \frac{1}{2}\bar{\Psi}\left(i\partial\!\!\!/ - M\right)\Psi + \mathcal{L}_{\rm int}, \qquad M = \begin{pmatrix} m_\chi & \delta m \\ \delta m & m_\chi \end{pmatrix}. \tag{3.4}$$

In order to describe the oscillation phenomenon between χ and χ^c, it is customary to work with the free Hamiltonian of the system $\mathcal{H}_k = \sqrt{k^2 + M^2}$ since mass eigenstates gain a phase $\exp(-iE_k t)$ when they propagate and $\omega_{\rm osc}(k) = \Delta E_k$ is the frequency of χ-χ^c oscillations. For instance, in the nonrelativistic limit we have $\omega_{\rm osc} \approx 2\delta m$.

Thus far, we have ignored interactions of our dark matter candidate with other particles in the dark sector or with standard model particles, and this is because $\mathcal{L}_{\rm int}$ is pretty much model dependent. For this reason, a first step would be to consider contact interactions resembling the Fermi four-fermion interaction and write

$$\mathcal{L}_{\rm int} = \frac{G_\chi}{2\sqrt{2}}\left(\bar{\Psi}\Gamma^i O_\pm \Psi\right)\left(\bar{f}\Gamma_i f\right), \tag{3.5}$$

where $i = S, V, P, A, T$ is the index for scalar $\Gamma^S = 1$, vector $\Gamma^V = \gamma^\mu$, pseudoscalar $\Gamma^P = \gamma^5$, axial vector $\Gamma^A = \gamma^\mu\gamma^5$, and tensor $\Gamma^T = \frac{i}{2}[\gamma^\mu, \gamma^\nu]$ interactions, f is a standard model or dark sector state, and $O_+ = \mathbb{1}_{2\times 2}$ and $O_- =$diag$\{1, -1\}$. This last notation $O_\pm$ is useful because of the following reason. In this formalism, annihilation and scattering amplitudes are arranged into matrices in 'flavor' space

$$\mathbb{M}_a = \begin{pmatrix} \mathcal{M}(\chi\bar{\chi} \leftrightarrow f\bar{f}) & 0 \\ 0 & \mathcal{M}(\chi^c\bar{\chi}^c \leftrightarrow f\bar{f}) \end{pmatrix}, \tag{3.6}$$

$$\mathbb{M}_s = \begin{pmatrix} \mathcal{M}(\chi f \leftrightarrow \chi f) & 0 \\ 0 & \mathcal{M}(\chi^c f \leftrightarrow \chi^c f) \end{pmatrix}. \tag{3.7}$$

In a process where the interaction discerns no difference between the two flavor states χ and χ^c, these matrices become proportional to the identity $\mathbb{1}_{2\times 2}$ and, therefore, they couple differently than if it did, *i.e.*

$$\mathbb{M}_a = \mathcal{M}(\chi\bar{\chi} \leftrightarrow f\bar{f})O_\pm, \quad \mathbb{M}_s = \mathcal{M}(\chi f \leftrightarrow \chi f)O_\pm. \tag{3.8}$$

For this reason, we can think of classifying interactions according to their being sensitive to $\chi \to \chi^c$ or not. So, if $\mathcal{L}_{\rm int}$ is invariant under $\chi \to \chi^c$, the interaction is termed flavor-blind. For example, scalar, pseudoscalar, and axial-vector interactions are of this type. On the other hand, vector and tensor interactions are flavor-sensitive.

The Boltzmann equations for the density matrix $\mathscr{F}_k$ read [58]

$$\frac{\partial \mathscr{F}_k}{\partial t} - Hk\frac{\partial \mathscr{F}_k}{\partial k} = -i[\mathcal{H}_k, \mathscr{F}_k] + \mathscr{C}[\mathscr{F}_k]. \tag{3.9}$$

In these equations, H is the Hubble rate, $\mathcal{H}_k$ is the free Hamiltonian

$$\mathcal{H}_k = \sqrt{k^2 + M^2}, \tag{3.10}$$

where k is the momentum of the DM particle and

$$\begin{aligned}\mathscr{C}[\mathscr{F}_k] &= -\frac{1}{2\omega_k}\int d\Pi_{k'} d\Pi_p d\Pi_{p'} (2\pi)^4 \delta^4(k + k' - p - p') \\ &\times \frac{1}{2s+1}\sum_{\text{spins}} \frac{1}{2}\Big(\{\mathscr{F}_k, \mathbb{M}_a^\dagger \overline{\mathscr{F}}_{k'} \mathbb{M}_a\}(1 \pm f_p)(1 \pm \overline{f}_{p'}) \\ &- \{\mathbb{1} \pm \mathscr{F}_k, \mathbb{M}_a^\dagger (\mathbb{1} \pm \overline{\mathscr{F}}_{k'})\mathbb{M}_a\} f_p \overline{f}_{p'} \Big),\end{aligned} \tag{3.11}$$

with $\omega_k = \sqrt{k^2 + m_X^2}$, corresponding to annihilation $\chi(k)\overline{\chi}(k') \longleftrightarrow f(p)\overline{f}(p')$. Here $+(-)$ is used for bosons (fermions), $f_p(\overline{f}_p)$ is the f (anti)particle distribution function with momentum p, and $d\Pi_k = d^3k/((2\pi)^3 2\omega_k)$.

The density matrix $\mathscr{F}_k$ and the 'barred' density matrix $\overline{\mathscr{F}}_k$ are

$$\mathscr{F}_k = \begin{pmatrix} \mathscr{F}_{11} & \mathscr{F}_{12} \\ \mathscr{F}_{21} & \mathscr{F}_{22} \end{pmatrix} \qquad \overline{\mathscr{F}}_k = \begin{pmatrix} \mathscr{F}_{22} & \mathscr{F}_{12} \\ \mathscr{F}_{21} & \mathscr{F}_{11} \end{pmatrix}. \tag{3.12}$$

Regarding the relativistic nature of our dark matter candidate, we consider it to be a cold relic, i.e. $x \equiv m_\chi/T > 1$ when decoupling from the primordial plasma, allowing us to treat it as a nonrelativistic particle throughout the evolution of the cosmos. This assumption enables the approximating of $\mathcal{H}_k$ to leading order in δm and the taking of the nonrelativistic limit of the free Hamiltonian $\mathcal{H}_0$,

$$\mathcal{H}_k = \sqrt{k^2 + M^2} \simeq \omega_k \mathbb{1} + \delta m \frac{m_X}{\omega_k}\sigma_1 \Longrightarrow \mathcal{H}_k \longrightarrow \mathcal{H}_0 = \begin{pmatrix} m_\chi & \delta m \\ \delta m & m_\chi \end{pmatrix}, \tag{3.13}$$

where σ_1 is the first Pauli matrix.

The master Boltzmann matrix equation for oscillating dark matter then reads

$$\frac{d}{dx}Y(x) = -\frac{i}{Hx}[\mathcal{H}_0, Y] - \frac{\Gamma_\pm}{2Hx}[O_\pm, [O_\pm, Y]] - \frac{s\langle\sigma v\rangle_\pm}{Hx}\left(\frac{1}{2}\left\{Y, O_\pm \overline{Y} O_\pm\right\} - Y_{eq}^2\right) \tag{3.14}$$

where $x = m_\chi/T$, $Y_{eq} = n_{eq}/s$, $s = \frac{2\pi^2}{45} g_{*S}(T) T^3$, $\Gamma_\pm$ is the scattering rate, and n_{eq} is defined by

$$n_{eq} \equiv 2\int \frac{d^3k}{(2\pi)^3}\exp(\omega_k/T) = \frac{m_\chi^3}{\pi^2}\frac{K_2(x)}{x}, \tag{3.15}$$

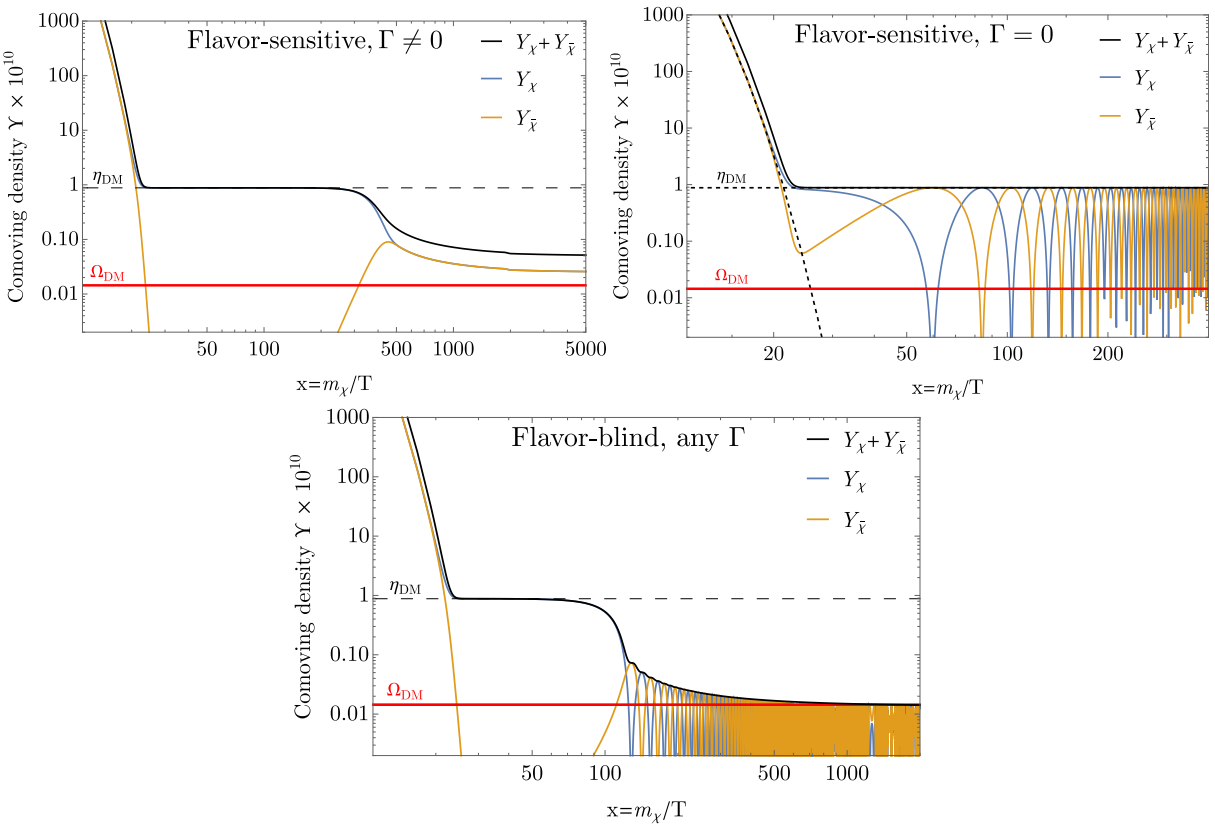

Figure 15 – DM density (black lines) for flavor-blind (bottom) and flavor-sensitive (top) interactions. Image reproduced from [58].

and $K_n(x)$ is the modified Bessel function of the second kind [59].

In Fig.15, we reproduced the results from Ref. [58] by solving the Boltzmann equations for m_χ=300 GeV, $\langle\sigma v\rangle$ =7.5 pb, $\delta m = 10^{-7}$eV, and $\Gamma = \kappa G_F T^5$, with $\kappa = 10^{-4}$. The dashed line is the initial DM asymmetry, which in this example is $\eta_{\rm DM} = 8.8 \times 10^{-11}$, and the red line is the observed DM relative density. Note that flavor-blind interactions do not care about the value of the scattering rate Γ (bottom panel). On the other hand, if this is turned off for flavor-sensitive interactions, there are no residual annihilations after freeze-out (upper right panel).

3.3 Vector and scalar models

In this section, we describe the models of oscillating asymmetric dark matter we will use to solve the core-cusp problem.

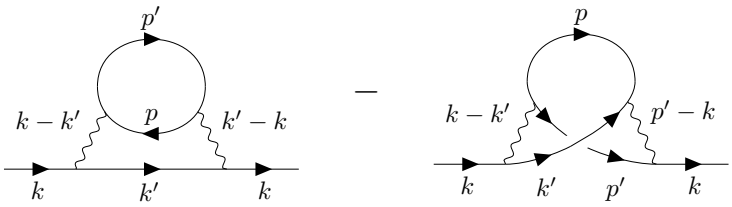

Figure 16 – Self-energy diagrams for the vector model (model 1).

3.3.1 Model 1: Vector mediator

We consider two models of quasi-Dirac fermionic DM χ. In the first model, DM couples to a lighter vector boson V^μ

$$\mathcal{L} \ni -\frac{1}{2}m_V^2 V_\mu^2 - g'\bar{\chi}\not{V}\chi. \tag{3.16}$$

The DM-number violating Majorana mass term is

$$\mathcal{L}_m = \frac{1}{2}\delta m(\bar{\chi}\chi^c + H.c.). \tag{3.17}$$

Since this interaction is *flavor-sensitive*, the set of Boltzmann equations read

$$Y' = -\frac{i}{xH}[\mathcal{H}, Y] - \frac{3\langle\sigma v\rangle_s\, s}{2xH}\begin{pmatrix} 0 & Y_{12} \\ Y_{21} & 0 \end{pmatrix}\mathrm{Tr}Y - \frac{3\langle\sigma v\rangle_a\, s}{xH}(\det Y - Y_{\rm eq}^2)\mathbb{1}_{2\times 2}, \tag{3.18}$$

where $H \simeq 1.67\sqrt{g_*}m_\chi^2/(M_p x^2)$ is the Hubble parameter and the collision term for elastic scattering of $\chi\chi$ or $\bar{\chi}\bar{\chi}$ through exchange of the vector boson is derived from the diagrams in figure 16 which are the analog of figure 4b in Ref. [58],

$$\langle\sigma v\rangle_s = \frac{I_s g'^4 m_\chi^{3/2} T^{1/2}}{4\pi m_V^4}, \tag{3.19}$$

where $I_s \approx 2.26$ (see Appendix A). For the annihilation cross section ($\chi\bar{\chi} \to VV$), we have

$$\langle\sigma v\rangle_a = \frac{\pi\alpha'^2}{m_\chi^2}\left[1 - \left(\frac{m_V}{m_\chi}\right)^2\right]^{3/2}\left[1 - \frac{1}{2}\left(\frac{m_V}{m_\chi}\right)^2\right]^2, \tag{3.20}$$

where $\alpha' = g'^2/4\pi$.

3.3.2 Model 2: Scalar mediator

In this second model, DM χ couples to a complex scalar $\Phi = \phi + i\,a$,

$$\mathcal{L} \ni -\frac{1}{2}m_\phi^2\phi^2 - \frac{1}{2}m_a^2 a^2 - g'\bar{\chi}(\phi + ia\gamma_5)\chi, \tag{3.21}$$

with the same DM-number violating term of Eq.(3.17). From Eq. (3.14), the set of Boltzmann equations now read

$$Y' = -\frac{i}{xH}\left[\mathcal{H}, Y\right] - \frac{\langle\sigma v\rangle_a\, s}{xH}\left[\begin{pmatrix} \det' Y & Y_{12}\mathrm{Tr}Y \\ Y_{21}\mathrm{Tr}Y & \det' Y \end{pmatrix} - Y_{\rm eq}^2 \mathbb{1}_{2\times 2}\right], \tag{3.22}$$

where $\det' Y = Y_{11}Y_{22} + Y_{12}Y_{21}$ and scatterings do not play any role, as expected for *flavor-blind* interactions. For the annihilation cross section ($\chi\bar{\chi} \to \phi a$), we have

$$\langle\sigma v\rangle_a = \frac{\pi\alpha'^2}{m_\chi^2}\left[1 - \frac{1}{4}\left(\frac{m_\phi}{m_\chi}\right)^2\right]^2, \tag{3.23}$$

where we have assumed for simplicity that $m_a \ll m_\phi$ and neglected the p-wave suppressed channels $\chi\bar{\chi} \to \phi\phi$ and $\chi\bar{\chi} \to aa$.

3.4 Structure formation

The Navarro-Frenk-White (NFW) profile reads [60],

$$\rho_{\chi,0}(r) = \frac{\rho_s}{(r/r_s)(1 + r/r_s)^2}, \tag{3.24}$$

where r is the distance from the center of the DM halo and ρ_s and r_s are parameters that vary from halo to halo. Because $\rho = m_\chi\, n$, we can use this profile as an initial condition assuming the DM halo has formed at some time t_0 (before oscillations have any effect) where the density matrix elements correspond to a pure χ state at each position r in the collapsed system,

$$\begin{aligned} n_{11}(r, t_0) &= \rho_{\chi,0}(r), \\ n_{12}(r, t_0) &= 0, \\ n_{21}(r, t_0) &= 0, \\ n_{22}(r, t_0) &= 0. \end{aligned} \tag{3.25}$$

The evolution of these elements of the density matrix is through the Boltzmann equations. In this case, the system is separated from the Hubble expansion, so we can drop the $3Hn$ term and set $n_{\rm eq} = 0$. For this reason, we solve

$$\dot{n} = -i\left[\mathcal{H}_0, n\right] - \frac{3}{2}\langle\sigma v\rangle_s\,(\mathrm{Tr}\, n)\begin{pmatrix} 0 & n_{12} \\ n_{21} & 0 \end{pmatrix} - \langle\sigma v\rangle_a \det n\, \mathbb{1}_{2\times 2}, \tag{3.26}$$

for the vector model (model 1) and

$$\dot{n} = -i\left[\mathcal{H}_0, n\right] - \langle\sigma v\rangle_a \left[\begin{pmatrix} \det' n & n_{12}\mathrm{Tr}\, n \\ Y_{21}\mathrm{Tr}\, n & \det' n \end{pmatrix} - \mathbb{1}_{2\times 2}\right], \tag{3.27}$$

for the scalar model (model 2). Results are shown in Fig.19.

In both cases, the initial NFW profile can be obtained by finding r_s and ρ_s from the virial radius r_{200}, concentration c_{200}, mass M_{200}, and velocity v_{200} through

$$\begin{aligned} \frac{\rho_s}{\rho_c} &= \frac{200}{3} c_{200}^3 g(c_{200}), \\ r_{200} &= c_{200} r_s, \\ M_{200} &= \frac{4\pi}{3} 200 r_{200}^3 \rho_c, \\ v_{200}^2 &= \frac{G\, M_{200}}{r_{200}}, \end{aligned} \tag{3.28}$$

where ρ_c is the present critical density, and $g_c^{-1} = \log(1+c) - c/(1+c)$.

For model 1, there is one more consideration to be made. Since $\langle\sigma v\rangle_a$ depends on the relative velocity v_{rel} between χ and $\bar{\chi}$, we need to specify the DM velocity profile. To do so, we adopted the analytical solution for the radial velocity disperion $\sigma_r(r)$ from Ref. [61], derived by solving the Jeans equation for a NFW profile. This determines $\sigma_r(r)$ for given NFW parameters r_s and ρ_s.

3.5 Results

3.5.1 Reactivation of oscillations at late times

From Eqs.(3.18) and (3.22), the cosmological evolution of χ, $\bar{\chi}$ and total abundances for model 1 and model 2 can be calculated. Results are shown in Fig.17. The model parameter values have been chosen in order to allow for oscillations to start before the epoch of structure formation. This allows annihilations to recouple during this period of time $t_s \sim 0.1$Gyr. If annihilations begin before, the DM relic density changes more than is allowed by CMB constraints [62]. Defining δ_η as the fractional change in the initial DM asymmetry η_{DM}, a value of $\delta_\eta \simeq 3\%$ is allowed by the CMB constraints. This leads to a window of allowed values for our models,

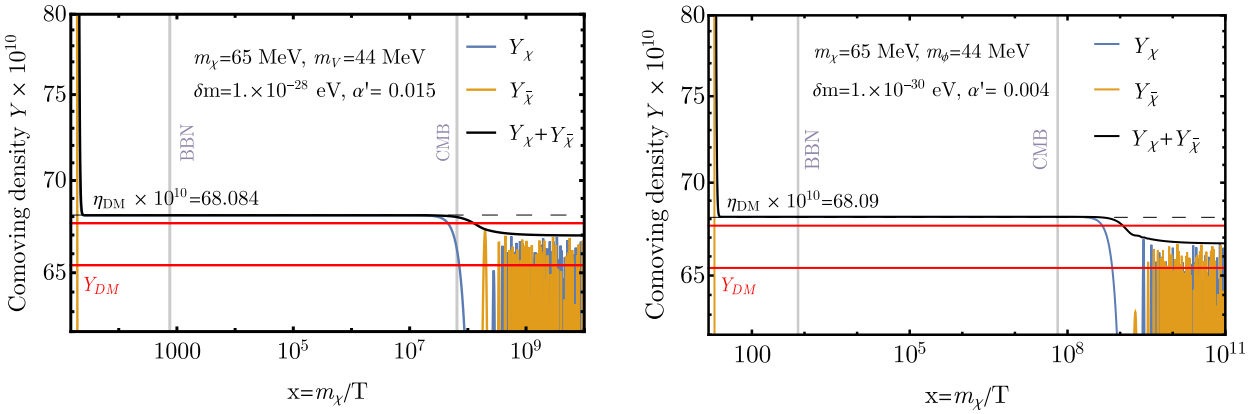

Figure 17 – Cosmological evolution of χ, $\bar{\chi}$ and total abundances for model 1 (left) and model 2 (right). We indicate the approximate time of BBN and CMB with vertical lines.

$$\frac{1}{t_s} \lesssim \delta m \lesssim \frac{16.3\,\delta_\eta^{1/2} m_\chi^{1/2}}{g_*^{1/4}\langle\sigma v\rangle_s \langle\sigma v\rangle_a^{1/2}\,\eta_{DM}^{3/2} M_p^{5/2}}, \tag{3.29}$$

for model 1 and

$$\frac{1}{t_s} \lesssim \delta m \lesssim \frac{342}{\sqrt{g_*}} \frac{\delta_\eta^{1/2}}{\langle\sigma v\rangle_a^2\,\eta_{DM}^2 M_p^3}, \tag{3.30}$$

for model 2 (see Appendix). Numerically, for the values used in Fig.17, we get

$$10^{-31}\text{eV} \lesssim \delta m \lesssim \begin{cases} 5\times 10^{-30}\text{eV} & (\text{ Model 1}) \\ 3\times 10^{-30}\text{eV} & (\text{ Model 2}) \end{cases} \tag{3.31}$$

3.5.2 Structure formation

We solved Eqs.3.26 and 3.27 for two systems. The first one is dwarf galaxy DDO 154 and the second one is galaxy cluster A2537. This choice was made because these systems are largely dominated by DM. Results are shown in Fig.19. As we can see, variations in the density profile are larger in denser regions (small r), while less dense regions remain practically unaltered by the reactivation of annihilations at late times.

For the vector model (model 1), since annihilations depend on the relative velocity $v_{\rm rel}$, this mechanism acts stronger on density profiles for galaxy cluster A2537 where velocity dispersion $\sigma_v \sim 1000$ km/s [63]. For the scalar model (model 2), the effect of late-time

annihilations is stronger for dwarf galaxy DDO 154. This occurs because this dwarf spheroidal galaxy is denser than galaxy cluster A2537.

In order to compare our results with the fits from SIDM [64] which , adjusted to the appropriate cross section, gives good fits to the rotation curves of DDO 154, we added their results (organge curves) to Fig.19. We note that, for model 1, the curves that approach the closest to SIDM results for DDO 154 favor lighter V's, while the curves do the same for A2537 prefer larger values of m_V. For model 2, where m_ϕ plays a minor role, the situation is the opposite. So, only α' matters. The SIDM profile can be approximately matched by taking $\alpha' = 0.01$ in the DDO 154 dwarf spheroidal galaxy, while for the same choice of parameters, the predicted inner profile of galaxy cluster A2537 lies somewhat above the SIDM fit.

One may also wonder to what extent a given model can match the observed properties of different spheroidal dwarf galaxies whose density profiles can be diverse. Although an exhaustive comparison is beyond the scope of the present work, we have studied a contrasting example which is DDO 126, whose DM density profile (like that of DDO 154) was estimated by ref. [65]. The best fits to the circular velocity measurements for the two galaxies occur at different values of the model parameters, as shown in the left panel of Fig. 18 for model 1, where we fixed $m_\chi = 65\,\mathrm{MeV}$ and $\alpha' = 0.015$, and allowed m_V to vary[1]. However, an acceptable fit to both systems can be found at an intermediate value $m_V \cong 20.6\,\mathrm{MeV}$, resulting in $\chi^2/\mathrm{d.o.f.} \cong 0.8$ for either system. We have allowed for systematic uncertainty in the magnitude of the DM density profiles reflecting an estimated $\sim 25\%$ uncertainty in the baryonic content of the galaxies [66]. Since the baryons comprise $\sim 10\%$ of these systems, this translates to a 2.5% uncertainty in the overall DM densities, that we have marginalized over to slightly improve the fits. For model 2, a mild tension in explaining the density profiles of both dwarf galaxies is also present (see right panel of Fig.18). Like for model 1, this is not a serious difficulty since an intermediate value $\alpha' \cong 0.0053$ results in an acceptable $\chi^2/\mathrm{d.o.f.} = 0.72$ for both systems.

Both model 1 and 2 face challenges when trying to simultaneously fit the rotation curves of dwarf galaxies and clusters. One possibility to overcome this problem is to have both scalar and vector mediators present in the model. This is a challenging task, so

[1] Notice we have chosen a lower value of m_χ in this example. This is motivated by the discussion in the next paragraph.

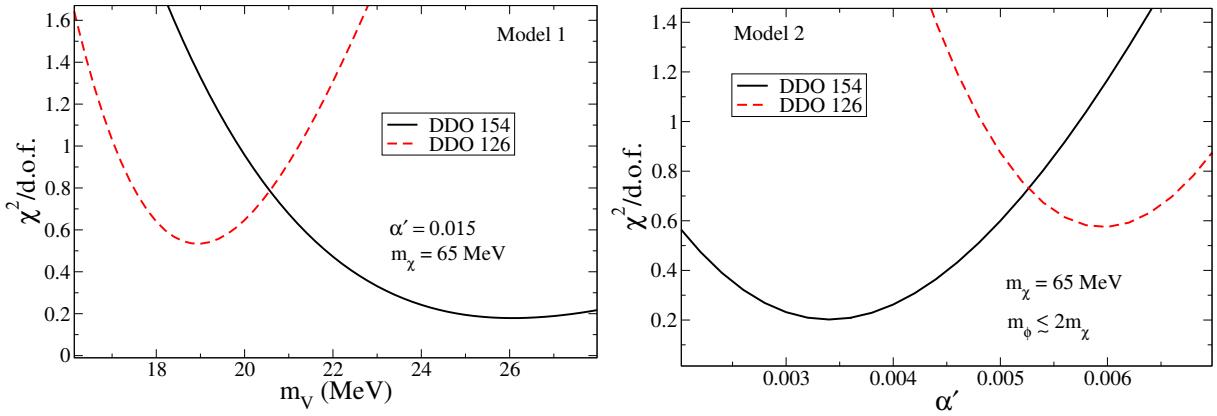

Figure 18 – **Left:** χ^2 per degree of freedom versus the vector mediator mass m_V in Model 1. Fits are made to the circular velocities of dwarf spheroidals DDO 154 and 126 with DM mass $m_\chi = 65\,\mathrm{MeV}$. **Right:** similar to left panel for Model 2. In either model, acceptable joint fits can be found by taking intermediate values of m_V or α', respectively.

here we will just give an example where the vector gives a good fit to a cluster, while leaving the dwarf spheroidal relatively unaffected and, at the same time, a scalar mediator achieves the opposite. An exhaustive analysis is left for future work.

Taking m_χ =65 MeV, and model 1 parameters $\alpha' = 0.015$, m_V =44 MeV, we fit the observed stellar line-of-sight velocity dispersion profile σ^*_{LOS} for A2537 extremely well. On the other hand, choosing $\alpha' = 0.004$ in model 2 gives an excellent fit to to dwarf spheroidal DDO 154 rotation curve (see Fig.20). In elastic SIDM, a cross section of $\sigma/m \simeq 3$ cm^2/g [64] is needed to agree with dwarf spheroidal galaxies, whereas 0.1 cm^2/g is used to explain clusters [66].

The theoretical analysis is supplemented by a complementary N -body simulations. Through this approach we can predict the evolution of galactic structures in a more quantitatively way. The theoretical approach and the N-body simulations should be viewed as complementary since each has its own limitations (see Appendix C in [46] for details). Results are shown in Fig.21 where we can see the N-body simulations for both models and their comparison with Fig.19 are in good agreement. This suggest the N-body simulations model reasonably well the physics encapsulated in the quantum Boltzmann equations where the coherence of DM particles plays a decisive role.

To compare our results with existing data, we calculated the circular velocity for dwarf galaxies and the projected stellar velocity along the line of sight for galaxy clusters, $v_{\mathrm{circ}}(r) = \sqrt{G\,M(r)/r}$, where $M(r)$ is the mass at radius r. The left panels of Fig.22 show

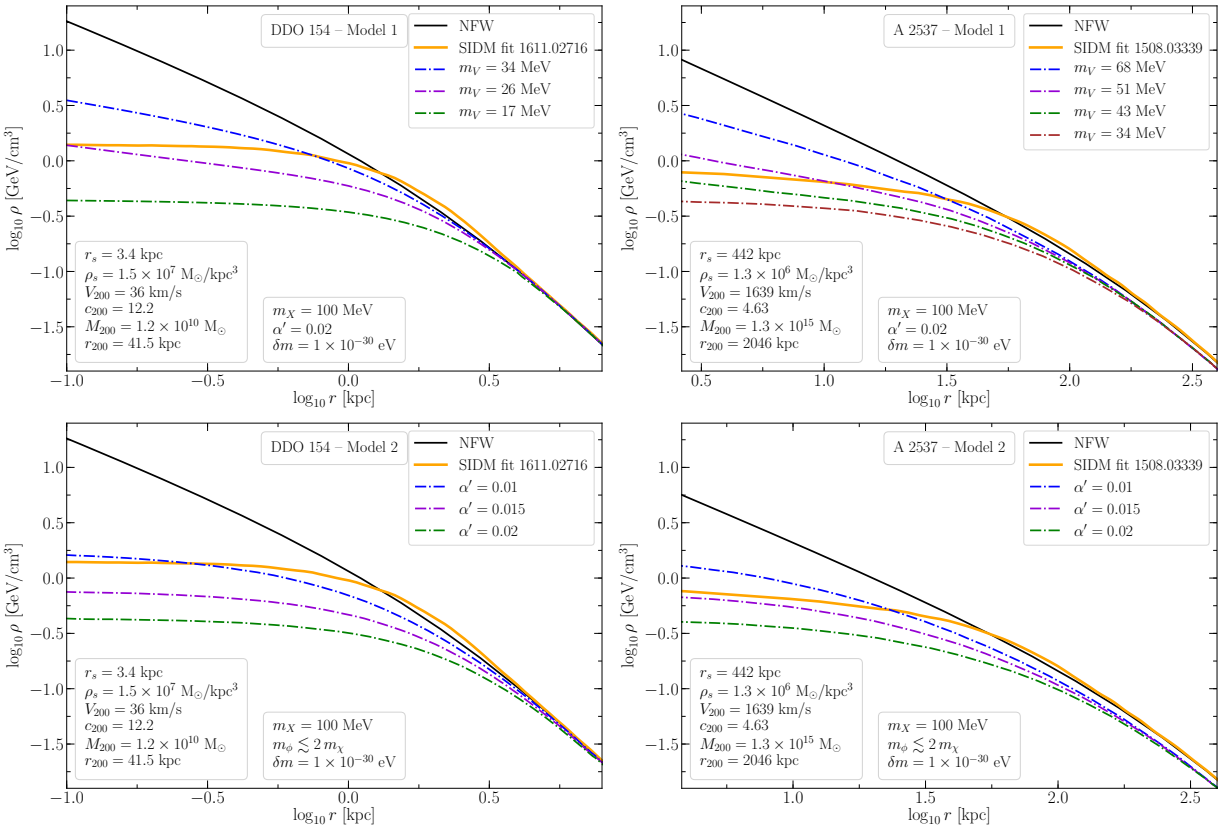

Figure 19 – **Left:** density profiles for dwarf spheroidal galaxy DDO 154. NFW and modified profiles from SIDM are from Ref. [64]. Dot-dashed curves are the predictions of Model 1 (Model 2) for different values of the vector mediator mass m_V (dark fine-structure constant $\alpha' = g'^2/4\pi$). **Right:** corresponding results for galaxy cluster A2537 where SIDM result is from Ref. [66].

our predictions for the rotation curve of DDO 154. The gray points show the total circular velocity of the dwarf galaxy as observed by the LITTLE THINGS survey [65], whereas the white points represent just the DM contribution to $v_{\rm circ}$, obtained by subtracting the gas and star components after carefully modeling their distribution within the galaxy. For A2537, it is possible to measure the stellar line-of-sight velocity dispersion profiles with spatially-resolved spectroscopy [63, 67]. As a result, in the right panel of Fig.22 we show our predictions for $\sigma^*_{\rm LOS}(r)$ are in good agreement with the existing data.

3.6 Conclusions

The long-standing discrepancies between ΛCDM gravitational N-body simulations of structure formation and observations of cored density profiles continue to motivate exploration of alternative DM models and mechanisms. In this work we have revived one of the earliest of such proposals [68] by showing that dark matter annihilations in galactic

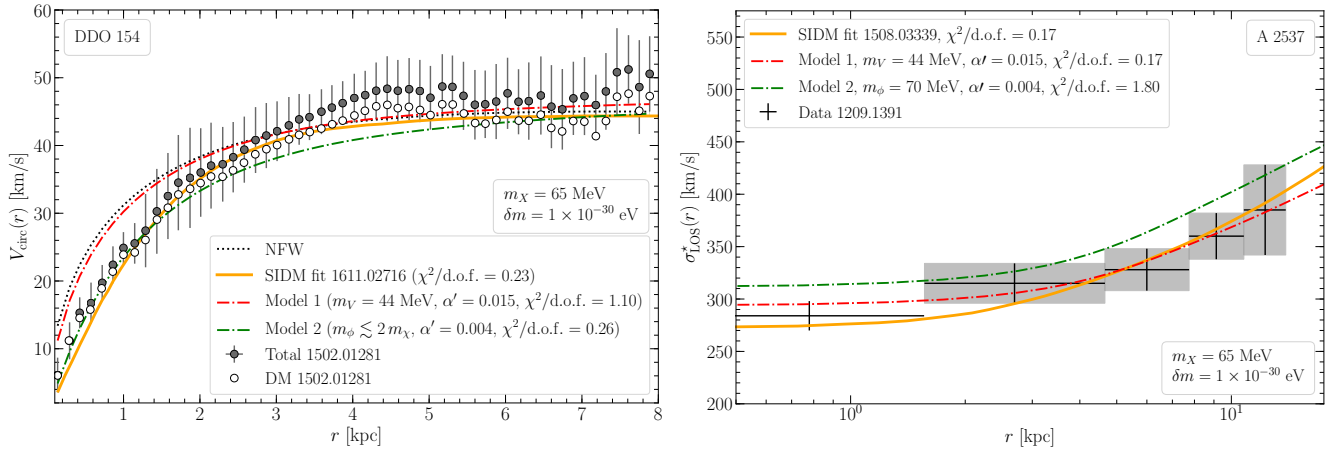

Figure 20 – Illustration of how combining vector and scalar mediators could give a good simultaneous fit for both dwarf spheroidal galaxies (left) and galaxy clusters (right). **Left:** predicted circular velocities due to the dark matter component alone from the same two models and from SIDM [64]. Data taken from Ref. [65]. In each case, one mediator dominates the coring effect of the central profile in one system while having little effect in the other system. **Right:** stellar velocity dispersion along the line-of-sight for galaxy cluster A2537 with predictions based on the dark matter density profile from two of our models, from SIDM [66]. Data taken from Ref. [63].

structures, like dwarf spheroidal galaxies and galaxy clusters, can be responsible for erasure of the cusps, using distinctive properties of asymmetric dark matter. The key idea is that very strong annihilations would freeze out early in cosmic history, thus solving the problem of removing the 'symmetric' ADM relic density, and are reactivated at late times (by oscillations of DM into its antiparticle) relevant for structure formation.

To obtain a large-enough annihilation cross section while respecting perturbativity of couplings, the DM and the mediator of the strong hidden force are to be light, typically below 100 MeV. We have illustrated the mechanism in two representative models, with vector or scalar mediators, respectively. We used two complementary approaches to model the structure formation dynamics. A fully consistent simulation is challenging because it must incorporate the quantum coherence of the oscillating dark matter while tracking the spatially-dependent annihilation rates within a DM halo. In our case, the N-body simulations, which treat the coherence in an approximate way, give relatively close results to a quantum Boltzmann equation approach. We have tested the scenario on two representative dwarf spheroidal galaxies, as well as a galactic cluster. Both methods lead to significant coring of the density profiles, qualitatively similar to the effects of elastic SIDM scattering that have been widely used to address the cusp-core problem.

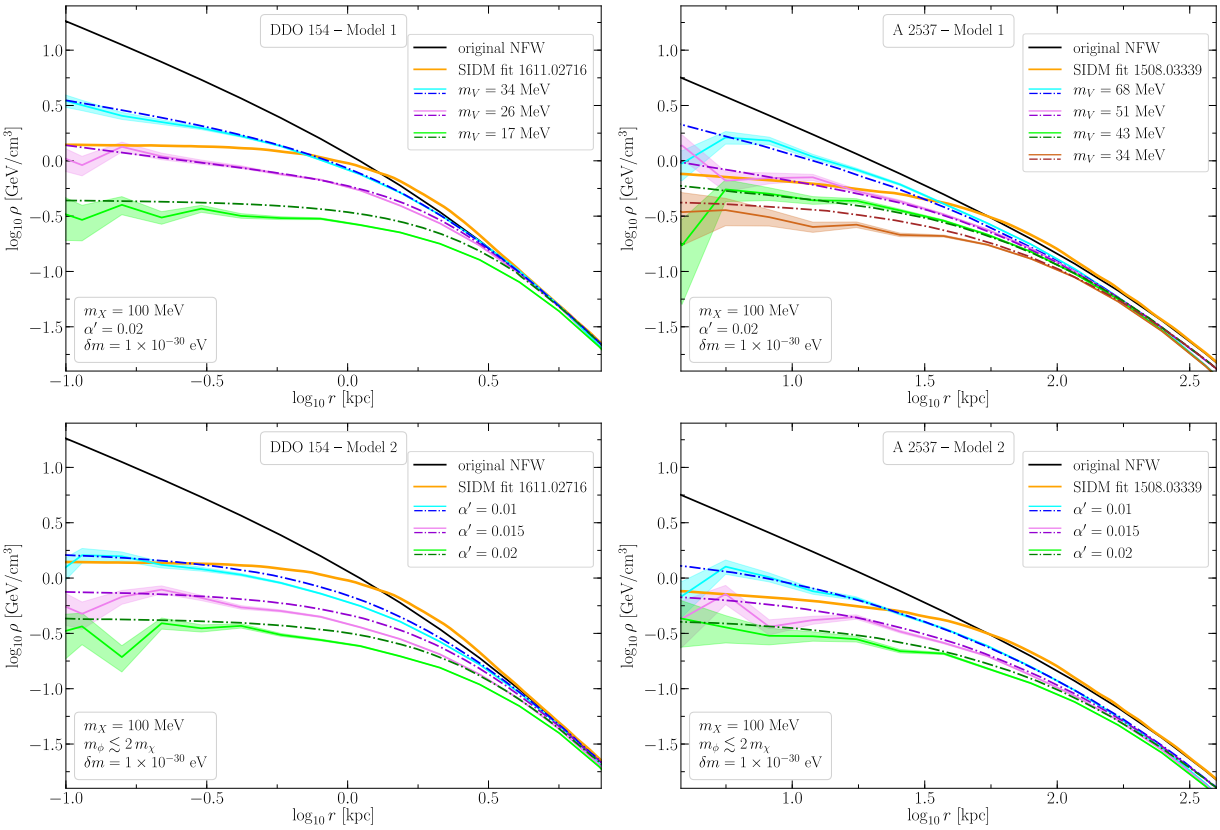

Figure 21 – Like Fig. 19, but now including the N-body simulation results. The latter are shown as solid lines surrounded by the 1σ uncertainty band.

Like the elastic SIDM paradigm, the new mechanism we propose in this work does not, in its simplest forms, address the diversity of halo profiles on all scales. In elastic SIDM, this is accomplished by assuming velocity-dependent scattering with a cross section that goes down at larger DM speeds. Within our mechanism, scalar mediators generically have a relatively stronger coring effect on small halos than larger (less dense) ones. Vector mediators have the opposite behavior. We presented evidence that the combination of both mediators could provide a good universal fit, leaving a detailed investigation for future study.

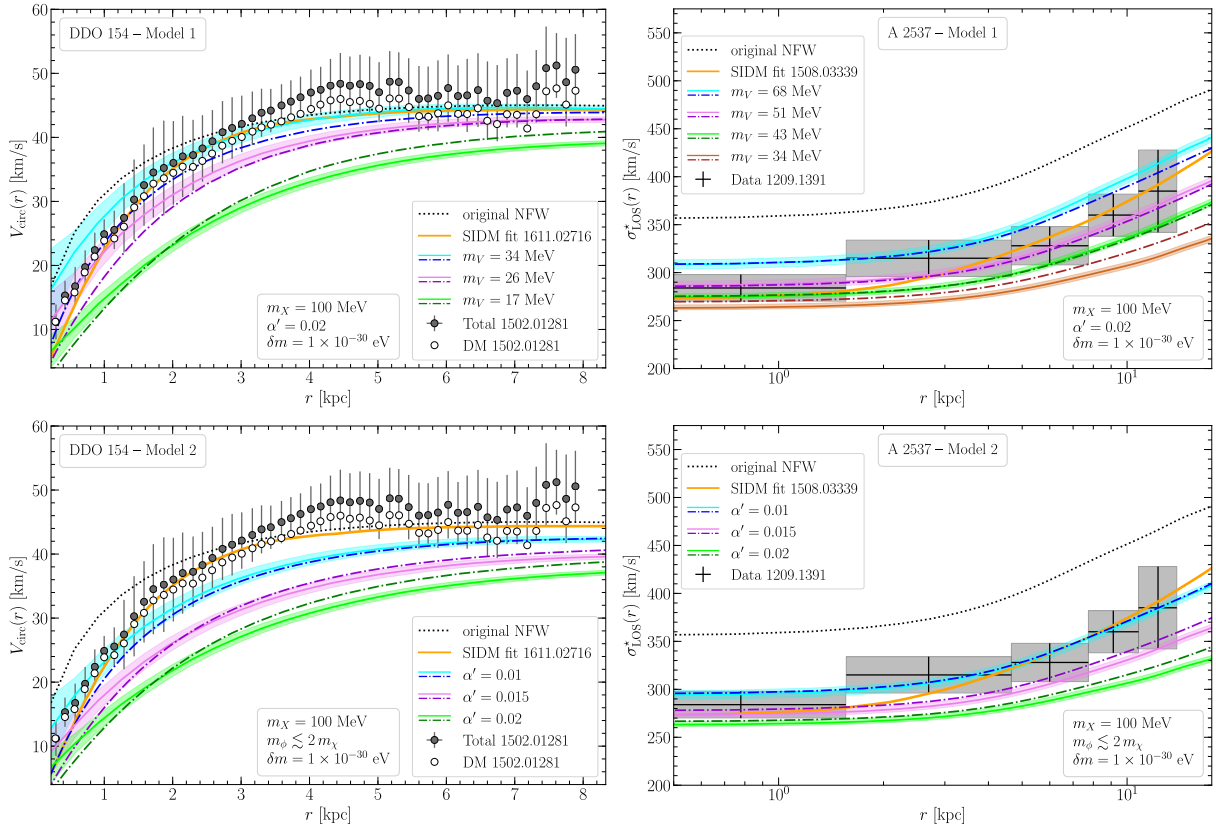

Figure 22 – Comparison between our model predictions and observational data. **Left:** circular velocity as a function of distance from the galactic center of the dwarf galaxy DDO 154. Data taken from Ref. [65]. In particular, the grey dots show the total effect of dark matter, gas, and stars on the rotation curve, whereas the white dots show just the dark matter contribution obtained after a careful modelling of stars and gas components (see Ref. [65] for details). **Right:** projected stellar velocity dispersion along the line-of-sight $\sigma^*_{\rm LOS}(r)$ as a function of radial distance r for galaxy cluster A2537. Data taken from ref. [63]. In all panels, N-body simulation results are shown as solid lines surrounded by the 1σ uncertainty band. The black dotted curve corresponds to the original NFW profile. The other dot-dashed curves are the results of Fig. 19. The orange solid line is the SIDM prediction from Ref. [64] for dwarf galaxy DDO 154 and from Ref. [66] for galaxy cluster A2537.

4 Constraints on new energy scales from dark matter decays

In this chapter we study how new physics scales, like the vacuum expectation value (VEV) responsible for $B-L$ spontaneous symmetry breaking (SSB), could be constrained when a new light scalar that decays into dark radiation in the form of neutrinos appears in the spectrum of the theory.

The content of this chapter is heavily based on our recent preprint [69], where our main results are published.

4.1 Motivation

A large amount of astronomical and cosmological observations is compatible with a cold relic whose self-interaction could solve, for example, small-scale problems [46, 49, 66, 70], while its interactions with SM particles could explain anomalies in terrestrial experiments [22, 71–74], as well as discrepancies between low-redshift and cosmic microwave background (CMB) determinations of the Hubble parameter H_0 and the matter perturbation amplitude σ_8 [75–78].

The resolution of these H_0 and σ_8 tensions [79–82] could also indicate the presence of a new neutrino species [83], primordial black holes [84], decaying dark matter [**?**, 85, 86], among others. In particular, a natural decaying DM candidate is the Majoron, which appears in models where the $B-L$ symmetry is broken by gravitational effects [87] or is spontaneously broken by the vacuum expectation value of a new complex singlet scalar [88]. If this CP-odd scalar decays predominantly into light neutrinos, it could largely modify the cosmological observables, so even if its relic density is negligible today, its history can rule-out a huge portion of the parameter space.

4.2 A gauged $B-L$ model with unstable dark matter

The model we use to study decaying dark matter is based on the gauge group $SU(3)_{\rm C}\otimes SU(2)_{\rm L}\otimes U(1)_{\rm Y'}\otimes U(1)_{\rm B-L}$, where C, L, Y′, and B–L stand for color, left chirality, a new charge different from SM hypercharge, and baryon minus lepton number, respectively. If we take B–L as a gauge symmetry, many models arise from the set of solutions to anomaly equations [89]. In Ref. [90], a model with three right-handed neutrinos with B–$L = 5, -4, -4$ charges was proposed. Its representation content is that of the SM slightly extended by these new particles and six new scalars, *i.e.* two doublets $\Phi_{1,2}$ and four singlets $\phi_{1,2,3,X}$, such that

$$SU(2)_{\rm L}\otimes U(1)_{\rm Y'}\otimes U(1)_{\rm B-L}\xrightarrow{\langle\phi\rangle} SU(2)_{\rm L}\otimes U(1)_{\rm Y}\xrightarrow{\langle H,\Phi\rangle} U_{\rm em}. \tag{4.1}$$

All of these new scalars have unique B–L quantum numbers [91] (see table 1). In this

Table 1 – Third component of the isospin, isospin, electric charge, Y', and B–L quantum number assignments for the fermions (left) and scalars (right)

Fermion	I_3	I	Q	Y'	B–L
ν_{eL}	1/2	1/2	0	0	-1
e_L	-1/2	1/2	-1	0	-1
u_L	1/2	1/2	2/3	0	1/3
d_L	-1/2	1/2	-1/3	0	1/3
e_R	0	0	-1	-1	-1
u_R	0	0	2/3	1	1/3
d_R	0	0	-1/3	-1	1/3
n_{1R}	0	0	0	4	-4
n_{2R}	0	0	0	4	-4
n_{3R}	0	0	0	-5	5

Scalar	I_3	I	Q	Y'	B–L
H^0	-1/2	1/2	0	1	0
H^+	1/2	1/2	1	1	0
Φ_1^0	-1/2	1/2	0	-4	3
Φ_1^-	1/2	1/2	-1	-4	3
Φ_2^0	-1/2	1/2	0	5	-6
Φ_2^-	1/2	1/2	-1	5	-6
ϕ_1	0	0	0	-8	8
ϕ_2	0	0	0	10	-10
ϕ_3	0	0	0	1	-1
ϕ_X	0	0	0	3	-3

model, the most general renormalizable and gauge-invariant scalar potential reads

$$\begin{aligned}
V_{B-L} \;=\; & -\mu_H^2 H^\dagger H + \lambda_H |H^\dagger H|^2 \\
& -\mu_{11}^2 \Phi_1^\dagger\Phi_1 + \lambda_{11}|\Phi_1^\dagger\Phi_1|^2 - \mu_{22}^2\Phi_2^\dagger\Phi_2 + \lambda_{22}|\Phi_2^\dagger\Phi_2|^2 - \mu_{s\alpha}^2|\phi_\alpha|^2 + \lambda_{s\alpha}|\phi_\alpha^*\phi_\alpha|^2 \\
& +\lambda_{12}|\Phi_1|^2|\Phi_2|^2 + \Lambda_{H\gamma}|H|^2|\Phi_\gamma|^2 + \Lambda_{Hs\alpha}|H|^2|\phi_\alpha|^2 + \Lambda'_{\gamma\alpha}|\Phi_\gamma|^2|\phi_\alpha|^2 + \Delta_{\alpha\beta}(\phi_\alpha^*\phi_\alpha)(\phi_\beta^*\phi_\beta) \\
& +\lambda'_{12}(\Phi_1^\dagger\Phi_2)(\Phi_2^\dagger\Phi_1) + \Lambda'_{H\gamma}(H^\dagger\Phi_\gamma)(\Phi_\gamma^\dagger H) \\
& +[\beta_{123}\phi_1\phi_2(\phi_3^*)^2 + \Phi_1^\dagger\Phi_2(\beta_{13}\phi_1\phi_3^* + \beta_{23}\phi_2^*\phi_3) - i\kappa_{H1X}\Phi_1^T\tau_2 H\phi_X \\
& -i\kappa_{H2X}(\Phi_2^T\tau_2 H)(\phi_X^*)^2 + \beta_X(\phi_X^*\phi_1)(\phi_2\phi_3) + \beta_{3X}(\phi_X^*\phi_3^3) + H.c.],
\end{aligned}$$

where $\gamma = 1, 2$, $\alpha, \beta = 1, 2, 3, X$, and $\alpha > \beta$ in the $\Delta_{\alpha\beta}$ terms. The quadratic potential is $V_2 = \frac{1}{2}\boldsymbol{\varphi}^\tau M \boldsymbol{\varphi}$, where $M = \partial^2 V_{B-L}/\partial\boldsymbol{\varphi}^2$. Interested in the CP-odd sector, we take $\boldsymbol{\varphi} = \{\mathrm{Im}_\varphi\}$ with $\varphi^0 = \frac{1}{\sqrt{2}}(v_\varphi + \mathrm{Re}_\varphi + \mathrm{Im}_\varphi)$ and $\varphi = H, \Phi_1, \Phi_2, \phi_1, \phi_2, \phi_3, \phi_X$.

In order to find the squared masses from M, we have found the roots of the eigenvalue equation $\det(\mathrm{M} - \lambda\,\mathrm{I}_{7\times7}) = 0$. This is a hard task because of the large number of free parameters, which forbid useful analytical expressions. For this reason, we departed from the 'general model' approach (where all couplings are independent) and proceeded to simplify the model as it was done in [91], assuming similar terms in V_{B-L} may have similar couplings. Namely,

$$\begin{aligned}
&\lambda_{11} = \lambda_{12} = \lambda_{s1} = \lambda_{s3} = \lambda_{sX},\\
&\Lambda_{H1} = \Lambda_{H1} = \Lambda_{H2} = \Lambda_{Hs1} = \Lambda_{Hs3} = \Lambda_{HsX} = \Lambda'_{H1} = \Lambda'_{H2},\\
&\Lambda'_{11} = \Lambda'_{13} = \Lambda'_{1X} = \Lambda'_{21} = \Lambda'_{23} = \Lambda'_{2X} = \lambda_{12} = \lambda'_{12} = \Delta_{13} = \Delta_{1X} = \Delta_{3X},\\
&\Lambda'_{12} = \Lambda'_{22} = \Delta_{12} = \Delta_{23} = \Delta_{2X},
\end{aligned} \tag{4.2}$$

and leave all other parameters free except for the VEVs of the new scalars, which we make v_D for all $\Phi's$ and v_M for all $\phi's$. Here $v_\mathrm{D} \ll v_\mathrm{SM} \approx 246$ GeV $\ll v_\mathrm{M}$. This choice was made in Ref. [91] in order to obtain significant phenomenological results and here we follow their work closely. In that article, the masses in the CP-odd scalar sector were found in the limit where $v_\mathrm{D}/v_\mathrm{M} \to 0$,

$$m^2_{I_3} = \mathcal{O}(v_\mathrm{D}/v_\mathrm{M}), \tag{4.3}$$

$$m^2_{I_4} = \frac{1}{2}\left[\Lambda_{Hs2}v^2_\mathrm{SM} + (\Lambda'_{12} + \lambda'_{22} - 2\Lambda_{Hs2})v^2_\mathrm{D} + (\Delta_{12} + \Delta_{23} + \Delta_{2X})v^2_\mathrm{M} - 2\mu^2_{s2}\right], \tag{4.4}$$

$$m^2_{I_{5,6}} = \frac{1}{4}v_\mathrm{M}\left[(1+\sqrt{2})v_\mathrm{SM} - 2\beta_{13}v_\mathrm{M} \mp \sqrt{4\beta^2_{13}v^2_\mathrm{M} + (3-2\sqrt{2})v^2_\mathrm{SM}}\right], \tag{4.5}$$

$$m^2_{I_7} = -5\beta_{3X}v^2_\mathrm{M}, \tag{4.6}$$

where I_i $(i = 1-7)$ are linearly-independent eigenvectors of the mass matrix M. Note that even if $m^2_{I_3}$ is not explicitly shown in Eq.(4.3), apart from the two Goldstone bosons, the remaining particles are much heavier than I_3, for their masses are proportional to the largest VEV v_M[1]. In this work we calculate m_{I_3} and show its correct relation with the new physics scales v_D and v_M.

[1] unless these are fine-tuned not to be so

A method to obtain approximate expressions for eigenvalues and eigenvectors is known as Rayleigh-Schrödinger perturbation theory [92–94], where the mass matrix is expanded in terms of a small parameter. In our case, $\zeta \equiv v_{\rm D}/v_{\rm M} \ll 1$ allows us to obtain, for instance, the zeroth-order eigenvector

$$I_3^{(0)} = \frac{1}{\sqrt{10}}{\rm Im}_{\phi_3} + \frac{3}{\sqrt{10}}{\rm Im}_{\phi_X}. \tag{4.7}$$

For the mass of I_3, we have found a better approximation using a different method (see Appendix C.3),

$$m_{I_3}^2 \simeq \frac{37\, v_{\rm SM}\, v_{\rm M}^2 v_{\rm D}^2\, \beta_{13}\, \beta_{3X}}{5\sqrt{2}(1+\sqrt{2}) v_{\rm M}^3 \beta_{13}\beta_{3X} - v_{\rm SM}\,(11 v_{\rm D}^2 \beta_{13} + 10 v_{\rm M}^2 \beta_{3X})}, \tag{4.8}$$

where $\beta_{13} < 0$ and $\beta_{3X} < 0$ because of the positivity of other two masses squared. Numerically, as $v_{\rm SM} \approx 246$ GeV and $v_{\rm SM} \ll v_{\rm M}$, for $\beta_{13} \sim \mathcal{O}(1)$ then

$$m_{I_3} \approx 0.73 \sqrt{\frac{v_{\rm D}}{1\ {\rm MeV}}} \sqrt{\frac{v_{\rm D}}{v_{\rm M}}}\ {\rm GeV}. \tag{4.9}$$

4.3 Observational limits

I_3 mainly decays into active neutrinos [91]. When including this into the dynamics of the different components in the universe, we can write the following equations

$$\dot{\rho}_{I_3} + 3H\rho_{I_3} = -\Gamma \rho_{I_3}, \tag{4.10}$$

$$\dot{\rho}_{\nu} + 4H\rho_{\nu} = \Gamma \rho_{I_3}, \tag{4.11}$$

$$\dot{\rho}_{m} + 3H\rho_{m} = 0, \tag{4.12}$$

where ρ_{I3} is the density of the unstable particle I_3, which produces an increase on the neutrino density ρ_ν. The stable cold dark matter is denoted by ρ_m and $\Gamma \approx \Gamma_{I_3 \to \nu\nu}$ is the total decay rate of I_3, which is given by [95]

$$\Gamma_{I_3 \to \nu\nu} \approx \frac{m_{I_3}}{16\pi} \frac{\sum_i m_{\nu_i}^2}{v_{\rm M}^2}. \tag{4.13}$$

Considering $\rm I_3$ does not decay before freeze-out, at temperature $\rm T_D \gtrsim m_t \approx 173$ GeV, its abundance can be written as [8, 96]

$$\Omega_{I_3,0}\, h^2 = \frac{m_{I_3}}{1.25\ {\rm keV}} \exp\left(-t_0/\tau\right), \tag{4.14}$$

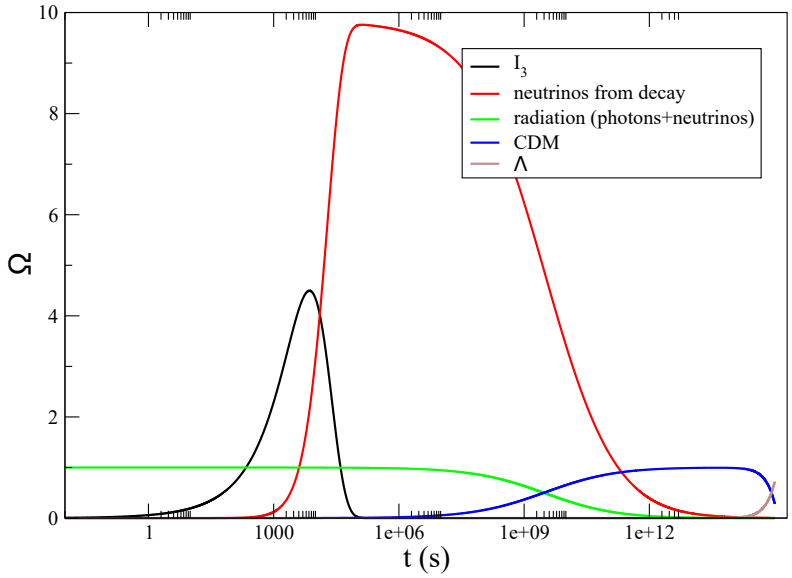

Figure 23 – Relative densities for the case $v_{\rm D} = 1$ MeV and $v_{\rm M} = 1$ TeV (see [91]).

where $\tau_{I_3} = 1/\Gamma$ is the lifetime of I_3 and t_0 is the age of the Universe.

Both the lifetime and the abundance of I_3 depend on $v_{\rm D}$ and $v_{\rm M}$, and the sum of neutrino squared-masses is a free parameter. Now, let's analyze the example from [91], *i.e.* $v_{\rm D} = 1$ MeV and $v_{\rm M} = 1$ TeV. Here, these values can give valid neutrino masses by means of the type-I seesaw mechanism and also the correct relic abundance for another DM candidate, which is stable, when a $\mathbb{Z}_2$ symmetry is imposed on the ϕ_2 singlet scalar. Using these values, we get

$$\tau_{I_3} \approx 0.1 \text{ year} \quad \text{and} \quad \Omega_{I_3,0}\, h^2 \approx 10^3 \exp\left(-t_0/(0.1 \text{ yr})\right). \tag{4.15}$$

In this case, I_3 represents a negligible fraction of the current dark matter in the universe. This is ok if there is another DM candidate that can account for the observed cold dark matter (CDM) relic density $\Omega_{cdm,0}$. Furthermore, we can calculate the amount of produced neutrinos from the decays of I_3 and check whether this value is in conflict with observations. We do this calculation by numerically integrating equations (4.10) to (4.12) with initial conditions for $\rho_{I_3,i}$ deduced from Eq. (4.14) and $\rho_{\nu,i} = 0$ for the neutrinos coming from the decays of I_3.

In Fig. 23 we see the fractional abundances in comparison with ΛCDM. Due to the large abundance of I_3 at early times, there is a period of cold dark matter (CDM) dominance driven by I_3 around $t \sim 1000$ s. When decays begin, the energetic content is populated by relativistic neutrinos, which would be the main ingredient in the Universe

until the cold dark matter starts to preponderate again. Such scenario would affect dramatically the cosmological observables and would hardly be acceptable by the latest perturbation data. Consequently, since some choices for the model parameters can affect the cosmology, we present in the following some weak limits on such parameters.

If I_3 is long-loved ($\tau_{I_3} \gg t_0$), it should not close the universe, *i.e.* $\Omega_{I_3} \lesssim 1$. From Eqs. (4.14) and (4.9),

$$\begin{aligned} \Omega_{I_3} &\approx \frac{m_{I_3}}{1.25\ \text{keV}} h^{-2}, \\ &\approx \frac{9\times 10^{-3}}{h^2}\left(\frac{v_{\rm D}}{\text{keV}}\right)\left(\frac{1000\ \text{TeV}}{v_{\rm M}}\right)^{1/2}, \\ &\approx \frac{9\times 10^{-3}}{h^2}\left(\frac{\text{Gyr}}{\tau_{I_3}}\right)\left(\frac{v_{\rm M}}{1000\ \text{TeV}}\right)^{2}, \end{aligned} \tag{4.16}$$

where we assumed $\sum m_\nu^2 = 5\times 10^{-3}\ \text{eV}^2$. As a result, we get an upper bound for the energy scale $v_{\rm M}$ of the $B-L$ SSB,

$$v_{\rm M} \lesssim 6.9\, h \left(\frac{\tau_{I_3}}{\text{Gyr}}\right)^{1/2} \times 10^3\ \text{TeV}. \tag{4.17}$$

Numerically, for instance, if $\tau_{I_3} = 100$ Gyr, using $h = 0.674$ we get

$$v_{\rm M} \lesssim 46.6 \times 10^3\ \text{TeV}. \tag{4.18}$$

For lower values of the lifetime of I_3, τ_{I_3}, we can make the following estimation. If at $t = \tau_{I_3}$ every I_3 particle converts *immediately* to neutrinos, then the energy density would decrease with an extra scaling factor of a, in comparison with the CDM. Assuming a matter dominated Universe, such event happens when

$$a \approx \left(\frac{3H_0\tau_{I_3}}{2}\right)^{2/3}.$$

Then,

$$\Omega_\nu h^2 \approx (H_0\tau_{I_3})^{2/3}\frac{m_{I_3}}{1.25\ \text{keV}} \approx (H_0\tau_{I_3})^{2/3}\, 10^{-7}\left(\frac{1\ \text{Gyr}}{\tau_{I_3}}\right)\left(\frac{v_{\rm M}}{1\ \text{TeV}}\right)^2.$$

Replacing the value of the Hubble rate, $H_0 \approx 0.1\, h\ \text{Gyr}^{-1}$, we get

$$\Omega_\nu h^2 \approx (0.1\, h)^{2/3} 10^{-7}\left(\frac{1\ \text{Gyr}}{\tau_{I_3}}\right)^{1/3}\left(\frac{v_{\rm M}}{1\ \text{TeV}}\right)^2.$$

Because $\Omega_\nu \lesssim 1$, for $\tau_{I_3} \approx 0.1$ yr, we get $v_{\rm M} < 76$ TeV. These numbers help us to restrict the space of parameters. However, we would expect much stronger restrictions when analyzing other cosmological observables. For instance, we can calculate the scale factor

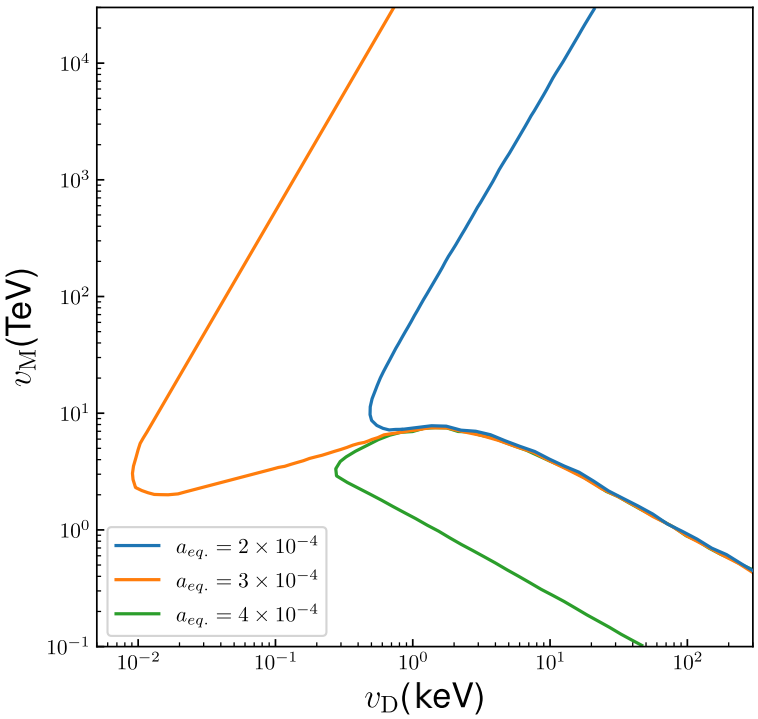

Figure 24 – Scale factor at matter-radiation equality in the model. For reference, $a_{eq} \sim 3 \times 10^{-4}$ is the ΛCDM prediction.

when the radiation and matter densities are equal to each other. A strong production of radiation (matter) would increase (decrease) the value of $a_{eq.}$, thus affecting the growth of structures or CMB asymmetries. One way to estimate the limit on the amount of dark radiation produced by the decays of I_3 particles would be to translate the limits on the number of neutrino families, given by [97], *i.e.* $N_{eff} = 2.99 \pm 0.17$, to a $3-\sigma$ interval in which the time of equality between radiation and non-relativistic species happens, arriving at

$$a_{eq.} = (3.0 \pm 0.2) \times 10^{-4}.$$

In Fig. 24 the scale factor of such equality is shown. The safe choice would be to stay on the left of both blue and green lines. Note that there is a fine-tuned region where the blue and green lines are almost indistinguishable and would produce the 'correct' scale factor $a_{eq.}$.

A fraction of the CDM of the universe could be allowed to decay into dark radiation. If initially (before decays) this fraction is $f_{\rm dcdm}$, strong limits on its decay rate $\Gamma_{\rm dcdm}$ has been put by a global analysis of both CMB and low redshift datasets [62, 98]. Here we

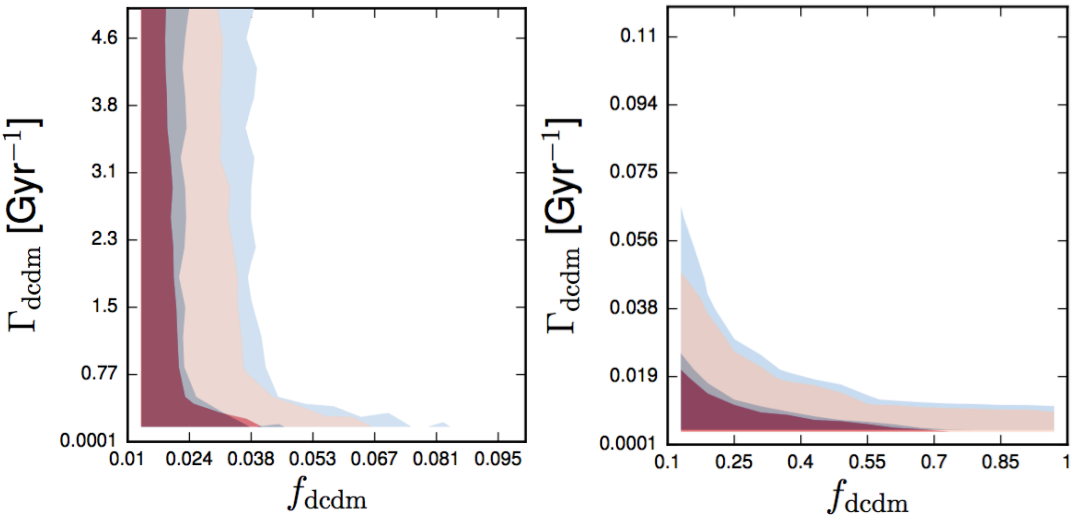

Figure 25 – Gravitational constraints on decaying DM fraction as a function of its total decay width. Image taken from [62].

show that using these limits, it is possible to put constraints on the new energy scales of the model. In Ref. [62], it was shown that if $\Gamma_{\rm dcdm} < H_0 \sim 0.07$ Gyr^{-1}, then $f_{\rm dcdm}\,\Gamma_{\rm dcdm} < \mathcal{O}(10^{-3})\,{\rm GeV}^{-1}$ (see Fig.25). On the contrary, if $\Gamma_{\rm dcdm} > H_0$, then $f_{\rm dcdm} \lesssim 0.04$. In this chapter, we use the most conservative of these bounds to search in the parameter space $v_{\rm M}$ vs. $v_{\rm D}$ the allowed regions for fixed values of $f_{\rm dcdm}$. Since the sum of neutrino squared-masses $\sum m_\nu^2$ is a free parameter, we proceed to analyze their limits. In the normal hierarchy, the lightest(heaviest) neutrino is $\nu_1(\nu_2)$ and the present limits on its mass are

$$\begin{aligned} 0 \leq \quad & m_{\nu_1} \quad \lesssim 30 \text{ meV} \quad \text{(Normal hierarchy)}, \\ 49.9 \text{ meV} \lesssim \quad & m_{\nu_2} \quad \lesssim 52.3 \text{ meV} \quad \text{(Inverted hierarchy)}. \end{aligned} \tag{4.19}$$

These masses can affect the sum of squared-masses according to the following expression

$$\sum_{i=1}^{3} m_{\nu_i}^2 = \begin{cases} 3\,m_{\nu_1}^2 + \Delta m_{\rm Sun}^2 + \Delta m_{\rm atm}^2 & \text{(NH)}, \\ 3\,m_{\nu_2}^2 - \Delta m_{\rm Sun}^2 + \Delta m_{\rm atm}^2 & \text{(IH)}. \end{cases} \tag{4.20}$$

Therefore, upper and lower bounds for $\sum m_{\nu_i}^2$ are approximately (see Fig.(27))

$$\begin{aligned} 2500 \text{ meV}^2 \lesssim \quad & \textstyle\sum m_{\nu_i}^2 \quad \lesssim 5200 \text{ meV}^2 \quad \text{(Normal hierarchy)}, \\ 4900 \text{ meV}^2 \lesssim \quad & \textstyle\sum m_{\nu_i}^2 \quad \lesssim 5600 \text{ meV}^2 \quad \text{(Inverted hierarchy)}. \end{aligned} \tag{4.21}$$

We calculated the values of $\sum m_{\nu_i}^2$ using Eq.(4.20), the central values of $\Delta m_{\rm Sun}^2$ and $\Delta m_{\rm atm}^2$ from [99], and $\sum m_\nu$ <120 meV [100].

For reference, it is convenient to rewrite Eq.(4.9) and Eq.(4.13) as

$$\frac{m_{I_3}}{\rm eV} \approx 23.1 \left(\frac{v_{\rm D}}{\rm keV}\right) \left(\frac{1000 \text{ TeV}}{v_{\rm M}}\right)^{1/2}, \tag{4.22}$$

$$\frac{\tau}{\text{Gyr}} \approx 9.1 \left(\frac{5\times 10^{-3}\ \text{eV}^2}{\sum m_\nu^2}\right)\left(\frac{\text{keV}}{v_\text{D}}\right)\left(\frac{v_\text{M}}{1000\ \text{TeV}}\right)^{5/2}. \tag{4.23}$$

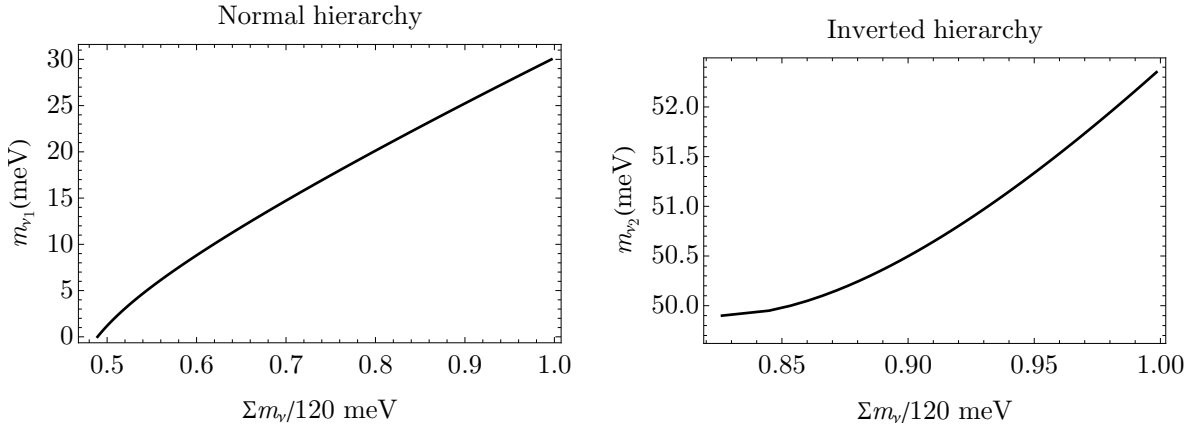

Figure 26 – Upper and lower bounds on m_{ν_1} and m_{ν_2} as functions of $\sum \nu$ for the normal and inverted hierarchy, respectively.

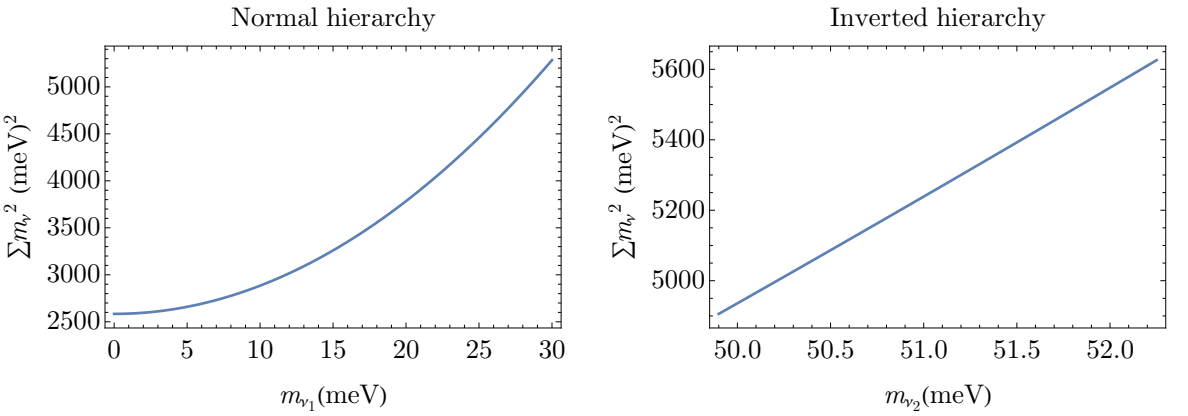

Figure 27 – Constraints on the sum of neutrino squared masses for the normal and inverted hierarchies.

4.4 Results

If we assume an initial dark matter relative density $\Omega_\text{dm}^\text{ini}$ with an initial stable component $\Omega_\text{sdm} = (1 - f_\text{dcdm})\Omega_\text{sdm}^\text{ini}$, then

$$\begin{aligned}\Omega_\text{dm} &= \Omega_\text{sdm} + \Omega_\text{dcdm} \\ &= \left[(1 - f_\text{dcdm}) + f_\text{dcdm}\, e^{-\Gamma_\text{dcdm} t}\right] \Omega_\text{dm}^\text{ini}.\end{aligned} \tag{4.24}$$

In this case, the present value of the DM relative density reads

$$\Omega_{dm} = \frac{m_{I_3}}{1.25\ \text{keV}}\, h^{-2}\left(\frac{1 - f_\text{dcdm}}{f_\text{dcdm}} + e^{-\Gamma_{I_3} t}\right). \tag{4.25}$$

Our results are presented in Figs. 28 and 29 where white regions indicate the values for Γ_{I_3} compatible with the bounds shown in Fig.25. Also, blue regions are excluded because the decay rate Γ_{I_3} is too large for a given $f_{\rm dcdm}$, and green regions are excluded because $\Gamma_{\rm dcdm} > H_0$ and $0.04 \leq f_{\rm dcdm}$. Moreover, black curves indicate different results for the DM relative density and colored dotted curves represent the different values for the lifetime of I_3 (in Gyr). For instance, below the blue dotted curve (13.8 Gyr), $\tau_{I_3} < t_0$ (the age of the universe).

4.5 Conclusions

A model containing a DM candidate should predict its right abundance today. However, this is not enough for successful model building. The model analysed here presents some regions on the parameter space that produce the right amount of dark matter, but it also presents some discrepancies with the standard cosmological model due to a very high production of dark radiation in the form of neutrinos, which, for instance, would distort the CMB anisotropies.

The dark matter of the universe could be multi-component. The lifetime of its decaying component is strongly constrained when the produced dark radiation is in the form of neutrinos, gravitational waves or other new relativistic degrees of freedom. In the model studied in this chapter, the unstable dark matter candidate I_3 decays mainly into light neutrinos, allowing us to use the sum of their squared-masses and the fraction $f_{\rm dcdm}$ of unstable DM before decays begin ($\Omega^{\rm ini}_{\rm dcdm} = f_{\rm dcdm}\,\Omega^{\rm ini}_{\rm dm}$) as free parameters to constraint the new energy scales $v_{\rm D}$ and $v_{\rm M}$. The latter is the vacuum expectation value responsible for $B-L$ spontaneous symmetry breaking and the former is the VEV responsible for dynamically generating Dirac neutrino masses.

Our results show that, even if taking the most conservative limits on $\Gamma_{\rm dcdm}$, a large area in the parameter space is ruled-out when the decaying dark matter candidate I_3 represents a significant amount of the initial CDM ($> 4\%$) and its total decay rate is lower than the present Hubble parameter, *i.e.* $\Gamma(I_3 \to \nu\nu) < H_0$, or when the decay rate of I_3 is larger than the present value of the Hubble rate and $f_{\rm dcdm} > 0.04$. The strongest bounds come from the present value of the total dark matter relative density. These are dominant when the initial fraction of decaying dark matter component is of a few percent.

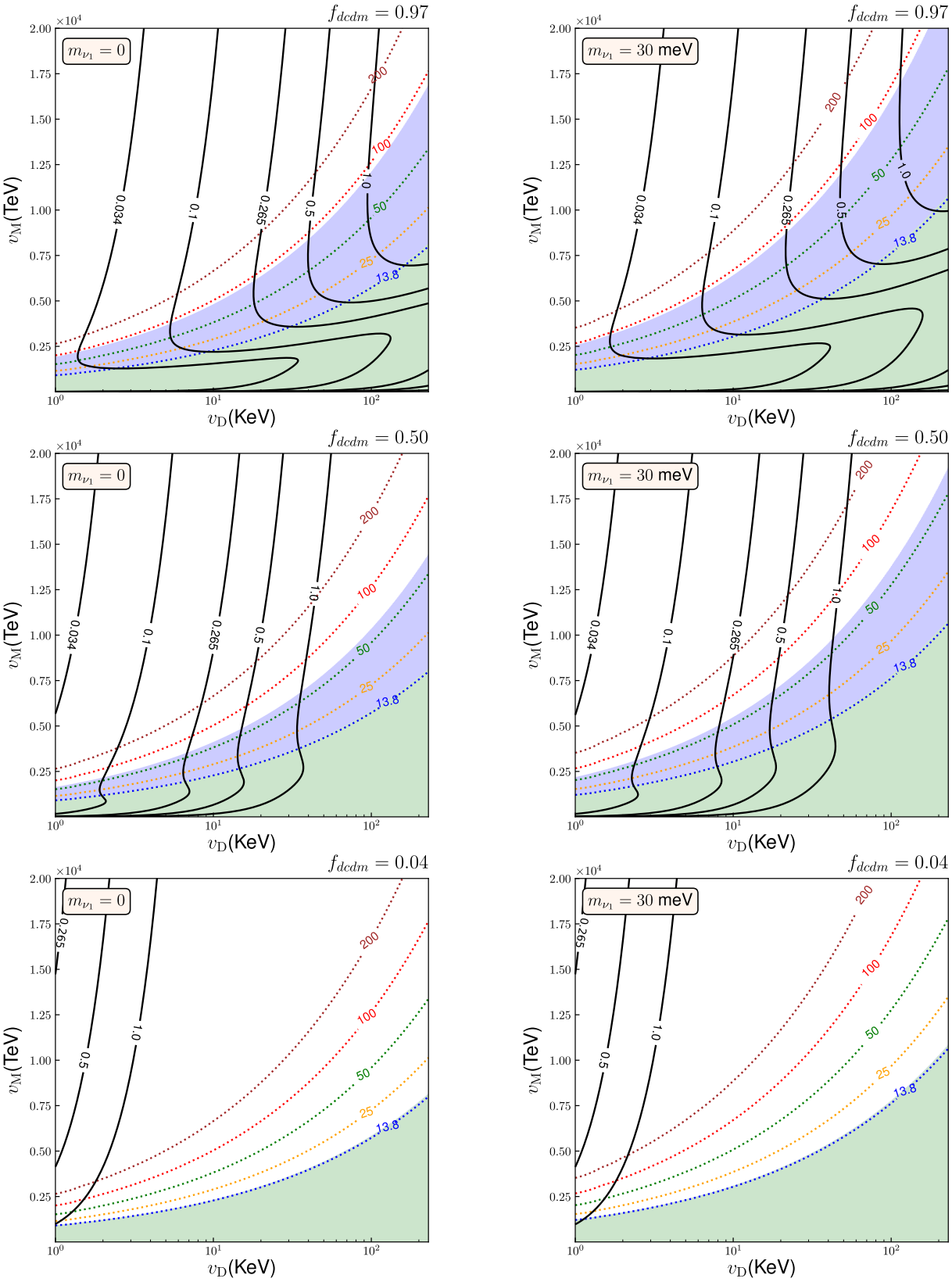

Figure 28 – Normal hierarchy: dark matter relative density (solid black) and I_3 lifetime in Gyr (dotted) curves. Blue regions are ruled-out because I_3 represents too-large of a fraction of the cold dark matter and its mean lifetime is too short, even if it is larger than the age of the Universe. Green regions are excluded as $\Gamma(I_3 \to \nu\nu) > H_0$, and $f_{\rm dcdm}$ used in these plots are larger than 0.04.

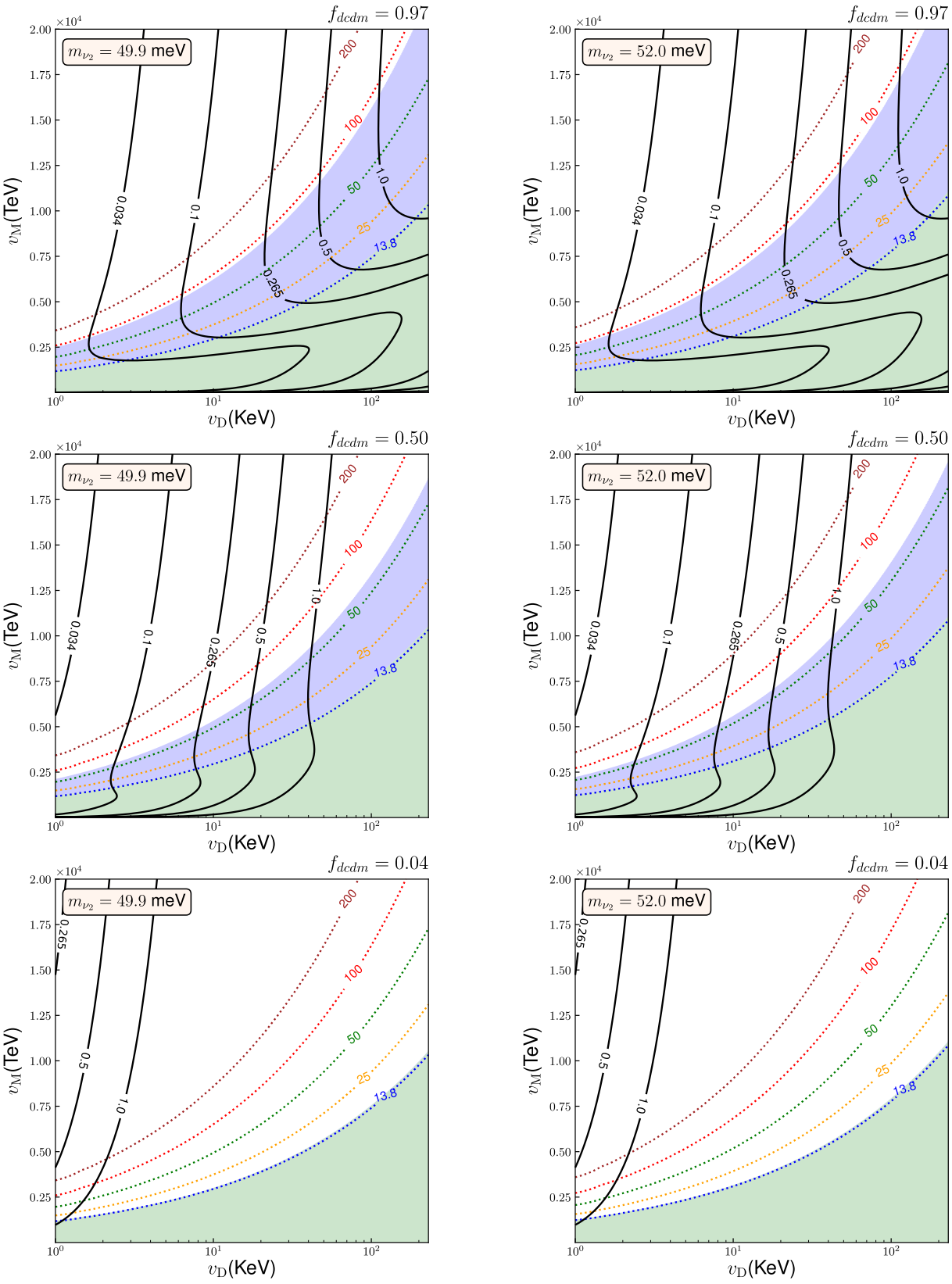

Figure 29 – Like Fig.28 for neutrino inverted hierarchy.

5 Conclusions

Despite the title of this thesis, in this work we have studied more than one dark matter candidate. In fact, we have studied models of asymmetric and decaying dark matter which could solve some of the small-scale challenges for theoretical cosmology. In particular, we solve the core-cusp problem by means of late-time reactivation of DM annihilations at the center of DM-dominated systems such as dwarf-spheroidal galaxies and galaxy clusters. We have worked two models of fermionic asymmetric dark matter with small DM-number Majorana mass terms. These allow for DM particle-antiparticle oscillations and we have derived upper bounds for them by imposing that the late-time depletion of DM density be allowed by CMB constraints.

When the DM is a heavy neutral lepton that couples to a light singlet scalar which mixes with the Higgs boson, experimental constraints that only consider HNL decays via weak interactions, must be reanalized. For this reason, we have performed a reinterpretation of three of the current limits on HNL mixing angles with active neutrinos versus HNL mass. We have found that for DELPHI and CHARM, the parameter space can open, close or remain the same, depending on the mass of the singlet scalar, its mixing angle with the Higgs boson, and the strength of its coupling to the HNLs. On the other hand, for Belle, the parameter space always opens because in this experiment the signal events include pions, which cannot be obtained from the decays of the singlet scalar. We have presented a new method to recast constraints from (older) experiments without the need to resort to computationally expensive Monte Carlo simulations.

Going beyond simple extensions of the SM, we study multi-component DM in a gauged $B - L$ model. In this theory, there is a stable component and an unstable one. Since the lifetime of a decaying DM component is strongly cosntrained when it produces dark radiation such as neutrinos or gravitational waves, we have used the most conservative limits on its decay rate as a function of the fraction of CDM it represented before decays to put constraints on the energy scales of the model. As a result, some results in previous works found in the literature are strongly disfavored, even if the present-day relative density of the unstable component is negligible.

Bibliography

[1] Fritz Zwicky. Die rotverschiebung von extragalaktischen nebeln. *Helvetica Physica Acta*, 6:110–127, 1933.

[2] Vera C. Rubin and Jr. Ford, W. Kent. Rotation of the Andromeda Nebula from a Spectroscopic Survey of Emission Regions. ApJ, 159:379, February 1970.

[3] Douglas Clowe, Maruša Bradač, Anthony H. Gonzalez, Maxim Markevitch, Scott W. Randall, Christine Jones, and Dennis Zaritsky. A direct empirical proof of the existence of dark matter. *The Astrophysical Journal Letters*, 648(2):L109, 2006. https://doi.org/10.1086/508162.

[4] T. S. Van Albada, K. Begeman, R. Sanscisi, and J. N. Bahcall. Distribution of dark matter in the spiral galaxy NGC 3198. *Dark Matter in the Universe*, 2004.

[5] Andrew Fruchter. Abell 2218: A Galaxy Cluster Lens. https://apod.nasa.gov/apod/ap011007.html.

[6] NASA/WMAP Science Team. WMAP Nine year microwave sky. https://www.nasa.gov/.

[7] Ch. Alcock, Carl W. Akerlof, R. A. Allsman, T. S. Axelrod, D. P. Bennett, S. Chan, K. H. Cook, K. C. Freeman, K. Griest, S. L. Marshall, et al. Possible gravitational microlensing of a star in the large magellanic cloud. *Nature*, 365(6447):621, 1993. https://doi.org/10.1038/365621a0.

[8] Edward W. Kolb and Michael S. Turner. *The Early Universe*, volume 69. 1990.

[9] G. Efstathiou, Richard S. Ellis, and Bruce A. Peterson. Analysis of a complete galaxy redshift survey–II. The field-galaxy luminosity function. *Monthly Notices of the Royal Astronomical Society*, 232(2):431–461, 1988.

[10] C Patrignani, Particle Data Group, et al. Review of particle physics. *Chinese physics C*, 40(10):100001, 2016.

[11] John A. Peacock. *Cosmological physics*. Cambridge university press, 1999.

[12] Peter A. R. Ade, N. Aghanim, C. Armitage-Caplan, M. Arnaud, M. Ashdown, F. Atrio-Barandela, J. Aumont, C. Baccigalupi, Anthony J. Banday, R. B. Barreiro, et al. Planck 2013 results. XVI. Cosmological parameters. *Astronomy & Astrophysics*, 571:A16, 2014.

[13] John N. Bahcall, Tsvi Piran, and Steven Weinberg. *Dark Matter in the Universe*. World Scientific, 2004.

[14] Richard S. Ellis. Gravitational lensing: a unique probe of dark matter and dark energy. *Philosophical Transactions of the Royal Society of London A: Mathematical, Physical and Engineering Sciences*, 368(1914):967–987, 2010.

[15] Giorgio Arcadi, Maíra Dutra, Pradipta Ghosh, Manfred Lindner, Yann Mambrini, Mathias Pierre, Stefano Profumo, and Farinaldo S. Queiroz. The waning of the WIMP? A review of models, searches, and constraints. *Eur. Phys. J. C*, 78(3):203, 2018. arXiv:1703.07364.

[16] James M. Cline and Guillermo Gambini. Constraints on heavy neutral leptons interacting with a singlet scalar. *Phys. Rev. D*, 105:115035, Jun 2022. arXiv:2203.08166.

[17] Takehiko Asaka and Mikhail Shaposhnikov. The νMSM, dark matter and baryon asymmetry of the universe. *Phys. Lett. B*, 620:17–26, 2005.

[18] Mikhail Shaposhnikov and Igor Tkachev. The νMSM, inflation, and dark matter. *Phys. Lett. B*, 639:414–417, 2006.

[19] Guillermo Ballesteros, Javier Redondo, Andreas Ringwald, and Carlos Tamarit. Unifying inflation with the axion, dark matter, baryogenesis and the seesaw mechanism. *Phys. Rev. Lett.*, 118(7):071802, 2017.

[20] Sandhya Choubey and Abhass Kumar. Inflation and Dark Matter in the Inert Doublet Model. *JHEP*, 11:080, 2017.

[21] Debasish Borah, P. S. Bhupal Dev, and Abhass Kumar. TeV scale leptogenesis, inflaton dark matter and neutrino mass in a scotogenic model. *Phys. Rev. D*, 99(5):055012, 2019.

[22] James M. Cline, Matteo Puel, and Takashi Toma. A little theory of everything, with heavy neutral leptons. *JHEP*, 05:039, 2020. arXiv:2010.12583.

[23] Kyrylo Bondarenko, Alexey Boyarsky, Dmitry Gorbunov, and Oleg Ruchayskiy. Phenomenology of GeV-scale Heavy Neutral Leptons. *JHEP*, 11:032, 2018. arXiv:1805.08567.

[24] P. Abreu et al. Search for neutral heavy leptons produced in Z decays. *Z. Phys. C*, 74:57–71, 1997. [Erratum: Z.Phys.C 75, 580 (1997)]. CERN-PPE-96-195.

[25] M. Dittmar, A. Santamaria, M. C. Gonzalez-Garcia, and J. W. F. Valle. Production Mechanisms and Signatures of Isosinglet Neutral Heavy Leptons in Z^0 Decays. *Nucl. Phys. B*, 332:1–19, 1990.

[26] D. Liventsev et al. Search for heavy neutrinos at Belle. *Phys. Rev. D*, 87(7):071102, 2013. [Erratum: Phys.Rev.D 95, 099903 (2017)]. arXiv:1301.1105.

[27] S. Aoki et al. FLAG Review 2019: Flavour Lattice Averaging Group (FLAG). *Eur. Phys. J. C*, 80(2):113, 2020. arXiv:1902.08191.

[28] Jordy De Vries, Herbert K. Dreiner, Julian Y. Günther, Zeren Simon Wang, and Guanghui Zhou. Long-lived Sterile Neutrinos at the LHC in Effective Field Theory. *JHEP*, 03:148, 2021.

[29] J. Dorenbosch et al. A search for decays of heavy neutrinos in the mass range 0.5 - 2.8 GeV. *Phys. Lett. B*, 166:473–478. 15 p, Nov 1985. CERN-EP-85-190.

[30] Michael Gronau, Chung Ngoc Leung, and Jonathan L. Rosner. Extending Limits on Neutral Heavy Leptons. *Phys. Rev. D*, 29:2539, 1984.

[31] Iryna Boiarska, Alexey Boyarsky, Oleksii Mikulenko, and Maksym Ovchynnikov. Constraints from the CHARM experiment on heavy neutral leptons with tau mixing. *Phys. Rev. D*, 104(9):095019, 2021. arXiv:2107.14685.

[32] Elena Graverini, Eric Van Herwijnen, and Thomas Ruf. Mass dependence of branching ratios into HNL for FairShip. Feb 2016. CERN-SHiP-NOTE-2016-001.

[33] C. Ahdida et al. Sensitivity of the SHiP experiment to Heavy Neutral Leptons. *JHEP*, 04:077, 2019. arXiv:1811.00930.

[34] Dmitry Gorbunov and Mikhail Shaposhnikov. How to find neutral leptons of the νMSM? *JHEP*, 10:015, 2007. [Erratum: JHEP 11, 101 (2013)]. arXiv:0705.1729.

[35] H. Dijkstra and T. Ruf. Heavy Flavour Cascade Production in a Beam Dump. Dec 2015. CERN-SHiP-NOTE-2015-009.

[36] Anthony Fradette and Maxim Pospelov. BBN for the LHC: constraints on lifetimes of the Higgs portal scalars. *Phys. Rev. D*, 96(7):075033, 2017. arXiv:1706.01920.

[37] Martin Wolfgang Winkler. Decay and detection of a light scalar boson mixing with the Higgs boson. *Phys. Rev. D*, 99(1):015018, 2019. arXiv:2010.12583.

[38] M Acciarri et al. Search for neutral Higgs boson production through the process $e^+e^- \to Z^*H^0$. *Physics Letters B*, 385(1-4):454–470, 1996.

[39] S Chatrchyan et al. Search for a light pseudoscalar Higgs boson in the dimuon decay channel in pp collisions at $\sqrt{s}$= 7 TeV. *Phys. Rev. Lett.*, 109:121801, 2012.

[40] Roel Aaij et al. Search for a dimuon resonance in the Υ mass region. *JHEP*, 09:147, 2018. arXiv:1805.09820.

[41] A. V. Artamonov et al. Study of the decay $K^+ \to \pi^+\nu\bar{\nu}$ in the momentum region $140 < P_\pi < 199$ MeV/c. *Phys. Rev. D*, 79:092004, 2009.

[42] J. P. Lees et al. Search for hadronic decays of a light higgs boson in the radiative decay $\Upsilon \to \gamma A^0$. *Phys. Rev. Lett.*, 107:221803, Nov 2011.

[43] J. P. Lees et al. Search for a low-mass scalar higgs boson decaying to a tau pair in single-photon decays of $\Upsilon(1s)$. *Phys. Rev. D*, 88:071102, Oct 2013.

[44] J. P. Lees et al. Search for long-lived particles in e^+e^- collisions. *Phys. Rev. Lett.*, 114:171801, Apr 2015.

[45] A. Alavi-Harati et al. Search for the decay $K_L \to \pi^0\mu^+\mu^-$. *Phys. Rev. Lett.*, 84:5279–5282, Jun 2000.

[46] James M. Cline, Guillermo Gambini, Samuel D. Mcdermott, and Matteo Puel. Late-Time Dark Matter Oscillations and the Core-Cusp Problem. *JHEP*, 04:223, 2021. arXiv:2010.12583.

[47] John Dubinski and R. G. Carlberg. The Structure of cold dark matter halos. *Astrophys. J.*, 378:496, 1991.

[48] Ricardo A Flores and Joel R Primack. Observational and theoretical constraints on singular dark matter halos. *arXiv preprint astro-ph/9402004*, 1994. arXiv:9402004.

[49] Sean Tulin and Hai-Bo Yu. Dark Matter Self-interactions and Small Scale Structure. *Phys. Rept.*, 730:1–57, 2018. arXiv:1705.02358.

[50] Kathryn M. Zurek. Asymmetric Dark Matter: Theories, Signatures, and Constraints. *Phys. Rept.*, 537:91–121, 2014. arXiv:1308.0338.

[51] Timothy Cohen and Kathryn M. Zurek. Leptophilic Dark Matter from the Lepton Asymmetry. *Phys. Rev. Lett.*, 104:101301, 2010. arXiv:0909.2035.

[52] Yi Cai, David E Kaplan, and Markus A Luty. Leptonic indirect detection signals from strongly interacting asymmetric dark matter. *arXiv preprint arXiv:0909.5499*, 2009.

[53] Chiara Arina and Narendra Sahu. Asymmetric inelastic inert doublet dark matter from triplet scalar leptogenesis. *Nuclear Physics B*, 854(3):666–699, 2012.

[54] Adam Falkowski, Joshua T Ruderman, and Tomer Volansky. Asymmetric dark matter from leptogenesis. *Journal of High Energy Physics*, 2011(5):1–32, 2011.

[55] Kfir Blum, Aielet Efrati, Yuval Grossman, Yosef Nir, and Antonio Riotto. Asymmetric higgsino dark matter. *Physical review letters*, 109(5):051302, 2012.

[56] Marco Cirelli, Paolo Panci, Geraldine Servant, and Gabrijela Zaharijas. Consequences of DM/antiDM Oscillations for Asymmetric WIMP Dark Matter. *JCAP*, 03:015, 2012. arXiv:1110.3809.

[57] Matthew R Buckley and Stefano Profumo. Regenerating a symmetry in asymmetric dark matter. *Physical review letters*, 108(1):011301, 2012.

[58] Sean Tulin, Hai-Bo Yu, and Kathryn M. Zurek. Oscillating Asymmetric Dark Matter. *JCAP*, 05:013, 2012. arXiv:1202.0283.

[59] Paolo Gondolo and Graciela Gelmini. Cosmic abundances of stable particles: Improved analysis. *Nuclear Physics B*, 360(1):145–179, 1991. https://doi.org/10.1016/0550-3213(91)90438-4.

[60] Julio F. Navarro, Carlos S. Frenk, and Simon D. M. White. A universal density profile from hierarchical clustering. *The Astrophysical Journal*, 490(2):493, 1997. arXiv:9611107.

[61] Ewa L. Lokas and Gary A. Mamon. Properties of spherical galaxies and clusters with an NFW density profile. *Mon. Not. Roy. Astron. Soc.*, 321:155, 2001.

[62] Vivian Poulin, Pasquale D. Serpico, and Julien Lesgourgues. A fresh look at linear cosmological constraints on a decaying dark matter component. *JCAP*, 08:036, 2016.

[63] Andrew B. Newman, Tommaso Treu, Richard S. Ellis, David J. Sand, Carlo Nipoti, Johan Richard, and Eric Jullo. The Density Profiles of Massive, Relaxed Galaxy Clusters: I. The Total Density Over 3 Decades in Radius. *Astrophys. J.*, 765:24, 2013.

[64] Ayuki Kamada, Manoj Kaplinghat, Andrew B. Pace, and Hai-Bo Yu. How the Self-Interacting Dark Matter Model Explains the Diverse Galactic Rotation Curves. *Phys. Rev. Lett.*, 119(11):111102, 2017.

[65] Se-Heon Oh et al. High-resolution mass models of dwarf galaxies from LITTLE THINGS. *Astron. J.*, 149:180, 2015.

[66] Manoj Kaplinghat, Sean Tulin, and Hai-Bo Yu. Dark Matter Halos as Particle Colliders: Unified Solution to Small-Scale Structure Puzzles from Dwarfs to Clusters. *Phys. Rev. Lett.*, 116(4):041302, 2016. arXiv:1508.03339.

[67] Andrew B. Newman, Tommaso Treu, Richard S. Ellis, and David J. Sand. The density profiles of massive, relaxed galaxy clusters. ii. separating luminous and dark matter in cluster cores. *Astrophys. J.*, 765:25, 2013.

[68] Manoj Kaplinghat, Lloyd Knox, and Michael S. Turner. Annihilating the cold dark matter cusp crisis. *Phys. Rev. Lett.*, 85:3335, 2000.

[69] Guillermo Gambini, Pedro C. de Holanda, and Saulo Carneiro. Constraints on energy scales from dark matter decay in a gauged $B - L$ model. 5 2022. arXiv:2205.12353.

[70] Samuel D. McDermott. Is Self-Interacting Dark Matter Undergoing Dark Fusion? *Phys. Rev. Lett.*, 120(22):221806, 2018. arXiv:1711.00857.

[71] Manfred Lindner, Yann Mambrini, Téssio B. de Melo, and Farinaldo S. Queiroz. XENON1T anomaly: A light Z' from a Two Higgs Doublet Model. *Phys. Lett. B*, 811:135972, 2020. arXiv:2006.14590.

[72] Shao-Feng Ge, Xiao-Dong Ma, and Pedro Pasquini. Probing the dark axion portal with muon anomalous magnetic moment. *Eur. Phys. J. C*, 81(9):787, 2021. arXiv:2104.03276.

[73] Shao-Feng Ge, Pedro Pasquini, and Jie Sheng. Solar Active-Sterile Neutrino Conversion with Atomic Effects at Dark Matter Direct Detection Experiments. 12 2021. arXiv:2112.05560.

[74] James M. Cline, Christian Gross, and Wei Xue. Can the ANITA anomalous events be due to new physics? *Phys. Rev. D*, 100(1):015031, 2019. arXiv:1904.13396.

[75] Nikita Blinov, Kevin J. Kelly, Gordan Krnjaic, and Samuel D. McDermott. Constraining the Self-Interacting Neutrino Interpretation of the Hubble Tension. *Phys. Rev. Lett.*, 123:191102, Nov 2019. arXiv:1905.02727.

[76] Jailson Alcaniz, Nicolás Bernal, Antonio Masiero, and Farinaldo S. Queiroz. Light dark matter: A common solution to the lithium and H_0 problems. *Phys. Lett. B*, 812:136008, 2021. arXiv:1912.05563.

[77] Guillermo Franco Abellán, Riccardo Murgia, Vivian Poulin, and Julien Lavalle. Implications of the S_8 tension for decaying dark matter with warm decay products. *Phys. Rev. D*, 105(6):063525, 2022. arXiv:2008.09615.

[78] Miguel Escudero and Samuel J. Witte. The Hubble tension as a hint of leptogenesis and neutrino mass generation. *Eur. Phys. J. C*, 81(6):515, 2021. arXiv:2103.03249.

[79] Adam G. Riess, Lucas Macri, Stefano Casertano, Hubert Lampeitl, Henry C. Ferguson, Alexei V. Filippenko, Saurabh W. Jha, Weidong Li, and Ryan Chornock. A 3% Solution: Determination of the Hubble Constant with the Hubble Space Telescope and Wide Field Camera 3. *Astrophys. J.*, 730:119, 2011. [Erratum: Astrophys.J. 732, 129 (2011)]. arXiv:1103.2976.

[80] Catherine Heymans et al. CFHTLenS tomographic weak lensing cosmological parameter constraints: Mitigating the impact of intrinsic galaxy alignments. *Mon. Not. Roy. Astron. Soc.*, 432:2433, 2013. arXiv:1303.1808.

[81] P. A. R. Ade et al. Planck 2015 results. XXIV. Cosmology from Sunyaev-Zeldovich cluster counts. *Astron. Astrophys.*, 594:A24, 2016. arXiv:1502.01597.

[82] Adam G. Riess et al. A 2.4% Determination of the Local Value of the Hubble Constant. *Astrophys. J.*, 826(1):56, 2016. arXiv:1604.01424.

[83] S. Carneiro, P. C. de Holanda, C. Pigozzo, and F. Sobreira. Is the H_0 tension suggesting a fourth neutrino generation? *Phys. Rev. D*, 100(2):023505, 2019. arXiv:1812.06064.

[84] Savvas Nesseris, Domenico Sapone, and Spyros Sypsas. Evaporating primordial black holes as varying dark energy. *Phys. Dark Univ.*, 27:100413, 2020. arXiv:1907.05608.

[85] Kari Enqvist, Seshadri Nadathur, Toyokazu Sekiguchi, and Tomo Takahashi. Decaying dark matter and the tension in σ_8. *JCAP*, 09:067, 2015. arXiv:1505.05511.

[86] Nikita Blinov, Celeste Keith, and Dan Hooper. Warm Decaying Dark Matter and the Hubble Tension. *JCAP*, 06:005, 2020. arXiv:2004.06114.

[87] Evgeny K. Akhmedov, Zurab G. Berezhiani, Goran Senjanovic, and Zhi-jian Tao. Planck scale effects in neutrino physics. *Phys. Rev. D*, 47:3245–3253, 1993. arXiv:9208230.

[88] Y. Chikashige, Rabindra N. Mohapatra, and R. D. Peccei. Are There Real Goldstone Bosons Associated with Broken Lepton Number? *Phys. Lett. B*, 98:265–268, 1981.

[89] Davi B. Costa, Bogdan A. Dobrescu, and Patrick J. Fox. General Solution to the U(1) Anomaly Equations. *Phys. Rev. Lett.*, 123(15):151601, 2019. arXiv:1905.13729.

[90] J. C. Montero and V. Pleitez. Gauging U (1) symmetries and the number of right-handed neutrinos. *Physics Letters B*, 675(1):64–68, 2009. arXiv:2010.12583.

[91] B. L. Sánchez-Vega, J. C. Montero, and E. R. Schmitz. Complex scalar dark matter in a B-L model. *Physical Review D*, 90(5):055022, 2014. arXiv:2010.12583.

[92] Peter Lancaster and Miron Tismenetsky. *The theory of matrices: with applications*. Elsevier, 1985.

[93] Brian J McCartin. *Rayleigh-Schrödinger perturbation theory: Pseudoinverse formulation*. Hikari Limited Bulgaria, 2009.

[94] C. E. Alvarez-Salazar and O. L. G. Peres. Constraining the $3-3-1$ model with heavy neutral leptons using $(g-2)_\mu$ and dark matter observables. *Phys. Rev. D*, 103(3):035029, 2021. arXiv:1906.06444.

[95] J Schechter and José WF Valle. Neutrino decay and spontaneous violation of lepton number. *Physical Review D*, 25(3):774, 1982.

[96] Massimiliano Lattanzi and José W. F. Valle. Decaying warm dark matter and neutrino masses. *Phys. Rev. Lett.*, 99(12):121301, 2007. arXiv:0705.2406.

[97] N. Aghanim et al. Planck 2018 results. VI. Cosmological parameters. *Astron. Astrophys.*, 641:A6, 2020. [Erratum: Astron.Astrophys. 652, C4 (2021)]. arXiv:1807.06209.

[98] Benjamin Audren, Julien Lesgourgues, Gianpiero Mangano, Pasquale Dario Serpico, and Thomas Tram. Strongest model-independent bound on the lifetime of Dark Matter. *JCAP*, 12:028, 2014. arXiv:1407.2418.

[99] Ivan Esteban, Maria Conceptión González-García, Michele Maltoni, Thomas Schwetz, and Albert Zhou. The fate of hints: updated global analysis of three-flavor neutrino oscillations. *Journal of High Energy Physics*, 2020(9):1–22, 2020. arXiv:2007.14792.

[100] Particle Data Group. Review of Particle Physics. *Progress of Theoretical and Experimental Physics*, 2020(8), 08 2020. 083C01.

[101] Torsten Bringmann, Felix Kahlhoefer, Kai Schmidt-Hoberg, and Parampreet Walia. Converting nonrelativistic dark matter to radiation. *Phys. Rev. D*, 98(2):023543, 2018.

APPENDIX A – Self-interacting term for the vector model

The content of this chapter is heavily based on Ref. [46], where our main results are published.

In this appendix we derive the collision term for elastic scattering of $\chi\chi$ or $\chi\bar{\chi}$ through exchange of the vector boson V^μ, needed for the quantum Boltzmann equations.

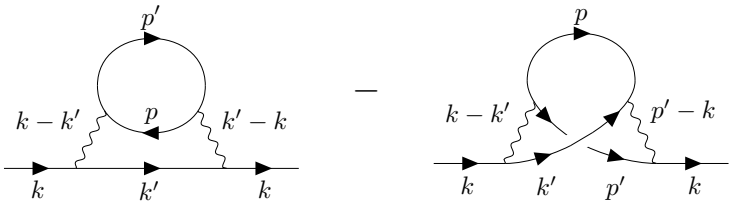

Figure 30 – Self-energy diagrams for the vector model (model 1).

We can read off the imaginary part of the self-energies $\Sigma^{>,<}$, in analogy to their Eq. (A26) of ref. [58],

$$\begin{aligned}\Sigma^{>,<}(k) &= i\frac{g'^4}{4}\int dk'dp'dp\,(2\pi)^4\delta^{(4)}(k+p-k'-p') \\ &\cdot \left[\frac{1}{((k-k')^2-m_V^2)^2}\,O_-\gamma^\mu S^{>,<}_{k'}O_-\gamma^\nu\,\mathrm{Tr}\left(S^{<,>}_{p}O_-\gamma_\mu S^{>,<}_{p'}O_-\gamma_\nu\right)\right. \\ &- \left.\frac{1}{((k-k')^2-m_V^2)((p-p')^2-m_V^2)}\,O_-\gamma^\mu S^{>,<}_{p'}O_-\gamma^\nu S^{<,>}_{p}O_-\gamma_\mu S^{>,<}_{k'}O_-\gamma_\nu\right],\end{aligned} \tag{A.1}$$

where $dp = \frac{d^4p}{(2\pi)^4}$ and the Green's functions are given by

$$\begin{aligned}S^<_k &= -2\pi\delta(k^2-m^2)(\not{k}+m_\chi)\left[\theta_{k^0}\mathcal{F}_k-\theta_{-k^0}(1-\bar{\mathcal{F}}_k)\right], \\ S^>_k &= +2\pi\delta(k^2-m^2)(\not{k}+m_\chi)\left[\theta_{k^0}(1-\mathcal{F}_k)-\theta_{-k^0}\bar{\mathcal{F}}_k\right].\end{aligned} \tag{A.2}$$

Here $\bar{\mathcal{F}}$ is the matrix with the diagonal entries interchanged, as in Eq.(11) of [58], and O_-) is Pauli σ_3 matrix. The trace is over both Dirac and flavor indices. We also define

$$\tilde{\mathcal{F}} = O_-\mathcal{F}O_-\,, \quad \text{and} \quad \tilde{\bar{\mathcal{F}}} = O_-\bar{\mathcal{F}}O_-\,. \tag{A.3}$$

This has the effect of reversing the signs of the off-diagonal elements.

Considering the relevant physical processes, it is not necessary to take account of all eight of the terms that arise from each diagram from the products of the $S^{>,<}$ functions. First, since annihilation diagrams are suppressed while $k^0 > 0$, we can ignore $k'^0 < 0$, which would give the s-channel diagram. Second, by energy conservation, we must have either

$$\begin{aligned} &p^0 > 0 \text{ and } p'^0 > 0 \quad , \quad \text{representing } \chi\chi \text{ scattering, or} \\ &p^0 < 0 \text{ and } p'^0 < 0 \quad , \quad \text{representing } \chi\bar{\chi} \text{ scattering.} \end{aligned}$$

Let us first write the terms that arise from the middle line of (A.1), apart from the factors of $2\pi\delta(\dots)$, *i.e.*

$$\begin{aligned} \frac{1}{((k-k')^2 - m_V^2)^2} \qquad & \gamma^\mu(\not{k}' + m_\chi)\gamma^\nu \,\mathrm{Tr}\left((\not{p} + m_\chi)\gamma_\mu(\not{p}' + m_\chi)\gamma_\nu\right) \times \\ \Sigma_k^> : \qquad & (1-\tilde{\mathcal{F}}_{k'})\left[\theta_{p^0}\theta_{p'^0}\,\mathrm{Tr}\left((-\mathcal{F}_p)(1-\tilde{\mathcal{F}}_{p'})\right) + \theta_{-p^0}\theta_{-p'^0}\,\mathrm{Tr}\left((1-\bar{\mathcal{F}}_p)(-\tilde{\bar{\mathcal{F}}}_{p'})\right)\right] , \\ \Sigma_k^< : \qquad & -\tilde{\mathcal{F}}_{k'}\left[\theta_{p^0}\theta_{p'^0}\,\mathrm{Tr}\left((1-\mathcal{F}_p)(-\tilde{\mathcal{F}}_{p'})\right) + \theta_{-p^0}\theta_{-p'^0}\,\mathrm{Tr}\left((-\bar{\mathcal{F}}_p)(1-\tilde{\bar{\mathcal{F}}}_{p'})\right)\right] . \end{aligned} \tag{A.4}$$

Similarly, the last line of (A.1) contributes

$$\begin{aligned} -\frac{1}{((k-k')^2 - m_V^2)((p-p')^2 - m_V^2)} \qquad & \gamma^\mu(\not{p}' + m_\chi)\gamma^\nu(\not{p} + m_\chi)\gamma_\mu(\not{k}' + m_\chi)\gamma_\nu \times \\ \Sigma_k^> : \qquad & (1-\tilde{\mathcal{F}}_{p'})\Big[\theta_{p^0}\theta_{p'^0}\left((-\mathcal{F}_p)(1-\tilde{\mathcal{F}}_{k'})\right) \\ & \qquad +\theta_{-p^0}\theta_{-p'^0}\left((1-\bar{\mathcal{F}}_p)(-\tilde{\bar{\mathcal{F}}}_{k'})\right)\Big] , \\ \Sigma_k^< : \qquad & -\tilde{\mathcal{F}}_{p'}\Big[\theta_{p^0}\theta_{p'^0}\left((1-\mathcal{F}_p)(-\tilde{\mathcal{F}}_{k'})\right) \\ & \qquad +\theta_{-p^0}\theta_{-p'^0}\left((-\bar{\mathcal{F}}_p)(1-\tilde{\bar{\mathcal{F}}}_{k'})\right)\Big] . \end{aligned} \tag{A.5}$$

Now, the collision term comes from $\Sigma^{>,<}$ by

$$\mathcal{C}_s = i\int \frac{d^4k}{(2\pi)^4}\,\mathrm{tr}\left[\left(\frac{\not{k} + m_\chi}{4m_\chi}\right)\left(\{\Sigma_k^<, S_k^>\} - \{\Sigma_k^>, S_k^<\}\right)\right] , \tag{A.6}$$

where, unlike Tr above, tr denotes only the trace over Dirac matrices. Since we are interested in low densities, we can neglect terms of order $\mathcal{F}^3$, which means that we need only keep terms of order

$$\Sigma_k^< : O(\mathcal{F}^2) , \quad S_k^> : O(1) , \quad \Sigma_k^> : O(\mathcal{F}) , \quad S_k^< : O(\mathcal{F}) . \tag{A.7}$$

After carrying out the Dirac traces and combining like terms, we find the respective contributions from the two diagrams are

$$\begin{aligned}
\mathcal{C}_1 &= -4g'^4 \int d\Pi_k d\Pi_{k'} d\Pi_p d\Pi_{p'} \, \frac{(2\pi)^4 \delta^{(4)}(k+p-k'-p')}{((k-k')^2 - m_V^2)^2} \\
&\times \left[(k\cdot p)(k'\cdot p') + (k\cdot p')(k'\cdot p) - m_\chi^2 (k\cdot k' + p\cdot p') + 2m_\chi^4\right] \\
&\times \theta_{k^0}\theta_{k'^0}\Big\{\theta_{p^0}\theta_{p'^0}\Big[\tilde{\mathcal{F}}_{k'} \operatorname{Tr}\tilde{\mathcal{F}}_{p'} - \mathcal{F}_k \operatorname{Tr}\mathcal{F}_p\Big] + \theta_{-p^0}\theta_{-p'^0}\Big[\tilde{\mathcal{F}}_{k'} \operatorname{Tr}\bar{\mathcal{F}}_p - \mathcal{F}_k \operatorname{Tr}\bar{\tilde{\mathcal{F}}}_{p'}\Big]\Big\}, \\
\mathcal{C}_2 &= -4g'^4 \int d\Pi_k d\Pi_{k'} d\Pi_p d\Pi_{p'} \, \frac{(2\pi)^4 \delta^{(4)}(k+p-k'-p')}{((k-k')^2 - m_V^2)((p-p')^2 - m_V^2)} \\
&\times \left[(k\cdot p)(k'\cdot p') - \tfrac{1}{2}m_\chi^2 (k\cdot k' + p\cdot p' + k\cdot p + k\cdot p' + k'\cdot p + k'\cdot p') + m_\chi^4\right] \\
&\times \theta_{k^0}\theta_{k'^0}\Big\{\theta_{p^0}\theta_{p'^0}\Big[\tilde{\mathcal{F}}_{p'}\tilde{\mathcal{F}}_{k'} - \tfrac{1}{2}\{\mathcal{F}_p, \mathcal{F}_k\}\Big] + \theta_{-p^0}\theta_{-p'^0}\Big[\tilde{\mathcal{F}}_{p'}\bar{\mathcal{F}}_p - \tfrac{1}{2}\{\bar{\tilde{\mathcal{F}}}_{k'}, \mathcal{F}_k\}\Big]\Big\}, \quad \text{(A.8)}
\end{aligned}$$

where $d\Pi_p = d^4p\,\delta(p^2 - m_\chi^2)/(2\pi)^3$.

In the non-relativistic limit, it further simplifies since the squared matrix element in brackets is equal to $2m_\chi^4$ for $\mathcal{C}_1$, while for $\mathcal{C}_2$ it depends on which of the theta functions are taken, *i.e.* $[\ldots] = -m_\chi^4$ for positive energies and $+m_\chi^4$ for negative energies. The resulting collision term is

$$\begin{aligned}
\mathcal{C}_s &= -\frac{g'^4}{4(2\pi)^8 m_V^4} \int d^3k \cdots d^3p'\, \delta^{(4)}(\cdots) \Big[4\Big(\tilde{\mathcal{F}}_{k'} \operatorname{Tr}\mathcal{F}_{p'} - \mathcal{F}_k \operatorname{Tr}\mathcal{F}_p\Big) \\
&- \tilde{\mathcal{F}}_{p'}\tilde{\mathcal{F}}_{k'} + \tfrac{1}{2}\{\mathcal{F}_p, \mathcal{F}_k\} + \tilde{\mathcal{F}}_p\bar{\mathcal{F}}_{p'} - \tfrac{1}{2}\{\bar{\tilde{\mathcal{F}}}_{k'}, \mathcal{F}_k\}\Big]. \quad \text{(A.9)}
\end{aligned}$$

Here, we used the identities $\operatorname{Tr}\tilde{\mathcal{F}}_p = \operatorname{Tr}\bar{\mathcal{F}}_p = \operatorname{Tr}\bar{\tilde{\mathcal{F}}}_p = \operatorname{Tr}\mathcal{F}_p$, as well as the fact that any terms with negative energies can be transformed to the corresponding phase space integrals with positive energy by changing $p \leftrightarrow p'$.

The next step is to make the following ansatz

$$\mathcal{F}_k = e^{-\beta\omega_k}\frac{n}{n_{\text{eq}}}, \quad \text{(A.10)}$$

where $\omega_k \cong m_\chi + k^2/2m_\chi \equiv m_\chi + E_k$,

$$n = \begin{pmatrix} n_{11} & n_{12} \\ n_{21} & n_{22} \end{pmatrix}, \quad \text{(A.11)}$$

and n_{eq} is the equilibrium number density. Then, the momentum integrals can be carried out to get collision terms as a function of the density matrix n

$$\begin{aligned}
\mathcal{C}_s &= -\frac{g'^4\, e^{-2\beta m_\chi}}{4(2\pi)^8 m_V^4\, n_{\text{eq}}^2} \int d^3k \cdots d^3p'\, \delta^{(4)}(\cdots) \Big[e^{-\beta(E_k+E_p)}\left[4(\tilde{n}-n)\operatorname{Tr} n - \tilde{n}^2 + n^2\right] \\
&+ e^{-\beta(E_p+E_{p'})}\tilde{n}\bar{n} - e^{-\beta(E_k+E_{k'})}\tfrac{1}{2}\{\tilde{\bar{n}}, n\}\Big]. \quad \text{(A.12)}
\end{aligned}$$

The integrals are all equal to $(m_\chi T)^{9/2}/T$ times a dimensionless number and there are only two different possibilities, depending upon whether the two energies in the Boltzmann factors are both initial/final state or one initial and one final. We get

$$\mathcal{C}_s = -\frac{g'^4\, m_\chi^{3/2} T^{1/2}}{16\pi\, m_V^4}\Big[I_s\,\left(4(\tilde{n}-n)\,\mathrm{Tr}\,n-\tilde{n}^2+n^2\right)+I_d\,\left(\tilde{n}\bar{n}-\tfrac{1}{2}\{\bar{\tilde{n}},n\}\right)\Big]\,, \quad \text{(A.13)}$$

where the two dimensionless integrals I_s and I_d are

$$\begin{aligned} I_s &= \frac{1}{8\pi^4}\int d^3p\, d^3k\, d^3p'\, d^3k'\, \delta^{(4)}(p+k-p'-k')\, e^{-(p^2+k^2)/2} \\ &= \frac{1}{8\pi^4}\int d^3p\, d^3k\, d^3p'\, \delta(\vec{p}\cdot\vec{k})\, e^{-(\vec{p}+\vec{p}')^2/2-(\vec{k}+\vec{p}')^2/2} \cong 2.26\,, \\ I_d &= \frac{1}{8\pi^4}\int d^3p\, d^3k\, d^3p'\, d^3k'\, \delta^{(4)}(p+k-p'-k')\, e^{-(p^2+p'^2)/2} \\ &= \frac{1}{8\pi^4}\int d^3p\, d^3k\, d^3p'\, \delta(\vec{p}\cdot\vec{k})\, e^{-(\vec{p}+\vec{p}')^2/2-p'^2/2} = \infty\,, \end{aligned} \quad \text{(A.14)}$$

and the zeroth component of the delta function is in terms of the non-relativistic dimensionless energies. The second forms of the integrals, in which the delta function of energies simplifies, are obtained by shifting $\vec{p}\to\vec{p}+\vec{p}'$ and $\vec{k}\to\vec{k}+\vec{p}'$. I_s was evaluated numerically. The divergent integral is inconsequential because it multiplies $\tilde{n}\bar{n}-\frac{1}{2}\{\bar{\tilde{n}},n\}\equiv 0$, which vanishes identically. In retrospect, we understand that this term is unphysical, since it corresponds to the interference of the t- and u-channel scattering diagrams, which vanishes for scattering of χ with $\bar{\chi}$. Finally, the relevant matrix evaluates to

$$4(\tilde{n}-n)\,\mathrm{Tr}\,n-\tilde{n}^2+n^2 = -6(n_{11}+n_{22})\begin{pmatrix} 0 & n_{12} \\ n_{21} & 0\end{pmatrix}\,, \quad \text{(A.15)}$$

so the collision term from scattering reads

$$\mathcal{C}_s = \frac{3I_s g'^4\, m_\chi^{3/2} T^{1/2}}{8\pi m_V^4}\,(n_{11}+n_{22})\begin{pmatrix} 0 & n_{12} \\ n_{21} & 0\end{pmatrix} \equiv \tfrac{3}{2}\langle\sigma v\rangle_s (n_{11}+n_{22})\begin{pmatrix} 0 & n_{12} \\ n_{21} & 0\end{pmatrix}\,, \quad \text{(A.16)}$$

which would appear in Eq. (20) of ref. [58]. The normalization of $\langle\sigma v\rangle_s$ is chosen to agree with the usual definition in which the low-energy cross section is

$$\sigma \approx \frac{g^4 m_\chi^2}{4\pi m_v^4}, \quad \text{(A.17)}$$

and the thermal averaging is done as in ref. [59].

APPENDIX B – Thermal decoherence in the Boltzmann equations

The content of this chapter is heavily based on Ref. [46], where our main results are published.

For the vector model (model 1), we have simulated the effect of thermal decoherence due to the oscillation rate depending on the momentum in the quantum Boltzmann equation for the density matrix

$$\frac{d\mathcal{F}_k}{dt} - Hk\frac{d\mathcal{F}_k}{dk} = -i[\mathcal{H}_k, \mathcal{F}] + \mathcal{C}[\mathcal{F}], \qquad \mathcal{H}_k = \omega_k \mathbb{1} + \frac{m_\chi \delta m}{\omega_k}\begin{pmatrix} 0 & 1 \\ 1 & 0 \end{pmatrix}, \tag{B.1}$$

where H is the Hubble rate and $\omega_k = \sqrt{k^2 + m_\chi^2}$. The k-dependence in the second term of the Hamiltonian implies that high-k parts of the distribution oscillate with slightly lower frequency than low-k parts. This is an additional source of decoherence that is neglected by integrating over momenta to reduce Eq. (B.1) to an equation for the number density matrix n. Our goal here is to verify that this neglect is justified. For the scalar model (model 2), this issue is less important since decoherence is not a requirement for annihilations to occur, as the interaction here is flavor-blind.

To model the effect, one would like to divide the particle distribution into several momentum bins. We will be content to divide them into just two, labeled by s, l for small and large momenta relative to the midpoint of the distribution. Accordingly, we split the density matrix n into

$$n = n_s + n_l, \tag{B.2}$$

and one finds separate Boltzmann equations for each component. These are coupled to each other through the collision terms. The Boltzmann equations take the form

$$\begin{aligned} \dot{n}_s + 3Hn_s &= -i[H_s, n_s] - \frac{\langle\sigma v\rangle_s}{8}(S_s + S) - \frac{\langle\sigma v\rangle_a}{2}\left(A_s - n_{\rm eq}^2\right), \\ \dot{n}_l + 3Hn_l &= -i[H_l, n_l] - \frac{\langle\sigma v\rangle_s}{8}(S_l + S) - \frac{\langle\sigma v\rangle_a}{2}\left(A_l - n_{\rm eq}^2\right), \end{aligned} \tag{B.3}$$

where $\langle\sigma v\rangle_{s,a}$ are the scattering and annihilation cross sections. The matrices S_i, S, A_i

are defined as

$$S_i = \begin{pmatrix} n_{i,11}(6n_{11}+8n_{22}) - n_{i,12}n_{21} - n_{i,21}n_{12} & 7n_{i,12}n - n_{i,t}n_{12} \\ 7n_{i,21}n_t - n_i n_{21} & n_{i,22}(8n_{11}+6n_{22}) - n_{i,12}n_{21} - n_{i,21}n_{12} \end{pmatrix}, \tag{B.4}$$

$$S = \begin{pmatrix} -3n_{11}^2 - 4n_{11}n_{22} + n_{12}n_{21} & 3n_{12}n \\ 3n_{21}n & -3n_{22}^2 - 4n_{11}n_{22} + n_{12}n_{21} \end{pmatrix}, \tag{B.5}$$

$$A_i = \begin{pmatrix} 2\,n_{i,11}n_{22} - (n_{i,12}n_{21} + n_{i,21}n_{12}) & (n_{i,12}n_t - n_i n_{12}) \\ (n_{i,21}n - n_i n_{21}) & 2\,n_{i,22}n_{11} - (n_{i,12}n_{21} + n_{i,21}n_{12}) \end{pmatrix}, \tag{B.6}$$

and we defined $n_{ij} = n_{s,ij} + n_{l,ij}$, $n = n_{11} + n_{22}$, and $n_i = n_{i,11} + n_{i,22}$. These expressions can be read from the form of the collision and annihilation terms in terms of the $\mathcal{F}$ matrices before doing the final integral over the momentum k of the particle whose distribution is being tracked in the Boltzmann equation. If one adds the two equations together, they revert to the standard equation in terms of n alone. The decoherence effect comes from the fact that the free Hamiltonians $\mathcal{H}_{s,l}$ are slightly different for the two components. For non-relativistic particles we have

$$\mathcal{H}_{s,l} \cong m_\chi \begin{pmatrix} 1 & 0 \\ 0 & 1 \end{pmatrix} + \delta m \begin{pmatrix} 0 & 1 \\ 1 & 0 \end{pmatrix} + \frac{\langle k^2 \rangle_{s,l}}{2m_\chi} \left[1 - \frac{\delta m}{m_\chi} \begin{pmatrix} 0 & 1 \\ 1 & 0 \end{pmatrix} \right]. \tag{B.7}$$

The important feature is the difference between $\langle k^2 \rangle_l$ and $\langle k^2 \rangle_s$, so for simplicity one could take, for example,

$$\langle k^2 \rangle_s = \tfrac{1}{2}\langle k^2 \rangle \text{ and } \langle k^2 \rangle_l = \tfrac{3}{2}\langle k^2 \rangle, \tag{B.8}$$

which is a temperature-dependent split. For temperatures such that scattering is still in equilibrium, we can estimate

$$\langle k^2 \rangle \sim 3m_\chi^2/x, \tag{B.9}$$

where $x = m_\chi/T$. After scatterings freeze out, the wavenumber red-shifts as $1/a$, so $\langle k^2 \rangle \sim 3m_\chi^2\, x_f/x^2$.

This effect can be important only in the early universe when the momenta are sufficiently large that k^2/m_χ^2 is not negligible. We have applied this formalism to check the early-universe solutions shown in Fig.17 and we have found no appreciable effect from this extra source of decoherence.

APPENDIX C – Upper limits for the DM Majorana mass

The content of this chapter is heavily based on Ref. [46], where our main results are published.

In this appendix, we will investigate the upper bound on the Majorana mass δm. This parameter determines the timescale on which annihilations recouple after the initial asymmetric dark matter freezeout epoch. For convenience, we define $\alpha = Y_{11} - Y_{22}, \beta = Y_{12} - Y_{21}, \theta = Y_{12} + Y_{21}$, $\gamma = Y_{11} + Y_{22}$, $s = \bar{s} m_\chi^3/x^3$, $H = \kappa m_\chi^2/x^2$, where $\bar{s} = \frac{2\pi^2}{45} g_{*s}$, $\kappa = \frac{1.67}{M_p}\sqrt{g_*}$.

C.1 Flavor-blind interactions

From the Boltzmann equations after freeze-out we get

$$x^2\beta' - \left(\frac{\bar{s}\,\langle\sigma v\rangle_a\, m_\chi}{\kappa}\eta_{DM}\right)\beta - \left(\frac{2i\delta m}{\kappa\, m_\chi^2}\eta_{DM}\right)x^3 = 0, \tag{C.1}$$

with $\beta(\bar{x}) = 0$ as initial condition. Here we used $\alpha \approx Y_{11} \approx \eta_{DM}$ (this does not imply $\alpha' = 0$), as we are working before the moment of residual annihilations. The solution to this equation can be approximated to $\beta(x) \approx iBx(A+x)/2$, where

$$A \equiv \frac{\bar{s}\,\langle\sigma v\rangle_a\, m_\chi}{\kappa}\eta_{DM}, \qquad B \equiv \frac{2\,\delta m}{\kappa\, m_\chi^2}\eta_{DM}. \tag{C.2}$$

Plugging this result into the Boltzmann equations for Y_{11} and Y_{22}, we get

$$\begin{aligned} 16\,\eta_{DM}\,Y_{11}' &= B^2(A+x)\,(A(A+x)-4)\,, \\ 16\,\eta_{DM}\,Y_{22}' &= B^2(A+x)\,(A(A+x)+4)\,, \end{aligned} \tag{C.3}$$

with initial conditions $Y_{11}(\bar{x}) = \eta_{DM}$ and $Y_{22}(\bar{x}) = 0$.

Taking the solutions for Y_{11} and Y_{22} and solving for x when $Y_{11}(\bar{\bar{x}}) = Y_{22}(\bar{\bar{x}})$ gives

$$\bar{\bar{x}} = 1.53\frac{m_\chi}{\sqrt{\delta m\, M_p}}g_*^{1/4}. \tag{C.4}$$

Now that we have found $\gamma = Y_{11} + Y_{22}$ near the epoch of residual annihilations, let us calculate how much it can deviate from η_{DM}. Defining the fractional change in the dark matter comoving density from $\gamma = \eta_{DM}\,(1 - \delta_\eta)$, we get

$$\delta m \lesssim \frac{342}{\sqrt{g_*}} \frac{\delta_\eta^{1/2}}{\langle\sigma v\rangle_a^2\, \eta_{DM}^2 M_p^3}, \tag{C.5}$$

for $x > \bar{\bar{x}}$. As a numerical example, for our set of parameters and taking $\delta_\eta \simeq 3\%$ (as limited by the change in the dark matter density after the formation of the CMB [62]), we get $\delta m \lesssim 3 \times 10^{-30}$ eV. This bound will be relaxed if the second epoch of annihilation freezes out before the formation of the CMB [101].

C.2 Flavor-sensitive interactions

In this case, the equation for β reads

$$x^{5/2}\beta' + \left(\frac{3 I_s g'^4 m_\chi^3 \bar{s}\, \eta_{DM}}{8\pi\kappa m_V^4}\right)\beta - \left(\frac{2i\delta m\, \eta_{DM}}{\kappa m_\chi^2}\right) x^{7/2} = 0 \tag{C.6}$$

where we considered $\alpha \approx \eta_{DM}$ and

$$\langle\sigma v\rangle_s = \frac{I_s g'^4 m_\chi^2}{4\pi m_V^4}\frac{1}{\sqrt{x}} = \overline{\langle\sigma v\rangle}_s \frac{1}{\sqrt{x}}. \tag{C.7}$$

This time, A is redefined to

$$A \equiv \frac{3 I_s g'^4 m_\chi^3 \bar{s}\, \eta_{DM}}{8\pi\kappa m_V^4}. \tag{C.8}$$

Working with our set of parameters, it is possible to approximate the solution of Eq. (C.6) to

$$\beta(x) \approx i\left(\frac{2}{3}\right)^{7/3} A^{4/3} B\, \Gamma\!\left(-\frac{4}{3}, \frac{2A}{3x^{3/2}}\right), \tag{C.9}$$

where the incomplete gamma function is defined by $\Gamma(a,z) = \int_z^\infty t^{a-1}e^{-t}dt$. Now we can use this result and solve for α. Taking the limit $\Gamma(s,r)/r^s = -1/s$ when $r \to 0$ for $Re(s) < 0$, we get

$$\alpha(x) = \eta_{DM}\left(1 - \frac{\delta m^2}{2\kappa^2 m_\chi^4} x^4\right). \tag{C.10}$$

Solving $\alpha = 0$ for x gives us the previous result of Eq. (C.4).

Now, let us rearrange the Boltzmann equations as an equation for the total DM comoving density γ

$$xH\gamma' = -\frac{1}{2}\langle\sigma v\rangle_a\, s\left(\gamma^2 - \Upsilon^2\right) \tag{C.11}$$

and an equation for its "late-time equilibrium" function $\Upsilon = \frac{\sqrt{f(x)}}{2\delta m}$,

$$f' = -3\overline{\langle\sigma v\rangle}_s \frac{s}{\sqrt{x}} \eta_{DM} x H (\alpha')^2, \tag{C.12}$$

where

$$f = (xH\alpha')^2 + 4\delta m^2 \alpha^2. \tag{C.13}$$

We will not attempt to solve the full set of equations from before freeze-out to today. Instead, let's try to evolve our functions from their states in the flat land to new states in the region of residual annihilations.

As we are working with smaller and smaller values of δm, let us explore what happens when $\delta m \to 0$. In this limit, there should be no residual annihilations, i.e. the total DM density must follow a constant equilibrium function, $\lim_{\delta m\to 0} \Upsilon = \eta_{DM}$. Consequently,

$$\lim_{\delta m\to 0} f(x) = 4\delta m^2 \eta_{DM}^2. \tag{C.14}$$

From this result, and equations (C.12) and (C.13) we get, $\alpha' \to 0$ and $\alpha \to \eta_{DM}$, in this limit. Also, $\beta \to 0$. Thus, $\Upsilon^2 \to \alpha^2$. Now, Eq. (C.10) was obtained using $\alpha \approx \eta_{DM}$. Performing the inverse substitution we get

$$\alpha(z) = \frac{\eta_{DM}}{\left(1 + \frac{z^2}{2}\right)}, \tag{C.15}$$

where we defined $z \equiv \frac{\delta m}{\kappa m_\chi^2} x^2$. From now on, we will use z instead of x. For example, from Eq. (C.10), the moment when $Y_{11} = Y_{22}$, i.e. $\alpha = 0$, is given by $z = \sqrt{2}$. Now, the equation we need to solve is,

$$z^{3/2} \delta_\eta'(z) = W\, \eta_{DM} \left[1 - 2\delta_\eta(z) - \frac{1}{\left(1 + \frac{z^2}{2}\right)^2}\right], \tag{C.16}$$

where we have parametrized the total DM density as $\gamma = \eta_{DM}(1 - \delta_\eta)$, where $\delta_\eta \ll 1$ and we have used $(1 - \delta_\eta)^2 \approx 1 - 2\delta_\eta$. Also, we defined

$$W \equiv \frac{\langle\sigma v\rangle_a\, \bar{s}}{4\kappa^{3/2}} \sqrt{\delta m} = \overline{W}\sqrt{\delta m}. \tag{C.17}$$

To a good approximation, we obtain

$$\delta_\eta(z) \approx \frac{\overline{W}\, \eta_{DM}}{2} \sqrt{\delta m} \frac{z^{3/2}}{2 + z^2}. \tag{C.18}$$

In this way,

$$\delta m \approx \frac{1521}{\sqrt{g_*}} \frac{\delta_\eta^2}{\langle\sigma v\rangle_a^2\, \eta_{DM}^2 M_p^3} \frac{(2 + z^2)^2}{z^3}. \tag{C.19}$$

Before getting an upper bound for δm, let us go back to Eq. (C.12) and Eq. (C.13). These can be merged into

$$x^{5/2}\alpha'' + \left(2A - x^{3/2}\right)\alpha' + \left(\frac{B}{\eta_{DM}}\right)^2 x^{9/2}\alpha = 0. \tag{C.20}$$

We notice there is a dramatic change in this equation when the damping term changes sign. For this reason, we take $2A - x^{3/2} = 0$ and solve for x,

$$\bar{\bar{x}} = \left[\frac{3}{1.66\sqrt{g_*}}\overline{\langle\sigma v\rangle}_s \bar{s}\, m_\chi M_p\, \eta_{DM}\right]^{2/3} \tag{C.21}$$

which gives us a a better approximation for the starting point $\bar{\bar{x}}$ for residual annihilations. Numerically, this gives us $\bar{\bar{z}} \ll 1$, so we can make the following approximation

$$\frac{(2+\bar{\bar{z}}^2)^2}{\bar{\bar{z}}^3} \to \frac{4}{\bar{\bar{z}}^3}. \tag{C.22}$$

Since this is our starting point, for any $z > \bar{\bar{z}}$ we have from Eq. (C.19)

$$\delta m < 16.3 \frac{m_\chi^{1/2}}{g_*^{1/4}} \frac{\delta_\eta^{1/2}}{\overline{\langle\sigma v\rangle}_s \langle\sigma v\rangle_a^{1/2}\, \eta_{DM}^{3/2} M_p^{5/2}}. \tag{C.23}$$

As we can see, for a fixed δm, the change in the DM comoving density δ_η goes to zero when we turn off scatterings. For our parameters, we obtain $\delta m < 5 \times 10^{-28}$ eV.

C.3 An approximate expression for the mass of I_3

The content of this chapter is heavily based on our recent preprint [69], where our main results are published.

In order to calculate the mass of the dark matter candidate in this model, we make the following definitions

$$\zeta \equiv \frac{v_{\rm D}}{v_{\rm M}}, \quad \eta \equiv \frac{v_{\rm D}}{v_H}, \quad \chi \equiv \frac{v_H}{v_{\rm M}}, \tag{C.24}$$

where $v_{\rm D} \ll v_H \approx v_{SM} \approx 246$ GeV $\ll v_{\rm M}$. From Eq.(4.2) the mass matrix for CP-odd scalars M_I^2 is

$$M_I^2 = \frac{v_{SM}^2}{2\chi^3}\,(1-\eta^2)^2\, m_I^2, \tag{C.25}$$

where m_I^2/χ is given by

$$\begin{pmatrix}
(1+\sqrt{2})\frac{\zeta^2}{\chi} & \sqrt{2}\,\zeta & \zeta & 0 & 0 & 0 & (-2+\sqrt{2})\,\zeta^2 \\
\sqrt{2}\,\zeta & \sqrt{2}\chi-\beta_{13} & \beta_{13} & \beta_{13}\zeta & 0 & -\beta_{13}\zeta & \sqrt{2}\zeta\chi \\
\zeta & \beta_{13} & \chi-\beta_{13} & -\beta_{13}\zeta & 0 & \beta_{13}\zeta & -\sqrt{2}\zeta\chi \\
0 & \beta_{13}\zeta & -\beta_{13}\zeta & -\beta_{13}\zeta^2 & 0 & \beta_{13}\zeta^2 & 0 \\
0 & 0 & 0 & 0 & \frac{2\kappa\chi^2}{(1-\eta^2)^2} & 0 & 0 \\
0 & -\beta_{13}\zeta & \beta_{13}\zeta & \beta_{13}\zeta^2 & 0 & -9\beta_{3X}-\beta_{13}\zeta^2 & 3\beta_{3X} \\
(-2+\sqrt{2})\,\zeta^2 & \sqrt{2}\zeta\chi & -2\zeta\chi & 0 & 0 & 3\beta_{3X} & (4+\sqrt{2})\zeta^2\chi-\beta_{3X}
\end{pmatrix} \tag{C.26}$$

Since the role of η is small in this matrix, we can safely take $\eta \to 0$ independently of ζ and χ. From the $(5,5)$ element of this matrix, we can note one eigenvalue is equal to $2\kappa\chi^2$ and $\det(M_I^2)$=0, so at least another one is also zero. Solving for the eigenvalues λ, we get the following eigenvectors in the { Im(H), Im(Φ_1), Im(Φ_2), Im(ϕ_1), Im(ϕ_2), Im(ϕ_3), Im(ϕ_X) } basis:

$$\begin{aligned}
\{6\chi,-9\zeta,0,-8,0,1,3\} \text{ and } \{-\chi,\zeta,\zeta,0,0,0,0\} \quad &\text{for} \quad \lambda=0 \\
\{0,0,0,0,1,0,0\} \quad &\text{for} \quad \lambda=2\kappa\chi^2
\end{aligned} \tag{C.27}$$

up to normalization factors. In Ref. [91] all masses were found (in the limit $\zeta \to 0$) in the CP-odd scalar sector except for m_{I_3}, which was given a numerical estimate of $\sim \mathcal{O}(\zeta^{1/2})$ in GeV. Here we find an approximate value for this mass, which is the mass of the decaying DM candidate we are studying in this work m_{I_3}.

The equation for the eigenvalues of m_I^2 reads

$$\lambda^2(\lambda-2\kappa\chi^2)p(\lambda)=0, \tag{C.28}$$

where $p(\lambda)=\sum_{i=0}^{4} c_i\,\lambda^i$ with c_4=1. Expanding and comparing coefficients with $\det(\lambda\,\mathrm{I}_{7\times7}-m_I^2)$, we get (to lowest order in the new parameters from Eq.(C.24)),

$$\begin{aligned}
c_0 &\approx 74\sqrt{2}\beta_{13}\beta_{3X}\zeta^2\chi^6, \\
c_1 &\approx 10\sqrt{2}\chi^5\beta_{3X}+11\sqrt{2}\zeta^2\chi^5\beta_{13}-10(1+\sqrt{2})\chi^4\beta_{13}\beta_{3X}, \\
c_2 &\approx \sqrt{2}\chi^4-10(1+\sqrt{2})\chi^3\beta_{3X}-(1+\sqrt{2})\chi^3\beta_{13}+20\chi^2\beta_{13}\beta_{3X}, \\
c_3 &\approx -(1+\sqrt{2})\chi^2+10\chi\beta_{3X}+2\chi\beta_{13}.
\end{aligned}$$

Because m_{I_3} is expected to be small, we can expand $p(\lambda)$ around zero $p(\lambda) \approx p(0) + p'(0)\,\lambda$ and solve $p(\lambda) = 0$ for λ, i.e.

$$\lambda \approx -\frac{p(0)}{p'(0)} = -\frac{c_0}{c_1} = \frac{74\sqrt{2}\beta_{13}\beta_{3X}\zeta^2\chi^2}{10\beta_{3X}((1+\sqrt{2})\beta_{13} - \sqrt{2}\chi) - 11\sqrt{2}\beta_{13}\zeta^2\chi}, \tag{C.29}$$

which gives us

$$m_{I_3}^3 \simeq \frac{v_{SM}^2}{2\chi^3}\lambda = \frac{37\, v_{SM}\, v_{\rm M}^2 v_{\rm D}^2\, \beta_{13}\, \beta_{3X}}{5\sqrt{2}(1+\sqrt{2})v_{\rm M}^3\beta_{13}\beta_{3X} - v_{SM}\,(11 v_{\rm D}^2\beta_{13} + 10 v_{\rm M}^2\beta_{3X})}. \tag{C.30}$$

C.4 Rayleigh-Schrodinger perturbation theory

The content of this chapter is heavily based on our recent preprint [69], where our main results are published.

In this appendix, we find approximate expressions for I_3 and its mass using Rayleigh-Schrodinger perturbation theory [92–94].

First of all, let's write $\tilde{m}_I^2 \equiv m_I^2/\chi$ as

$$\tilde{m}_I^2 = \tilde{m}_0^2 + \zeta\tilde{m}_1^2 + \zeta^2\tilde{m}_2^2, \tag{C.31}$$

where

$$\tilde{m}_0^2 = \begin{pmatrix} 0 & 0 & 0 & 0 & 0 & 0 & 0 \\ 0 & \sqrt{2}\chi - \beta_{13} & \beta_{13} & 0 & 0 & 0 & 0 \\ 0 & \beta_{13} & \chi - \beta_{13} & 0 & 0 & 0 & 0 \\ 0 & 0 & 0 & 0 & 0 & 0 & 0 \\ 0 & 0 & 0 & 2\kappa\chi^2 & 0 & 0 & 0 \\ 0 & 0 & 0 & 0 & 0 & -9\beta_{3X} & 3\beta_{3X} \\ 0 & 0 & 0 & 0 & 0 & 3\beta_{3X} & -\beta_{3X} \end{pmatrix} \tag{C.32}$$

$$\tilde{m}_1^2 = \begin{pmatrix} 0 & \sqrt{2} & 1 & 0 & 0 & 0 & 0 \\ \sqrt{2} & 0 & 0 & \beta_{13} & 0 & -\beta_{13} & \sqrt{2}\,\chi \\ 1 & 0 & 0 & -\beta_{13} & 0 & \beta_{13} & -2\,\chi \\ 0 & \beta_{13} & -\beta_{13} & 0 & 0 & 0 & 0 \\ 0 & 0 & 0 & 0 & 0 & 0 & 0 \\ 0 & -\beta_{13} & \beta_{13} & 0 & 0 & 0 & 0 \\ 0 & \sqrt{2}\,\chi & -2\,\chi & 0 & 0 & 0 & 0 \end{pmatrix} \tag{C.33}$$

$$\tilde{m}_2^2 = \begin{pmatrix} \frac{1+\sqrt{2}}{\chi} & 0 & 0 & 0 & 0 & 0 & -2+\sqrt{2} \\ 0 & 0 & 0 & 0 & 0 & 0 & 0 \\ 0 & 0 & 0 & 0 & 0 & 0 & 0 \\ 0 & 0 & 0 & -\beta_{13} & 0 & \beta_{13} & 0 \\ 0 & 0 & 0 & 0 & 0 & 0 & 0 \\ 0 & 0 & 0 & \beta_{13} & 0 & -\beta_{13} & 0 \\ -2+\sqrt{2} & 0 & 0 & 0 & 0 & 0 & (4+\sqrt{2})\chi \end{pmatrix} \tag{C.34}$$

The first *unperturbed* eigenvalues and eigenvectors come from $\tilde{m}_0^2$ and they are (before normalization)

$$\begin{aligned} \lambda_1^{(0)} &= 0,\ \lambda_2^{(0)} = 0,\ \lambda_3^{(0)} = 0,\ \lambda_4^{(0)} = -10\,\beta_{3X},\ \lambda_5^{(0)} = 2\kappa\chi^2, \\ \lambda_{6,7}^{(0)} &= \left[-2\beta_{13} + (1+\sqrt{2})\chi \mp \sqrt{4\beta_{13}^2 + (3-2\sqrt{2})\chi^2}\right]/2, \end{aligned} \tag{C.35}$$

$$\begin{aligned} I_1^{(0)} &= (1,0,0,0,0,0,0),\ I_2^{(0)} = (0,0,0,1,0,0,0),\ I_3^{(0)} = (0,0,0,0,0,1,3), \\ I_4^{(0)} &= (0,0,0,0,0,-3,1),\ I_5^{(0)} = (0,0,0,0,1,0,0),\ I_6^{(0)} = (0,r^-,1,0,0,0,0), \\ I_7^{(0)} &= (0,r^+,1,0,0,0,0), \end{aligned} \tag{C.36}$$

where $2\beta_{13}\, r^{\pm} = (\sqrt{2}-1)\chi \pm \sqrt{4\beta_{13}^2 + (3-2\sqrt{2})\chi^2}$. The first order corrections are

$$\lambda_i^{(1)} = \left\langle I_i^{(0)} | \tilde{m}_1^2 | I_i^{(0)} \right\rangle \ \text{ and } \ I_i^{(1)} = -\left(\tilde{m}_0^2 - \lambda_i^{(0)} \mathrm{I}_{7\times 7}\right)^{\mathrm{PS}} \left(\tilde{m}_1^2 - \lambda_i^{(1)} \mathrm{I}_{7\times 7}\right) I_i^{(0)}, \tag{C.37}$$

where $\mathrm{I}_{7\times 7}$ is the identity matrix and PS stands for the pseudoinverse of a matrix. For $i = 3$ we have $\lambda_3^{(0)} = 0$, so

$$I_3^{(1)} = -\tilde{m}_0^{\mathrm{PS}} \tilde{m}_1^2 I_3^{(0)} = (0, 3t - 8\beta_{13}, -6t + 8\sqrt{2}\beta_{13}, 0, 0, 0, 0), \tag{C.38}$$

where $\sqrt{2}\, t = (2+\sqrt{2})\beta_{13} - 2\chi$. Next, the second order correction reads

$$\lambda_3^{(2)} = \left\langle I_3^{(0)} | \tilde{m}_0^2 | I_3^{(0)} \right\rangle + \left\langle I_3^{(0)} | \tilde{m}_1^2 | I_3^{(1)} \right\rangle$$

$$\lambda_3^{(2)} = \frac{1}{10}\left(9(4+\sqrt{2})\chi - \beta_{13}\right) + \frac{1}{3\sqrt{10}N_3}\left[(6t - 8\sqrt{2}\beta_{13})(6\chi - \beta_{13}) + (3t - 8\beta_{13})(3\sqrt{2}\chi - \beta_{13})\right], \tag{C.39}$$

with the normalization factor $N_3 = [90\chi^2 + 6(2-7\sqrt{2})\beta_{13}\chi + (87-54\sqrt{2})\beta_{13}^2]^{1/2}$.

Now, we can compute the second order contribution to the eigenvector of I_3

$$I_3^{(2)} = -(\tilde{m}_0^2)^{\mathrm{PS}} \left[(\tilde{m}_2^2 - \lambda_3^{(2)}) I_3^{(0)} + \tilde{m}_1^2 I_3^{(1)} \right] = (0,0,0,0,0,-3,1)/\sqrt{10}. \tag{C.40}$$

Finally, I_3 and its mass can be approximated to

$$I_3 \simeq I_3^{(0)} + \zeta\, I_3^{(1)} + \zeta^2\, I_3^{(2)} \quad \text{and} \quad m_{I_3}^2 \simeq \frac{v_{SM}^2}{2\chi^2} \zeta^2 \lambda_3^{(2)} \approx \frac{1}{2} v_{\mathrm{D}}^2 \lambda_3^{(2)}. \tag{C.41}$$